博士論文

Satellite-based nearshore monitoring of suspended fine sediments discharged from multiple rivers
（沿岸域における複数河川から供給される浮遊細砂の**衛星モ**ニタリング）

ヘッティアーラッチゲ カビンダ グナセーカラ

(HETTIARACHCHIGE KAVINDA GUNASEKARA)

SATELLITE-BASED NEARSHORE MONITORING OF SUSPENDED FINE SEDIMENTS DISCHARGED FROM MULTIPLE RIVERS

沿岸域における複数河川から供給される浮遊細砂の衛星モニタリング

HETTIARACHCHIGE KAVINDA GUNASEKARA

A dissertation submitted to the Department of Civil Engineering,

in partial fulfillment of the requirements for the Degree of

Doctor of Philosophy

Department of Civil Engineering

The University of Tokyo

September 2016

Members of the Examination Committee

Yoshimitsu Tajima   **Professor**
Department of Civil Engineering   Supervisor
The University of Tokyo

Shinji Sato   **Professor**
Department of Civil Engineering
The University of Tokyo

Jun Sasaki   **Professor**
Department of Socio-Cultural
Environmental Studies
The University of Tokyo

Takenori Shimozono   **Associate Professor**
Department of Civil Engineering
The University of Tokyo

Wataru Takeuchi   **Associate Professor**
Institute of Industrial Science
The University of Tokyo

DECLARATION

I hereby certify that I am the sole author of this thesis, and that neither any part of this thesis nor a whole of the thesis has been submitted elsewhere for the award of any degree or diploma of other University or Institution.

I declare that this is a true copy of my thesis work, including any last revisions, as approved by my thesis examination committee.

_____

HETTIARACHCHIGE KAVINDA GUNASEKARA

ABSTRACT

Under the significant load of human activity, such as the construction of dams and sand mining from riverbeds, coastal erosion has become a worldwide problem. While the change of shoreline locations can be directly observed by local residents or from some other measures such as aerial photographs, it is difficult to monitor the quantitative features of sediment discharge from rivers and the nearshore movement of discharged sediment, which are primary causes of coastal erosion. A lack of such quantitative data makes it difficult to implement effective and appropriate measures for mitigation from and protection against coastal erosion problems.

Satellite-based monitoring techniques can be powerful tools for understanding the nearshore behavior of sediments discharged from rivers and there are a number of existing studies which aim to use satellite data for monitoring the turbidity patterns in nearshore areas. Most of these studies, however, focus on the monitoring of a specific region for a relatively short period of time and, thus, developed monitoring techniques may not provide us with sufficient data to understand the characteristics of the daily sediment movement which causes coastal erosion.

This study aims to develop a new satellite-based monitoring system, which enables us to capture the daily sediment behavior with relatively high temporal resolutions. Since the turbidity patterns are expected to change dynamically with the tides, river flows, waves and some other factors, the monitoring frequency and the amount/duration of available data are some of the primary features for selection of the appropriate satellite for the present monitoring system. After a review and comparisons of several candidates for satellite data, this study selected the MODIS satellite which records the data of each site twice a day and archives the data over the past sixteen years. All the archived data from 2000 to December 2015 were utilized for the analysis. Data processing, such as downloading, reprojection, mosaicking and resampling, is automated in the Linux environment.

One of the unique and challenging features of this study is that we aim to use all the available MODIS data over the past sixteen years to understand the spatial and temporal behavior of the turbidity patterns. Some of the MODIS data, however, are fully/partially affected by cloud and the present monitoring system needs to exclude the influence of the cloud in the analysis of the turbidity patterns. While the red band

has high reflectance from both cloud and high turbidity, the NIR band shows low reflectance from the turbid water but high reflectance from the cloud. Thus, this study utilizes these characteristics and newly determines the threshold value for detection of the cloud by the ratio of the difference between the red band and NIR band and the red band reflectance itself.

The present cloud masking algorithm is specially calibrated for cloud on the sea water and was improved in that the new system has less chance of misdetection of cloud on the sea surface. Many of the obtained turbidity maps partially contain pixels with cloud. On the other hand, the observed horizontal length scale of the turbidity variation appears to be much larger than the pixels' size, 250m. Based on this fact, this study introduces a unique cell system to represent the spatial-temporal turbidity patterns. The developed cell system in the study area contains more than 16 pixels per cell and the average turbidity can be obtained even if the cell is partially covered by cloud. Alongshore boundaries of the cell were determined parallel to the shoreline so that selected cells are aligned at about the same distance from the shoreline. Several Matlab scripts were developed to automatically process daily images to estimate the turbidity in each pixel and to obtain the average turbidity over each cell, in which the pixels covered by cloud were excluded. Besides such cell-based analysis, which increases the amount of available data at each location, the original pixel-based turbidity data are also used for estimation of the areas of higher turbidity around the river mouths. The developed monitoring system was then applied to the Red and Ma River systems in the northern part of Vietnam and to the Enshu-nada coast, Japan. In Vietnam, the Red River system shows a decreasing trend in the turbidity of suspended fine sediment discharge while the Ma River tends to have an increasing trend. Observed yearly variations of the turbidity at the mouth of the Ma River were then compared with the observed river discharge data and they showed a very clear correlation with each other. This feature validates the use of the present monitoring system for observation of turbidity patterns discharged from the river mouths.

Along the Enshu-nada coast, the cell-based daily turbidity product is able to capture the direction and alongshore extent of the suspended load discharged from the Tenryu River, and it shows a relationship with the shape of the sandpit near the

river mouth. Furthermore, the flood events of the Tenryu River were also closely correlated with the estimated area of high turbid plume around the mouth of the Tenryu River.

ACKNOWLEDGEMENT

I wish to express my deepest appreciation and gratitude to my supervisor, Professor Yoshimitsu Tajima, who helped and guided me to make this research a success. Without his guidance and persistent help this dissertation would not have been possible.

My committee members, Professor Shinji Sato, Professor Jun Sasaki, Associate Professor Takenori Shimozono and Associate Professor Wataru Takeuchi, who spent their valuable time in advising me all through the research work is gratefully acknowledged.

I would like to acknowledge the support of the Japanese government for providing me the Japanese government (Monbukagakusho) scholarship during the study periods.

I must also thank my wife who encouraged me at all the time and, for all her love, friendship and tolerance throughout my research work.

Finally I wish to thank all who helped me to carry out this project successfully even though the names have not been mentioned.

To SARA,

My amazing wife,

Whose sacrificial care me and our son, OKITH

made it possible for me to complete this work

Table of Content

List of Figures

List of Tables

List of Abbreviations

C. blue	Coastal Blue
CZCS	Coastal Zone Color Scanner
FTU	Nephelometric Turbidity Unit
L7	Landsat 7
L8	Landsat 8
MERIS	Medium Resolution Spectral Imager
MIR	Short wavelength infrared
MODIS	Moderate Resolution Imaging Spectroradiometer
NIR	Near-infrared
RRD	Red River Delta
SeaWiFS	Sea-viewing Wide Field-of-view Sensor
SPM	Suspended Particulate Matter
SS	Suspended Sediment
SSC	Suspended Sediment Concentration

CHAPTER ONE

INTRODUCTION

1.1 Background

Monitoring the amount of sedimentary discharge from rivers and the budgets for the littoral drift of sediments are key issues for sustainable coastal beach protection. Satellite-based monitoring of the spatial and temporal variation of turbid river plumes may be one of the effective methods that enable us to understand the long-term trend of sedimentary discharge from rivers and the resulting budget of alongshore sediment transport.

Moreover, the environment and ecosystems of coastal estuaries, especially mangroves, sea grass and coral reefs are often very sensitive and vulnerable. Recently, the turbidity influence of coastal waters clearly has increased around nearshore areas. That causes water contamination and damage to tourism activities and the degradation of coral reefs which reduces the primary productivity of phytoplankton by limiting photosynthetic activity and the characteristic ecosystems including mangroves, sea grass and coral reefs, etc.

In Vietnam, the Red River system, which releases large amounts of sediment into the Gulf of Tonkin, consists of eight river mouths. Milliman and Meade ranked the Red River Delta (RRD) as the ninth largest river system in terms of sedimentary discharge in 1983. The construction of dams and rerouting of river channels have had a major impact on the diverse sedimentary discharge patterns in the north of Vietnam.

Figure 1.1 shows the high concentration of suspended sedimentary discharge entering into the nearshore environment in Hai Phong Bay, in the north of Vietnam. Figure 1.2 illustrates the corresponding Landsat satellite image in the same area. This kind of suspended sedimentary plume can be measured and monitored in terms of water quality, and it could be very relevant to the level of water turbidity. There are many ways to monitor water quality such as deploying sensors on the site, selective water sampling for laboratory tests, ground-based sensors, etc. The use of a satellite-based monitoring scheme may add some advantages over these ground-based measurements while it may also have disadvantages. The advantages of satellite-

based monitoring are, for example: (i) the monitoring can cover a vast area at each observation time; (ii) the capability of remote and periodic monitoring; (iii) the archives of relatively long-term and periodic observations; and (iv) the cost effectiveness for monitoring the wider area. The main disadvantage is the calibration of satellite data for the better representation of realistic conditions. The reliable correlation of satellite remote sensing and water quality can be used to monitor and quantify the present and past sedimentary discharge patterns of rivers.

Figure 1.1 Photos of highly turbid discharge in the Northern part of Vietnam

Figure 1.2 Landsat satellite image of highly turbid discharge in the Northern part of Vietnam

1.2   Scope and Methodology of the Present Study

Many studies have been carried out to map the suspended sediments through the use of remote sensing techniques. Petus et al. 2010 and Doxaran et al. 2002 applied satellite-based surface reflectance data for mapping the turbidity of the water surface due to suspended sediments. Doxaran et al. 2009 and Park & Latrubesse 2014 specifically presented the capability of the moderate resolution imaging spectroradiometer (MODIS) satellite products for the mapping of turbidity and suspended matters.

While the estimated turbidity values of the water surface may not directly represent the contribution of suspended sediment for the coastal sediment budget, the continuous monitoring of the spatial distribution of turbidity patterns at a higher level of temporal scale provides us with various kinds of information, such as the timings of high discharge, the alongshore behavior of discharged suspended sediments, and comparisons of the relative magnitudes of suspended sediments discharged from multiple rivers along the extensive length of coastal areas. Several studies focus on the estimation of suspended sediment concentrations as a function of the observed turbidity to understand the mechanism (Lewis & Eads 2001).

Since the nearshore turbidity dynamically changes in different temporal and spatial scales, in order to have a better understanding of the behavior of turbidity, monitoring of spatial and temporal variations at higher temporal scales is required. Petus et al. 2014, Park & Latrubesse 2015 and Park & Latrubesse 2014 presented spatiotemporal monitoring of the turbidity/suspended sediment concentration using MODIS data products. The MODIS satellite has an imaging archive collection over the last 16 years and it is capable of obtaining two images per day at any location on Earth. Since the MODIS is an optical satellite, cloud coverage is the main constraint in using the whole of the 16 years' archive data (for which the observations are still ongoing). The above-cited studies mainly selected cloud-free dates manually or chose a shorter period of data set for the analysis.

There are several limitations to the realization of long-term and frequent monitoring of turbidity over wider coastal stretches, including multiple rivers, based on satellite data such as MODIS. The primary limitations are: (i) automated cloud-masking techniques and (ii) effective use of data which are partially covered by

cloud. Thus, this study aims to develop a satellite-based long-term and frequent monitoring system of suspended fine sediments patterns along the coast and to investigate the applicability and feasibility of the developed system for the monitoring and understanding of the characteristic behavior of suspended sediments discharged from multiple rivers.

The main objectives of the study have been set up as follows:
1. To develop a reliable method for the estimation of turbidity based on MODIS along the coast around the Red River Delta, Vietnam.
2. To develop a method to mask out automatically the cloud in the MODIS data.
3. To develop a method to monitor the spatial and temporal behavior of turbidity patterns along the coast based on MODIS.
4. To investigate several methods of analysis for the better understanding of the characteristics of the alongshore behavior of fine suspended sediments discharged from multiple rivers.
5. To investigate the applicability and feasibility of the above-mentioned developed monitoring techniques in other areas.

In order to achieve the above objectives, two study sites have been selected to investigate the sediment discharge patterns of multiple river mouths; in the northern part of Vietnam and the Enshu-nada coast in Japan. Several field extrusions have been carried out to establish the relationship between the discharged suspended river sediments and the surface reflectance data of the MODIS satellite. Special attention has been made to use as much as possible of the MODIS data for the analysis without excluding any due to the presence of scattered cloud patches. As mentioned above, most of the previous studies have used only much clearer MODIS data sets for analysis.

The overall methodology is illustrated in Figure 1.3. After extracting most of the possible daily basis turbidity patterns, a relative comparison of the river turbidity discharge patterns has been made to understand the characteristics of the rivers over time. Furthermore, an attempt has been made to try to understand the relationship between the river waters' discharged characteristics and the spatial extent of turbidity

patterns in nearshore areas. After understanding the response of the turbidity patterns to the river waters' characteristics, the response has been used to understand the locations where limited data sets and information are available.
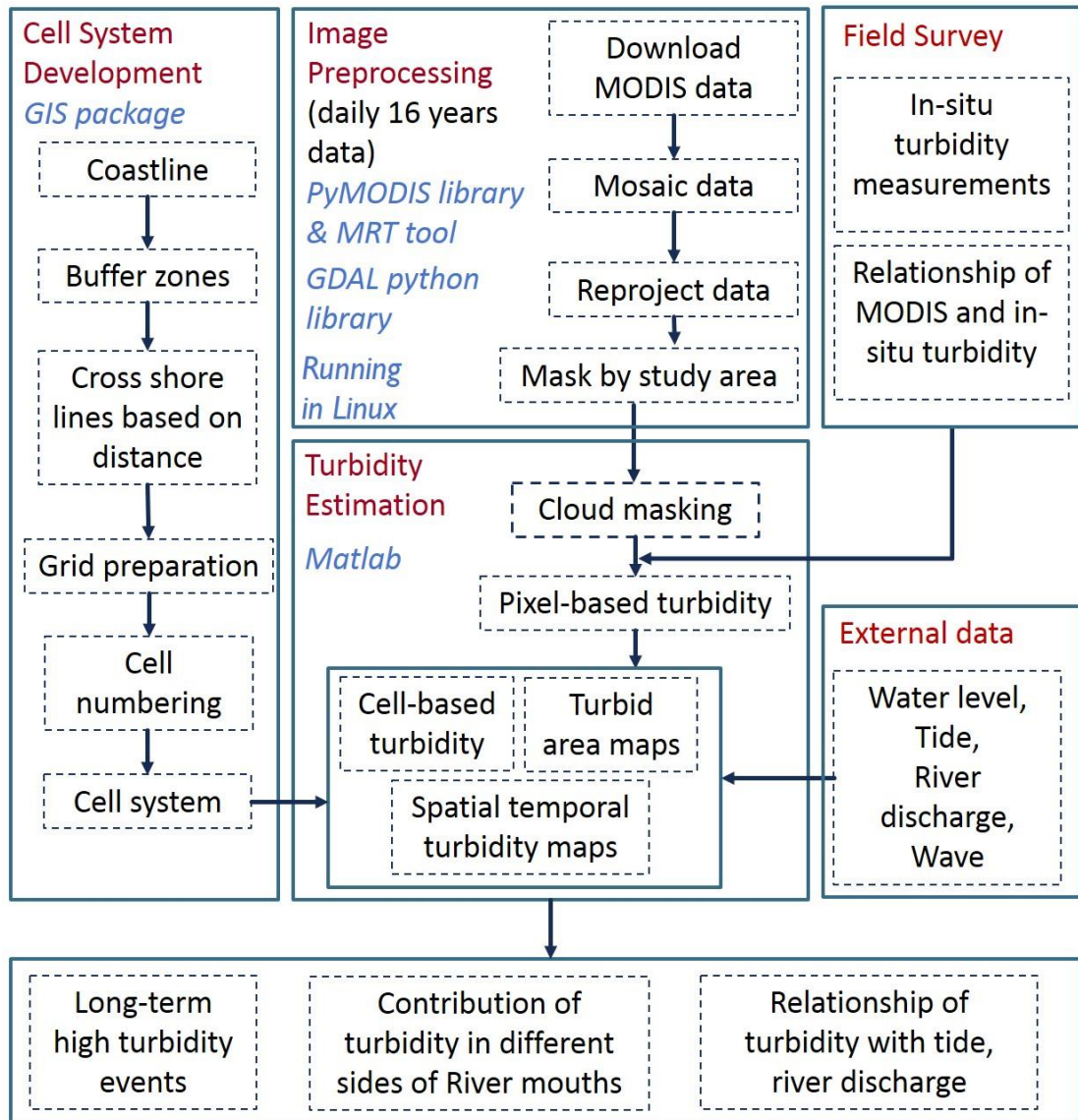
Figure 1.3 Overall methodology of the study

1.3 Thesis Structure

This thesis consists of the following eight chapters.

CHAPTER 1: INTRODUCTION

The reader can refer to this chapter to get an idea of the thesis and the chapter further describes the scope of the research, objectives and the overall methodology.

CHAPTER 2: REMOTE SENSING OF OCEAN COLOR IN COASTAL AREAS

This chapter serves as a literature review of the research topic. It also focuses on the technical details about satellite data

CHAPTER 3: STUDY SITES AND FIELD SURVEY

Two study sites have been selected to implement the monitoring system. Therefore, the main target of this chapter is to discuss the characteristics of the study sites. Moreover, all the fieldworks and laboratory experiments are also discussed here.

CHAPTER 4: DEVELOPMENT OF SATELLITE-BASED MONITORING SYSTEM

This chapter presents the development of a satellite-based monitoring system in detail. The newly introduced cloud masking algorithm is also discussed, and comparison has been made to highlight the uniqueness of the introduced algorithm.

CHAPTER 5: SPATIAL-TEMPORAL SUSPENDED FINE SEDIMENT PATTERNS

This chapter describes the results of the satellite-based monitoring system. The suspended fine sediments patterns are quantified based on the area, direction and level of the sediment concentration, and are then related to the alongshore contribution in the long-term and seasonal time frames. Moreover, all the suspended

fine sediments patterns are further analyzed with the river discharges, tides, waves and wind data.

CHAPTER 6: FEASIBILITY AND APPLICABILITY OF THE PROPOSED MONITORING SYSTEM IN THE OTHER AREA (THE ENSHU-NADA COAST)

This chapter evaluates the feasibility and applicability of developing monitoring in the other study area. The Enshu-nada coast has been selected and the spatial-temporal variation of suspended fine sediments is described.

CHAPTER 7: SATELLITE-BASED ANALYSIS OF AN EXTREME WEATHER EVENT IN A COASTAL AREA

This chapter is devoted to the typhoon Haiyan, an extreme weather event which heavily damaged the eastern coast of the Philippines. The damage was analyzed based on the alongshore distribution of the sand encroachment lines, vegetation changes, and wave-sheltering effects.

CHAPTER 8: CONCLUSIONS AND RECOMMENDATIONS

This chapter concludes the study by emphasizing its uniqueness and importance. Then, an attempt has been made to report the components that can be studied further to improve and expand the use of the findings of the research.

CHAPTER TWO

REMOTE SENSING OF OCEAN COLOR IN COASTAL AREA

2.1   Introduction

The physics of ocean color remote sensing is discussed in the first part of this chapter. The second part of this chapter is dedicated to a review of previous studies and existing algorithms on suspended sediments/turbidity. The selection of satellite data for the study and a detailed description about MODIS data will be discussed in the last part of this chapter.

2.2   Passive Remote Sensing of Ocean Color in Coastal

In passive remote sensing, the sun is the energy source to obtain a radiometric flux reaching towards a sensor after traveling though the atmosphere and scattering. Therefore, the sensor can obtain data in the daytime. It records several sections of the electromagnetic spectrum in the visible and near-infrared portions. The receiving sensor could be mounted on a satellite, airplane or any other platform but in this study only satellite-based observations are considered. Most of the satellites are sun-synchronized so that satellite sensors pass through the same area at nearly same time. MODIS, MERIS (Medium Resolution Imaging Spectrometer), SeaWiFS (Sea-viewing Wide Field-of-view Sensor), and CZCS (Coastal Zone Color Scanner) are some of the satellite sensors widely use in ocean color remote sensing studies.

The passive sensor receives mainly three types of energy with respect to the traveling medium and path of the energy:

   i.   Light reaching the sensor after scattering in the atmosphere;

   ii.   Light reaching the sensor after specular reflection on the object surface;

   iii.   Upwelling light from the water surface after back-scattering.

All the above could be subject to attenuation due to the absorption and scattering by the atmosphere. Figure 1.1 and 1.2 of the ICCG (2000) report illustrates the schematic diagram of passive remote sensing and possible pathways to the sensor. In ocean color studies, only upwelling lights from the sea surface contain useful

information. Most of the energy received by the satellite sensor undergoes multiple scattering due to atmospheric obstacles such as atmospheric gases and aerosols. Atmospheric correction is a necessary step in ocean color analysis. Global atmospheric correction algorithms exist and need localized corrections for accurate quantification of the results.

2.3   Mapping of Suspended Sediments/Turbidity

Mapping and monitoring of a large area with a higher temporal resolution is only possible with a remote sensing approach. Satellite remote sensing has an added advantage compared with areal imaging because satellite-based mapping and monitoring of suspended sediments and turbidity have been in existence since the 1970s.

After launching Landsat data, the file is widely expanded by various approaches. After that several satellite sensors are introduced to dedicatedly map the suspended sediment concentration and turbidity. Some of the sensors were introduced in the previous section.

River discharge suspended sediment is highly varied and has localized characteristics. Therefore, most of the site-specific case studies have to be carried out to obtain a better estimation of the suspended sediment or turbidity. Recently, there have been a few attempts to produce a globally reliable relationship to obtain turbidity (Dogliotti et al., 2015) but that kind of approach is still under the validation process.

The in-situ measurements of the turbidity and suspended sediment concentration are necessary to obtain a site-specific relationship. Doxaran et al., (2009) introduced a few assumptions for direct comparison between in situ measured and satellite derived suspended sediment concentrations, the assumptions being as follows:

(1)   The turbidity of surface waters is homogeneous over the satellite pixel beside the in situ measurements and does not change significantly in time between the closest in situ and satellite measurements (the maximum time difference of 5 min);

(2) The water turbidity is homogeneous within the first meter below the surface (as the turbidity sensor on the measurement platform is at a fixed depth of 1

m, while the optical depth viewed and analyzed by the satellite can be lower than 1 m).

Farooq (2011) studied the response of the visible portion of the electromagnetic spectrum against the different concentrations of suspended sediments. The red portion of the electromagnetic spectrum shows a higher sensitivity to the different levels of suspended sediment concentration. The sensitivity decreases towards the blue and near-infrared regions where the wavelengths decrease and increase, respectively. Therefore, the multispectral satellite data sets that include the red band are very useful for mapping the suspended sediment variations.

The following section discusses the existing algorithms and studies on suspended sediment mapping using remote sensing data and the use of the red band for the mapping is emphasized.

2.4   Existing Algorithms and Studies

There are many existing studies on mapping the suspended sediment concentration and turbidity. Out of those studies, the more relevant studies which are closely oriented with the scope of this study been selected and are presented here. The type of satellite, portion of the electromagnetic spectrum, cloud masking technique or procedure of selection of the qualified pixels, time span of the analysis and interpretation of coastal behavior based on the results are considered to choose the studies to present in this section.

Doxaran et al., (2009) conducted a study in an estuary using the MODIS band 1 (red) and band 2 to obtain the concentration of suspended particulate matter (SPM). The research introduced a site-specific relationship to quantify the SPM using both bands and an analysis was conducted over a specific period of time. The images for the analysis were selected based on visual inspection to avoid images with haze and cloud. The research deployed the MOD09GQ (Terra) and MYD09GQ (Aqua) atmospherically corrected level 2 dataset. The same authors conducted a study in 2002 (Doxaran et al., 2002) and presented the relationship between the SPM and both the red and NIR bands using the Landsat satellite.

A study on suspended sediment in the Amazon River was carried out by Park and Latrubesse, (2014). The MODIS 250m resolution product, the MOD09GQ and MYD09GQ data set, was used after atmospheric correction. In this study, only band 1 was used for the estimation of the suspended sediment concentration and the study highlighted the usefulness of the red band for the estimation of the suspended sediment concentration. Three sets of a site-specific relationship were introduced and the suspended sediment concentration and red band reflectance showed a good correlation. In-depth analysis was made to remove the pixels with a large solar zenith angle. Another MODIS product, MOD13Q1, was used to obtain the water mask and use that also as a parameter to select the qualified pixels for the analysis. The analysis was made from 2000 to 2010 at three study sites, and found that the number of usable images in the 10 years period was between 200 to 300.

Petus et al., (2010) conducted a study to estimate the turbidity and total suspended matter of a river plume using a MODIS 250m resolution dataset which was similar to the above studies. The cloud free images were selected by means of another thematic map that was obtained from another source. The relationship introduced by Doxaran et al., (2009) was used to obtain the suspended matter concentration with the MODIS data set. The in-situ measurements of turbidity and total suspended matter concentration were further used to obtain turbidity maps. Petus et al., (2014) again demonstrated a similar technique to map suspended matter and turbidity in another site, and further extended analysis to relate MODIS based results with river discharge.

2.5   Selection of Satellite Data for the Study

Table 2.1 shows the details of the candidate satellites for this study and the most popular satellites (freely obtainable) are considered for the comparison. The Landsat and Sentinel-1 satellites are the best for the spatial resolution but both have a low revisit period which much deviates from the scope of this study. The Himawari-8 data have some potential due to the satellite being geostationary and having a 10min temporal resolution. But the most sensitive band, the red band, for the suspended sediment has a 500m spatial resolution. This dataset is available from July 2015 and cannot be used for historical analysis.

Table 2.1 Potential satellites for this study

Facts	MODIS		Landsat	Sentinel-2			Himawari-8	
Spatial resolution (m)	250	500	30	10	20	60	500	1000
Usable bands for turbidity mapping	2	4	4	2	4	2	1	4
Revisit time	2 images per day		16 days	10days	5 days (after 2016)		10 min (Geo-stationary)	
Accessibility	Free		Free	Free			Free	
Future continuation	Yes		Yes	Yes			Yes	

The MODIS medium-resolution bands (250m and 500m bands) were originally designed as ''sharpening'' bands for land studies and cloud detection, and therefore have lower sensitivities than the MODIS ocean bands. However, through comparison with other sensors including Landsat-7 ETM+, CZCS and SeaWiFS, Hu et al., (2004) concluded that these bands provide sufficient sensitivity for water applications and are at least as useful for coastal ocean applications as CZCS.

After considering all these factors, the MODIS data were selected for this study. Moreover, the Landsat and Sentinel-2 data are obviously useful to verify the derived suspended sediment characteristics from the MODIS data.

2.6 Electromagnetic Spectrum and Satellite Data for Suspended Sediment Mapping

The spectral characteristics of suspended sediments with different concentrations will be discussed here. Moreover, those sensitive regions of the electromagnetic spectrum for suspended sediments and their presence in the satellite's data also will be discussed here.

Farooq (2011) further studied response of different levels of suspended sediment concentration with respect to the wavelength of the electromagnetic spectrum. In that study, it clearly showed that red band more sensitive to the level of the suspended

sediment concentration. The sensitivity decreases towards the blue and near-infrared regions. Therefore, if the multispectral satellite data set includes the red band, that data set is quite useful for the mapping of suspended sediments and turbidity in detail as it is able to categorize according to the degree of the suspended sediment and turbidity. Loisel at al., (2013) explained the clear difference between clear water and highly turbid water. In the NIR region, both relatively clear and turbid water show relatively very low response while in the red band region, high turbid water shows higher response and relatively clear water shows less response. Therefore, both bands are being used in this study.

Table 2.2 shows the multispectral bands and regions of MODIS and Landsat satellites. Both satellites contain red and NIR bands in their multispectral data set. As explained before, to map the spatiotemporal variation of river discharge at higher temporal scale, the MODIS data is being used. There are many MODIS data sets available free of charge to download. The next section of this chapter introduces about MODIS data and the products.

Table 2.2 Multispectral bands and regions of the MODIS and Landsat satellites

	MODIS		Landsat		
	Band	Wave length (nm)	Band		Wave length (nm)
			L8	L 5/7	
C. blue		435-451	B1		435-451
Blue	B3	459-479	B2	B1	452-512
Green	B4	545-565	B3	B2	533-590
Red	B1	620-670	B4	B3	636-673
NIR	B2	841-879	B5	B4	851-879
MIR	B5	1230-1250			
MIR	B6	1628-1652	B6	B5	1566-1651
MIR	B7	2105-2155	B7	B6	2017-2294

2.7   MODIS Data

2.7.1   General description

The MODIS sensor is on board both the Terra and Aqua satellites. It has a wider swath width of 2,330 km and completely captures the entire surface of the Earth every one to two days. It detects 36 spectral bands between 0.405 and 14.385 μm. The 36 bands fall into three spatial resolutions, 250m, 500m and 1000m.

2.7.2 Data products and processing levels

There are many data products derived from MODIS observations describe features of the land, oceans and the atmosphere that can be used for the studies on local to global scales. In this study, 250m spatial resolution MODIS band 1 and 2 of daily surface reflectance were selected.

MOD09 (MODIS Surface Reflectance) is a seven-band product computed from the MODIS Level 1B land bands 1 (620-670 nm), 2 (841-876 nm), 3 (459-479), 4 (545-565 nm), 5 (1230-1250 nm), 6 (1628-1652 nm), and 7 (2105-2155 nm). The product is an estimate of the surface spectral reflectance for each band as it would have been measured at ground level as if there were no atmospheric scattering or absorption. It corrects for the effects of atmospheric gases and aerosols. MOD09GQ data is produced from MOD09 data set which provides only MODIS band 1 and 2 daily surface reflectance in a 250 m resolution gridded product in the Sinusoidal projection. Science Data Sets provided for this product include reflectance for Bands 1 and 2, a quality rating, observation coverage, and observation number (MODIS Surface Reflectance User's Guide).

The gridded data is provided in the global level with different tiles, each tile processes with horizontal and vertical number. Figure 2.1 shows MODIS tiles in the Vietnam study area.

15
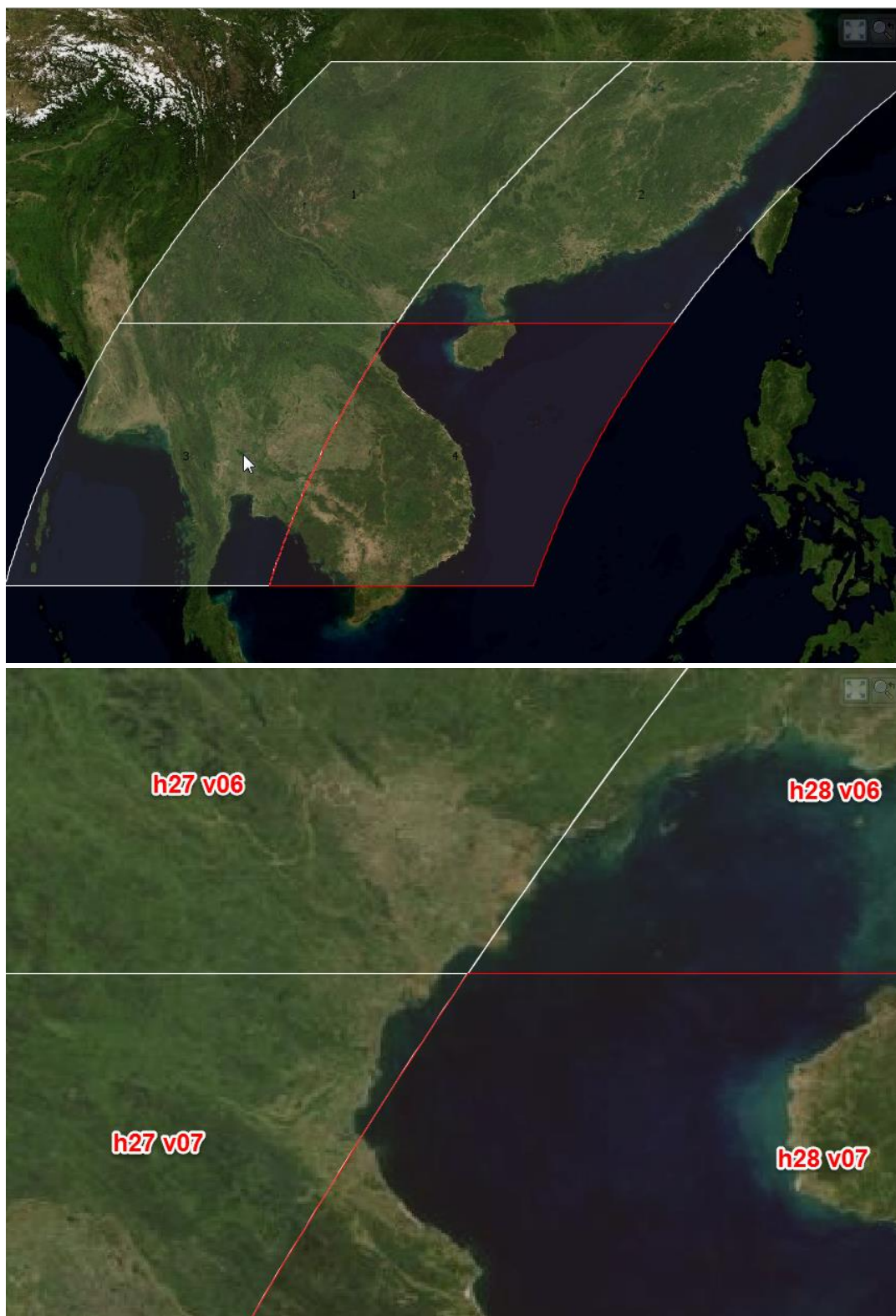
Figure 2.1 Examples of MOD09GQ gridded tiles in the Vietnam study site

CHAPTER THREE

STUDY SITE AND FIELD SURVEY

3.1   Introduction

Field surveys were carried out along the north-eastern coast of Vietnam to obtain the in-situ turbidity and corresponding suspended sediment concentrations at the time of the MODIS image acquisition. Another objective of the field work was to understand the overall characteristics and behavior of suspended sediments discharged from multiple rivers compared with the features of turbidity patterns observed through the developing satellite-based monitoring system.

The first part of this chapter, section 3.2, discusses in-depth the background of the turbidity problem in Vietnam, the hydro-climatic conditions, and details about dam construction and its influences on turbidity patterns to the present time. Section 3.6 then discusses the field survey activities and the outputs.

3.2   Geometric Characteristics of the Coast around the Red River Delta

The Red River discharges a significant amount of sediments, and the Red River Delta is known to have the fourth largest delta plain in Southeast Asia (Hori et al., 2004). Hai Phong, for example, is located in the northern part of Vietnam and is highly affected by complex sediment discharges from multiple branches of the Red River system. The significant sediment discharge around Hai Phong Bay and the Cam Estuary has a notable economic impact not only from the deposition (Lefebvre et al., 2012) in Hai Phong Harbour, one of the main economic hubs in the northern part of Vietnam, but also from high turbidity along the surrounding coastal resorts.

Although some local residents claim that there is an increasing trend in turbidity, especially after the construction of reclaimed land in the bay, there is no quantitative evidence to justify their claims. Besides such reclamation in the bay, construction of dams and reservoirs along the Red River system may also have a significant impact on the sediment discharge and turbidity around the bay. Since the turbidity around the bay dynamically changes in different temporal and spatial scales, a better

understanding of the behavior of turbidity is required for monitoring the spatial and temporal variations of turbidity patterns around the bay.
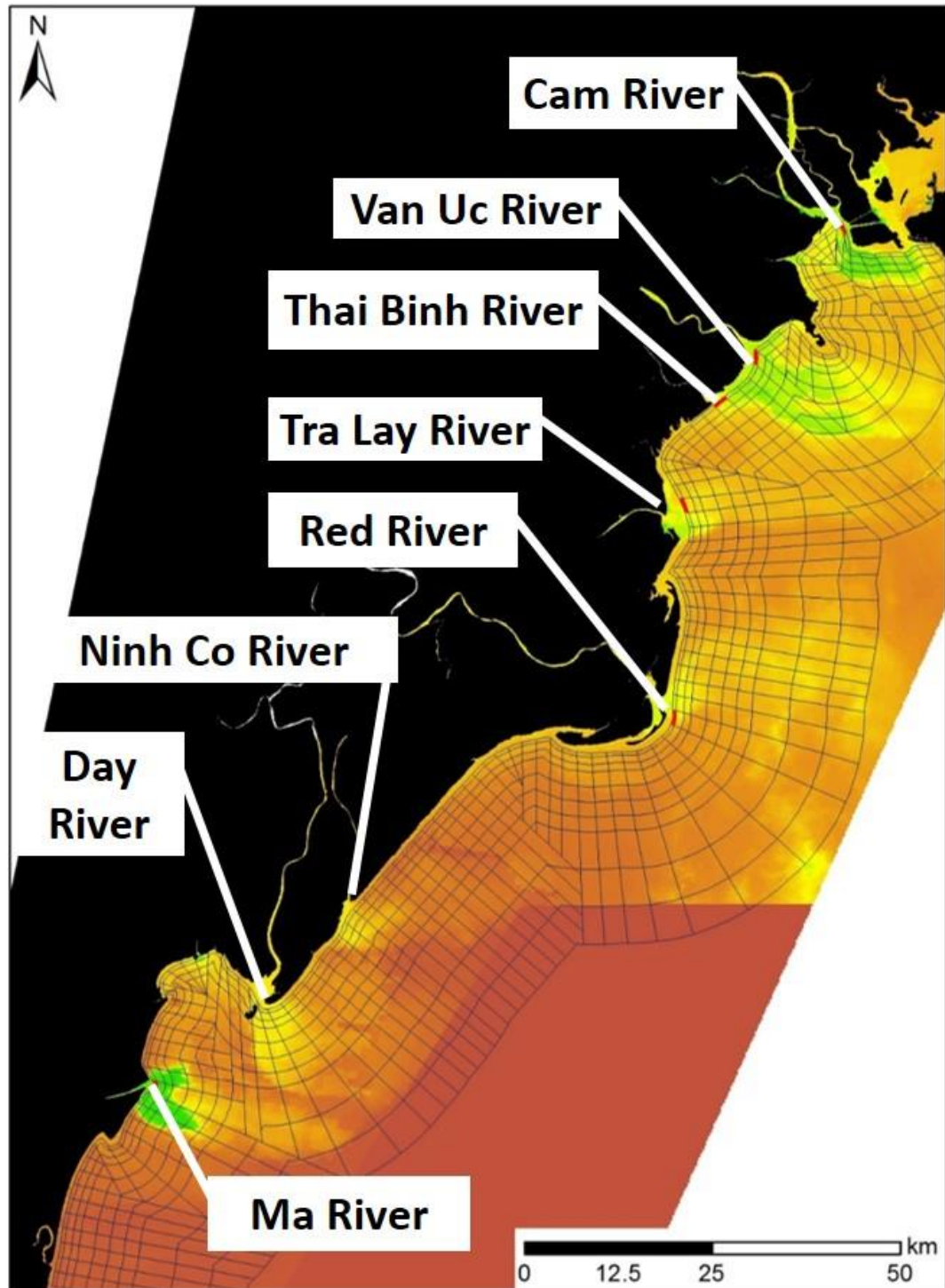
Figure 3.1 A map of Vietnam study area and locations of river mouths
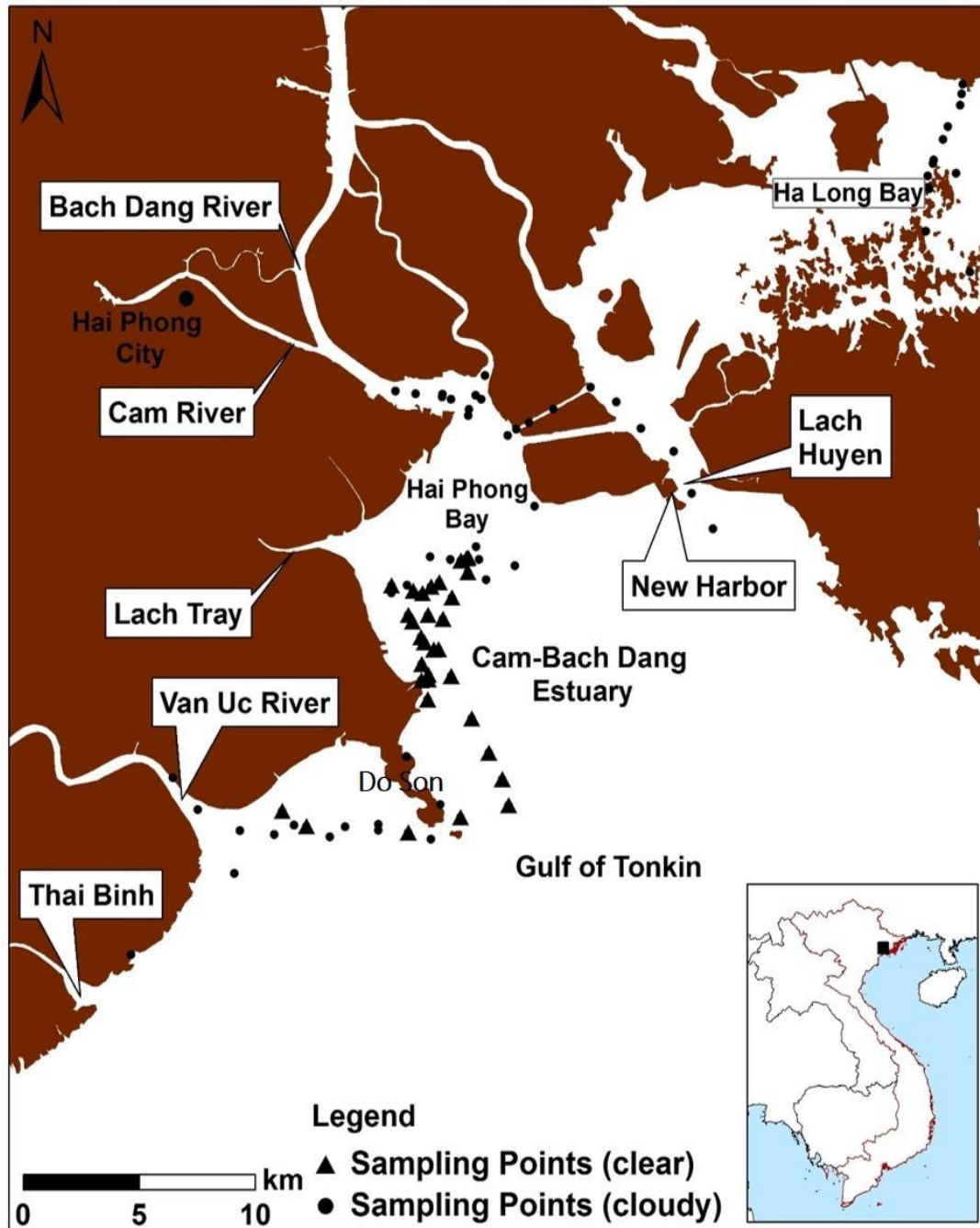
Figure 3.2 A map of sampling site and sampling points when the sky was clear
(triangles) and cloudy (circles)

Figure 3.1 illustrates the Red River system and its main river mouths; the most southerly river is the Day River followed by the Ninh Co River, Red River, Tra Lay River, Thai Binh River, Van Uc River and Cam River towards the north. The Ma River falls in another basin, next to the Red River basin. Figure 3.2 shows a detailed map around Hai Phong Bay where the fieldwork was carried out. The Cam-Bach

Dang Estuary and the sides of the Van Uc River consist of a low water depth of around 1m to 3m. There is a new harbor construction at Lach Huyen.

Ha Long Bay is a world famous world heritage site located on the northeast side of the Cam-Bach Dang Estuary where the seawater is in a very clear condition; this is completely opposite to the condition of Hai Phong Bay. Several satellite images (Figure 1.2 is an example) show some evidence of the redirection of turbid water discharge due to the manmade channels and islands towards Ha Long Bay.

3.3 Hydro-climatic Conditions

3.3.1 Rainfall

Rainfall around the study area depends greatly on cold air masses, storms, and monsoons. Of these three factors, cold air causes more rain, the storms cause heavy rains in the summer and the monsoon rains are persistent. In the coastal areas, there are two seasons: the wet (flood) season from May to October, with the rainfall in this season accounting for nearly 80-90% of the total annual rainfall. The dry season is from November to April in the next year.

3.3.2 River characteristics

(1) River network

This section decribes the characteristcs of the Hai Phong area which has a dense network of rivers (Table 3.1), the average density of which is 0.6 - 0.8 km per km^2, with 16 major rivers spreading throughout the city with a total length of 300 km. All tributaries of the rivers flow into the Gulf of Tonkin with 5 river mouths opening into the sea: these 5 rivers are the Thai Binh, Van Uc, Lach Tray, Cam and Bach Dang.

Table 3.1 The characteristics of some major rivers in Hai Phong

Name of River	Length (km)	Average width (m)	Average depth (m)	Average flow speed (m/s)
Bach Dang	42	1000	8	0.7
Cam	37	400	7	0.7
Van Uc	38	400	8	1.2
Thai Binh	30	150	3	0.4
Lach Tray	43	120	4	0.7

(Source: Hai Phong Council Report, 1990)

(2) River flow

Every year the rivers flow into the sea at Hai Phong with over 30 km^3 of water and 18 million tons of sediment. During the flood season, (June to October), the water load is 75-85% of the year's total, and the sediment load is 90-95% of the total for the whole year. About 14 km^3 of water and 5 million tons of sediment, primarily through the Nam Trieu River, flow out to the northeast of the Do Son peninsula. In particular, the Cam River produces the largest flow in the area with about 10-11 km^3 of water and nearly 4 million tons of sediment; the Lach Tray River produces 1.5 km^3 of water and about 1 million tons of sediment, and the Bach Dang River about 1 km^3 of water per year. Part of the bigger load flows out to the southeast of the Do Son peninsula, mainly through the Van Uc River.

Hai Phong is located in the downstream area of the river system with five big estuaries flowing into the sea: the river mouths of the Thai Binh, Van Uc, Lach Tray, Cua Cam and Nam Trieu. The estuaries are characterized by the same shape, tides, and the annual supply of large amounts of water and silt out of the river mouths.

The average flow rate in the dry season for the estuaries is 10-15 cm/s, and it rarely exceeds 50 cm/s and the tidal current is not dominant. On rainy days, there is a large river flow, often above 100 cm/s, reaching 1.8 to 2.5 m/s, with an dominant tide and flow downstream most of the time during the day. The amount of flow in the river is considerably increased by the tide, with an amount of 40-85% in both seasons. (Table 3.2).

Table 3.2 Correlation of flow rates (million m^3) and tides of some river stations

Hydrology station	Season	Tide flow	Ebb tide flow	River flow
Cau Rao (in Lạch Tray River)	Dry 1992	5.5	9.8	4.3
	Flood 1991	8.2	10.4	2.3
Hung Vuong (in the Cam River)	Dry 1992	19.6	47.6	28.0
	Flood 1991	21.2	51.7	35.9
Cau Da Bach (in the Da Bach River)	Dry 1992	15.8	18.8	3.0
	Flood 1991	16.3	21.5	5.1

(Source: Nguon Tran Duc Thanh, 1993)

The flood season usually starts later than a month of rainy season, and the dry season is from November to April the following year. During the flood season, the water flow accounts for 75-85% of the whole year's total, especially in March, July, August, and September when the discharges account for 50-70% of the year's total.

The biggest floods are usually in July or August, accounting for 20-27%, and sometimes up to 35%, of the annual water flow. During the flood season, the northern rivers (the Da Bach, Cua Cam, and Lach Tray) are influenced by the Thai Binh River flood regime which is stronger, while the southern rivers (the Luoc, Hoa, Thai Binh, and Moi) bear the influence of the Red River flood regime which is stronger. During the flood season, the flood waters from the rivers combined with the low tide line velocity can reach values of 2.0m/s to 2.5m/s; at high tide, the estuary flow is encroached on by pressure or destroyed by the tidal current.

Table 3.3 Flow rates of some of the rivers in Hai Phong

Name of river	Location	Highest rate (m³/s)	Average of dry season flow (m³/s)	Minimum runoff in average (m³/s)	Minimum flow (m³/s)
Kinh Thay	Cua Cam		115	47.2	0.1
Van Uc	Trung Trang	506	193	63.2	52.5
Moi	Mii River	190	82.6	53	48.2
Thai Binh	Cong Go	74.8	16.4	1.1	approximate 0

(Source: Do Dinh Chien Va, 2004)

(3) Sediment flow

The sediment load of the Hai Phong rivers depends heavily on Thai Binh River system and there is an annual discharge into the sea of about 18 million tons, with the upstream supply also largely from the Red River. However, at the shoreline with high tides, the sediment of the rivers of Hai Phong moves up and down in the two-way by tidal regime (Table 3.4).

Table 3.4 Sediment flow rates of some of the rivers in Hai Phong

Name of river	Season	Move volume (tons)	Tidal increase (%)	From river (%)
Cau Da Bach (Da Bach River)	Rainy 1991	3793	48.3	51.7
	Dry 1992	670	83.6	16.4
Hung Vuong (Cam River)	Rainy 1991	8958	24.5	75.5
	Dry 1992	2064	39.2	60.8
Nam Trieu (Ha Luu Bach Dang)	Rainy 1991	12025	27.8	72.2
	Dry 1992	2428	48.3	51.7

(Source: Nguon Tran Duc Thanh, 1993)

Before the Hoa Binh Dam construction in the period 1958 - 1985, the total amount of suspended sediments in a multi-year average was 114 million tons at the Shanxi station but after construction in the period from 1986 to 1997 the total amount dropped to 73 million tons (Pho , 2003).

Due to the impact of the dams in the basin, especially the Hoa Binh Dam, by 1990 the total amount of sediment reaching the northern estuaries was only 85,984.106 tons and after 2010 it was only 35,676.106 tons which is a 58.51% decrease. Before 1990 the two estuaries of the Van Uc River and the Thai Binh River produced a total amount of sediment into the sea of 16,872 million tons/year; after damming this amount was reduced by 9,454 million tons/year to only 7,418 million tons/year, a reduction of 56.03% (Cu et al., 2011).

Before the period of the construction of the Hoa Binh Dam (before 1990), the annual total amount of sediment flowing into the sea from the Van Uc River was 11.696 million tons/year and after 1990 it decreased by 6.546 million tons/year to only 5,150 million tons/year. The total amount of sediment greatly diminished on June, 7, 8, 9, 10 and 11. After construction of the dam, the total amount of sediment flowing through the mouth of the Van Uc River decreased by 57.92% during the flood season and during the dry season fell by 15.00%.

Before 1990 the total annual amount of sediment flowing into the sea at the Thai Binh River estuary was 5,172 million tons/year and after construction of the Hoa Binh Dam this decreased by 2,890 million tons/year to only 2.282 million tons/year. The total amount of sediment greatly diminished on June, 7, 8, 9, 10 and 11. After the Hoa Binh Dam construction, the total movement of sand into the Thai Binh estuary was reduced to 57.81% in the flood season and there was a 12.15% reduction in the dry season.

Unlike the Van Uc River and the south of the Thai Binh River, the mouth of the Do Son River tended to have a decline trend of sediment load. The Bach Dang River, north Cua Cam and Lach Tray, Do Son tend to have increased sediment load after Hoa Binh Dam construction (Vinh, 2012). The Cam River sediment load was 2 million tons/year in the 1960s, but after construction of the Hoa Binh Dam this rose to nearly 4 million tons/year.

According to the monitoring and calculations of Binh et al., (2010), the total sediment discharge of the Bach Dang River and Lach Tray was about 5.8 million tons annually.

Thus, after the construction of the Hoa Binh Dam, the total amount of sediment flowing from the rivers and emptying into the sea through Hai Phong in the north is about 5.8 million tonnes and in the south is about 7.4 million tons, a total of 13.2 million tons, which is down by 4.8 million tons (26.6%) compared with the time before the construction of the Hoa Binh Dam.

3.3.3 Tidal variations

The north of Vietnam is characterized by diurnal tides, with one ebb-flood cycle occurring each day. Figure 3.3 (top) shows the observed tide variations at the Hon Dau tidal station (located near the Do Son peninsula, Hai Phong Bay) in 2014. The black dots represent the tide height at the MODIS observation time. Figure 3.3 (bottom) shows the tidal variations from August 1, 2014 to September 30, 2014 with the MODIS acquisition time. Within a month, the MODIS images nearly cover the low and high tide levels, but the availability of usable data totally depends on the coverage of the cloud.

Figure 3.4 shows the monthly average value of the tides at the MODIS observation time of both the Aqua and Terra satellites. Around March, both satellites observe the area with the same tidal condition (1.5 m) and around September it is around 2.5 m. Moreover, if we want to understand the influence of the tides from MODIS, it is better to try images from December to January and from May to July.
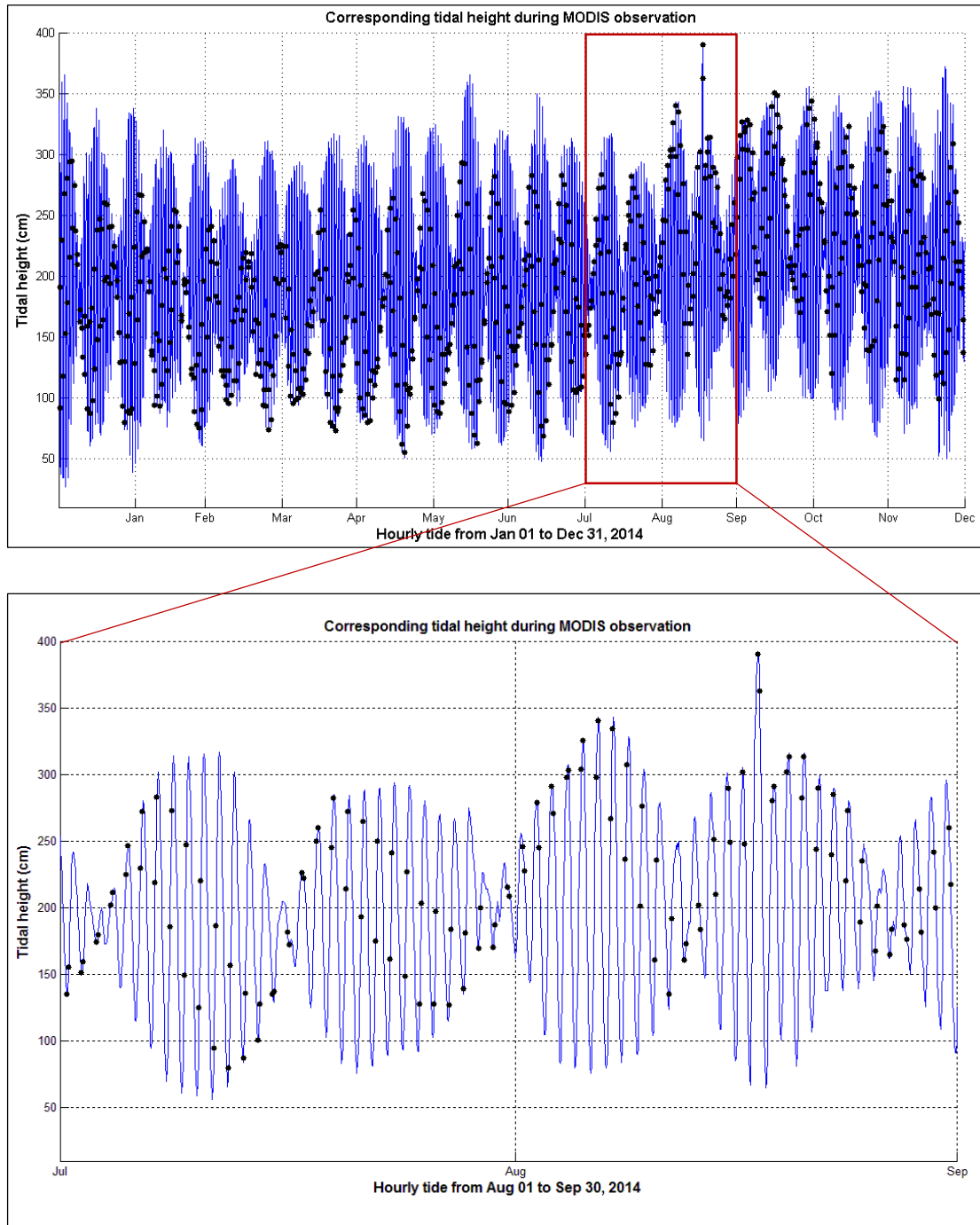
Figure 3.3 Tidal variations plotted with time of the MODIS acquisition
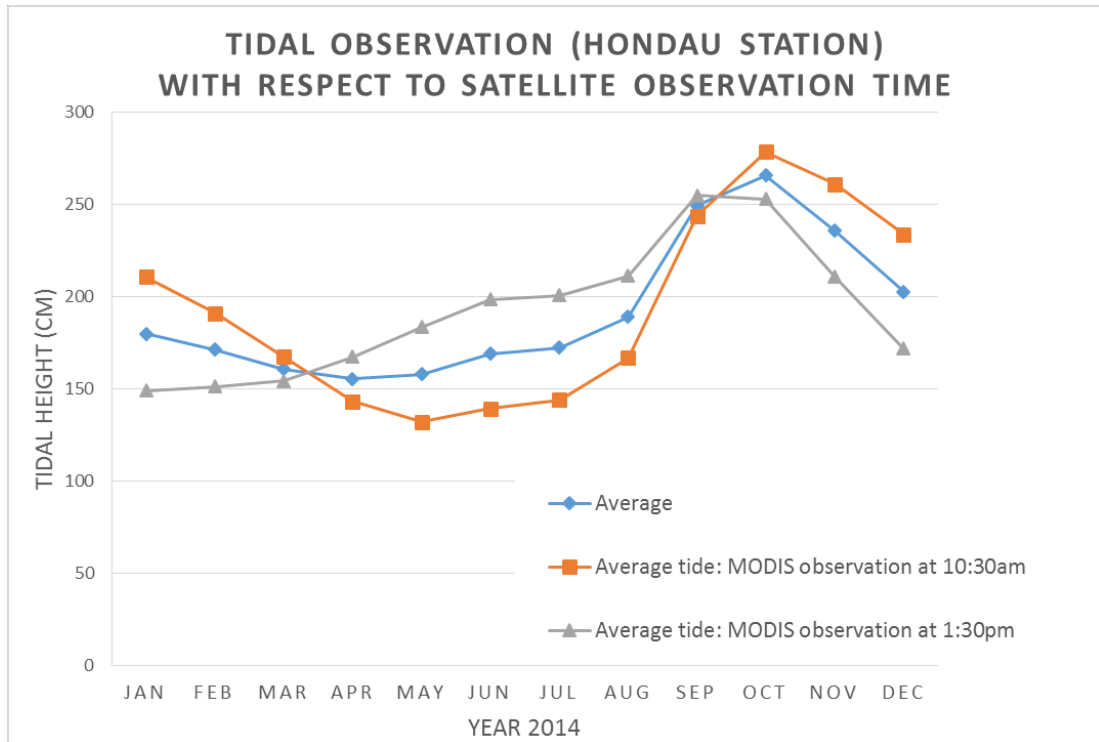
Figure 3.4 Monthly average tidal level variation over a year (2014)

3.3.4 Wind and waves

The Hai Phong costal zone lies within the influence of the tropical monsoon regime and its impact across Southeast Asia. The NE monsoon season is from October to March in the next year and the prevailing wind direction is N to NE. Every month there is an average of 3-4 monsoons, each one lasting 3-5 days. The average wind speed level is 5-6 and the strongest level is 7-8. The NE wind blows parallel to the shore and should be very strong, but it does not have the ability to create large waves. The summer monsoon has a prevailing wind direction of SE to E. The average wind speed is 2.5 to 3.0 m/s. Storms and tropical depressions appear in the summer, and hurricane wind speeds reach 35-50 m/s. The SE wind blows nearly perpendicular to the shore, with great momentum and the ability to create large waves. The number of days with wind speeds greater than 15 m/s is unevenly distributed among months, but are focussed primarily from May to October to coincide with the storms in the region.

The characteristics of the coastal wind regimes in Hai Phong are based on the measured wind data analysis center at Hon Dau National Meteorological sation for

1960 - 2011 (Figure 3.5). The features of the regional winds include seasonal fluctuations as well as the monthly fluctuations. Among them, the predominant wind direction frequency is greater during the flood season when the wind is S to SE. Meanwhile in the dry season, the prevailing wind direction is NE to E.
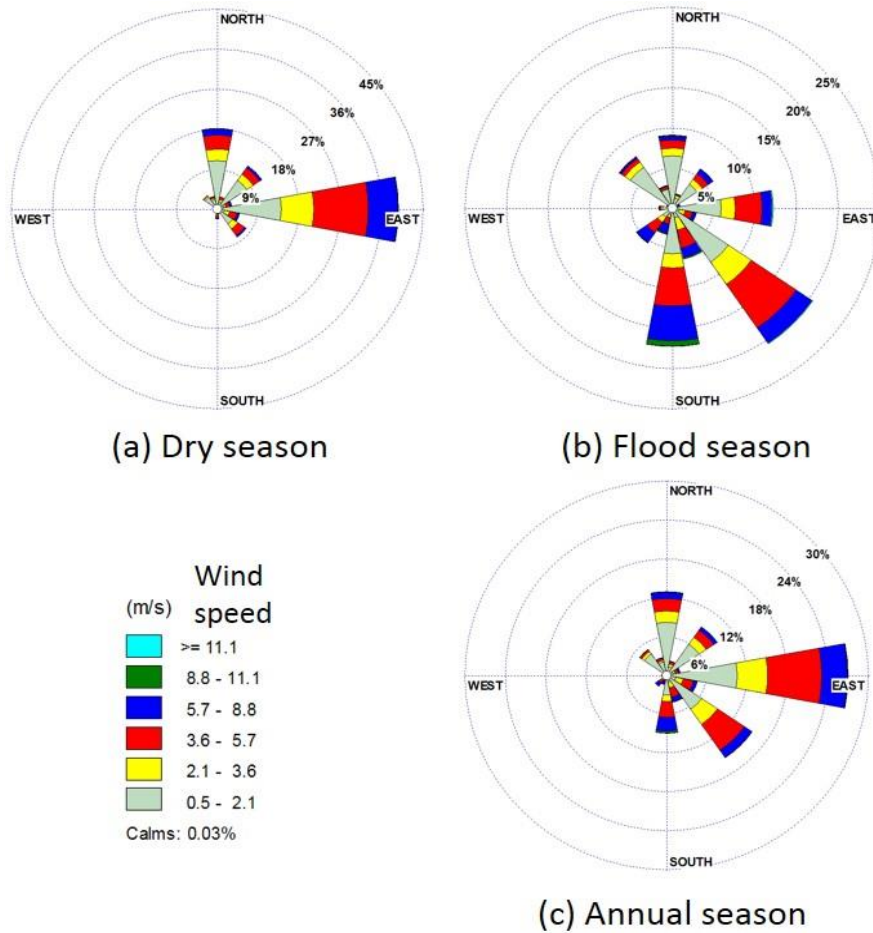
Figure 3.5 Annual average wind directions at Hon Dau National Hydrology Station (1960-2011). a- dry season; b- flood season; c- annual (Source: Tu, 2012)

3.4 Thermoluminescence and Sediment Movement Characteristics around the Ma River
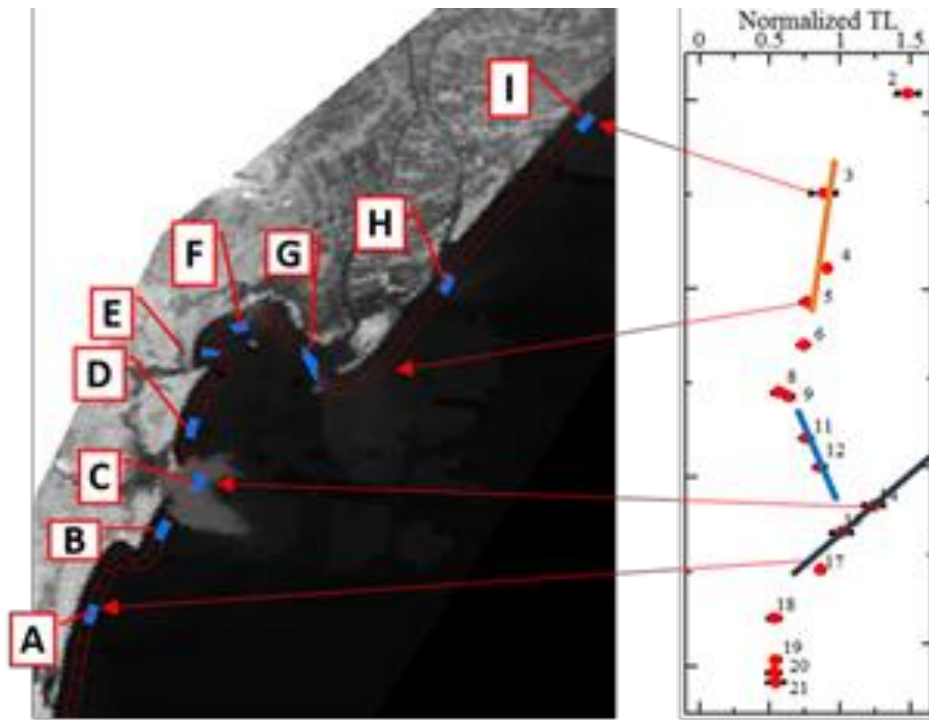
Figure 3.6 A detail map of the Ma River and thermoluminescence variation

Higashi et al., (2015) carried out a study around the Ma River on sediment movement characteristics using thermoluminescence (TL). Figure 3.8 shows the signal intensity of the TL of feldspars in samples obtained along the coastline from the Red River to the Ma River. As seen in the figure, the intensity of the TL gradually decreases with the distance from the river mouth. The alongshore TL intensity is known to represent how much the sand grains have been exposed to the sunlight as they migrate along the coast after being discharged from the river. A quick decay of the TL in the alongshore direction therefore indicates that the sand grains slowly migrated towards the direction to which the TL intensity decreases while the gradual decay of the TL indicates fast migration of the sediments. The high TL intensity at the river mouth indicates that the river discharges a certain amount of sediments which have a lower TL intensity.

As seen in Figure 3.6, a clear peak of the TL intensity around the mouth of the Ma River indicates that the Ma River actively discharges a certain amount of sediments and the Ma River is the main source of the sediment supply over the surrounding

coast on both the north and south sides of the river mouth. A relatively faster decay of the TL in the southward direction rather than the northward direction at the mouth of the Ma River may indicate that littoral movement of sediments is relatively slower in the southward direction rather than the northward direction. Relatively low TL intensity along the coast on the south side of the Red River may indicate that the sediment supply from the Red River to this coast is no longer dominant.

3.5 Field Work

3.5.1 In-situ measurements of turbidity

   Field surveys were conducted around Hai Phong Bay and around the mouth of the Van Uc River to obtain the in situ turbidity data, which is used for validation of the developing satellite-based turbidity monitoring system. These field surveys were carried out at the time when MODIS was recorded around the target area. To cover both the rainy and dry seasons, we carried out two field surveys in the dry season, March 2015 and February 2016 and four field surveys in the rainy season, July 2014, July 2015, September 2015 and November 2015. The extent of the data collection coverage highly depended on weather conditions at the study site although it was not easy to forecast the cloud-free days when MODIS was also recorded. Some of the turbidity data could not be used for comparisons with the MODIS data since these sites were covered by cloud and no reliable reflectance data were obtained from MODIS. Turbidity was measured with the turbidity meter, INFINITY_CLW ACLW2-USB, which can measure the turbidity within the range from 0 to 1,000 FTU (Formazin Nephelometric Unit).

   A tourist boat was used for the data collection, and we stopped the boat at each survey point to avoid the influence of turbulence on the turbidity measurements. At each point, the turbidity meter was dropped into the water with a rope and the depth of the turbidity sensor was maintained at less than 50cm at all the sampling locations. The coordinates of each point were recorded by GPS. At each location, the turbidity was recorded for more than two minutes to obtain the average turbidity value over the time. Figure 3.7 shows photographs during the fieldwork when the turbidity front was clearly observed. The sampling locations were selected so that the measured turbidities are distributed in the wider range. Before the fieldwork, we synchronized
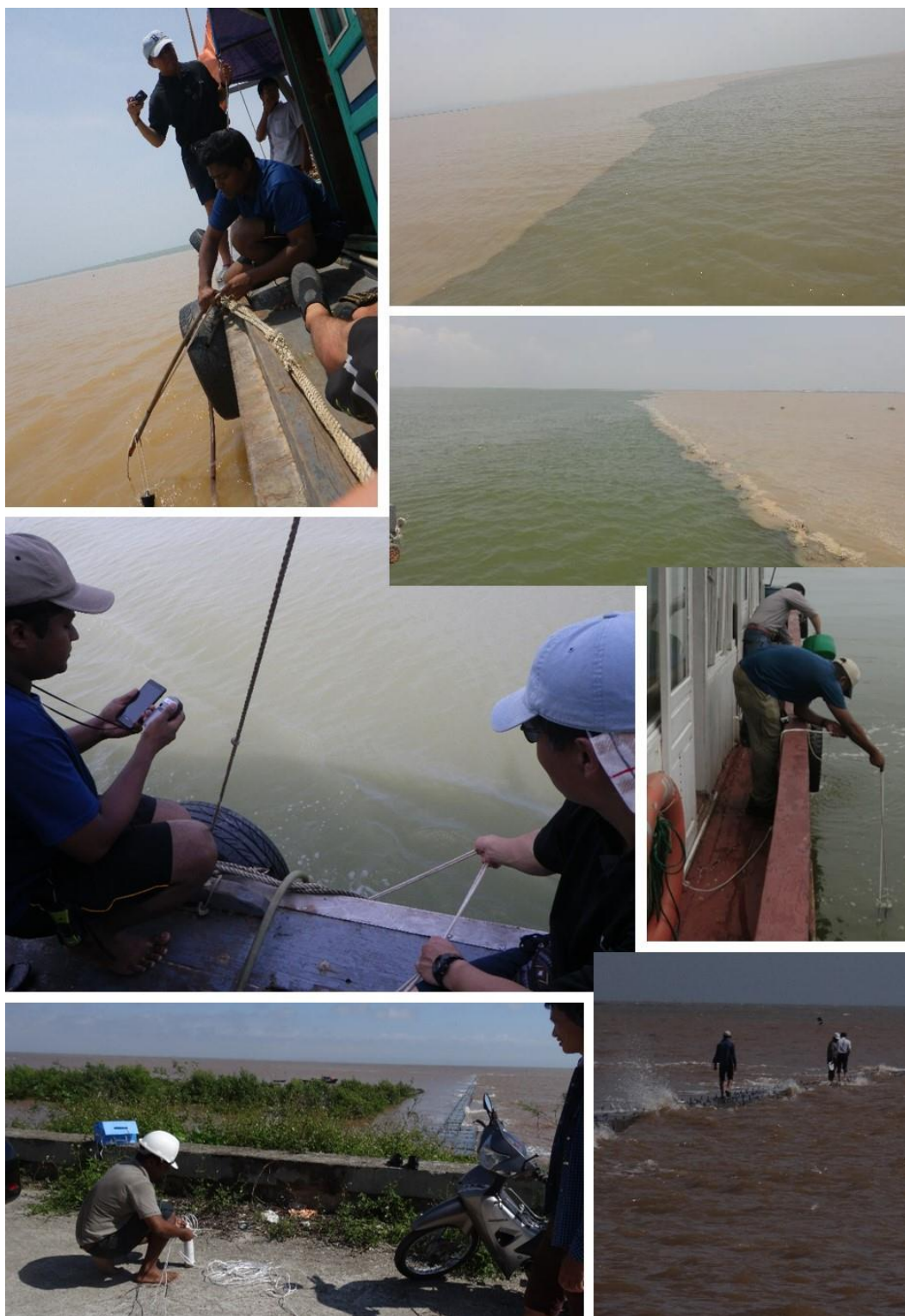
Figure 3.7 Photos of turbidity sampling

the clocks of the sensors and GPS so that we could easily match the measured turbidity and coordinates of the measured locations through the recorded time.

Figure 3.8 A map of all the sampling locations (background: Landsat image)

The location information and all the collected readings are documented in Appendix III. Figure 3.8 shows the map of all the collected samples during all the field excursions.

3.5.2 In-situ measurements of SSC

Measurements of the suspended sediment concentration (SSC) were also carried out at the same time as the turbidity measurements. The SSC samples were obtained at the places where considerable differences in the turbidity level were observed. To observe the characteristics in the dry and wet seasons, field surveys were carried out in March 2015 and February 2016 for the dry season, and July 2015, September 2015 and November 2015 for the wet season. The mouths of the Van Uc River and the Cam River, including Hai Phong Bay, were covered. The extent of the field survey highly depended on the weather conditions.

To measure the SSC, 500ml water samples were collected at locations where we observed the different concentrations of turbid water. At the same time, the turbidity was also measured. Figure 3.9 shows the SSC sampling and the on-site filtration sample.

Figure 3.9 Photos of turbidity sampling
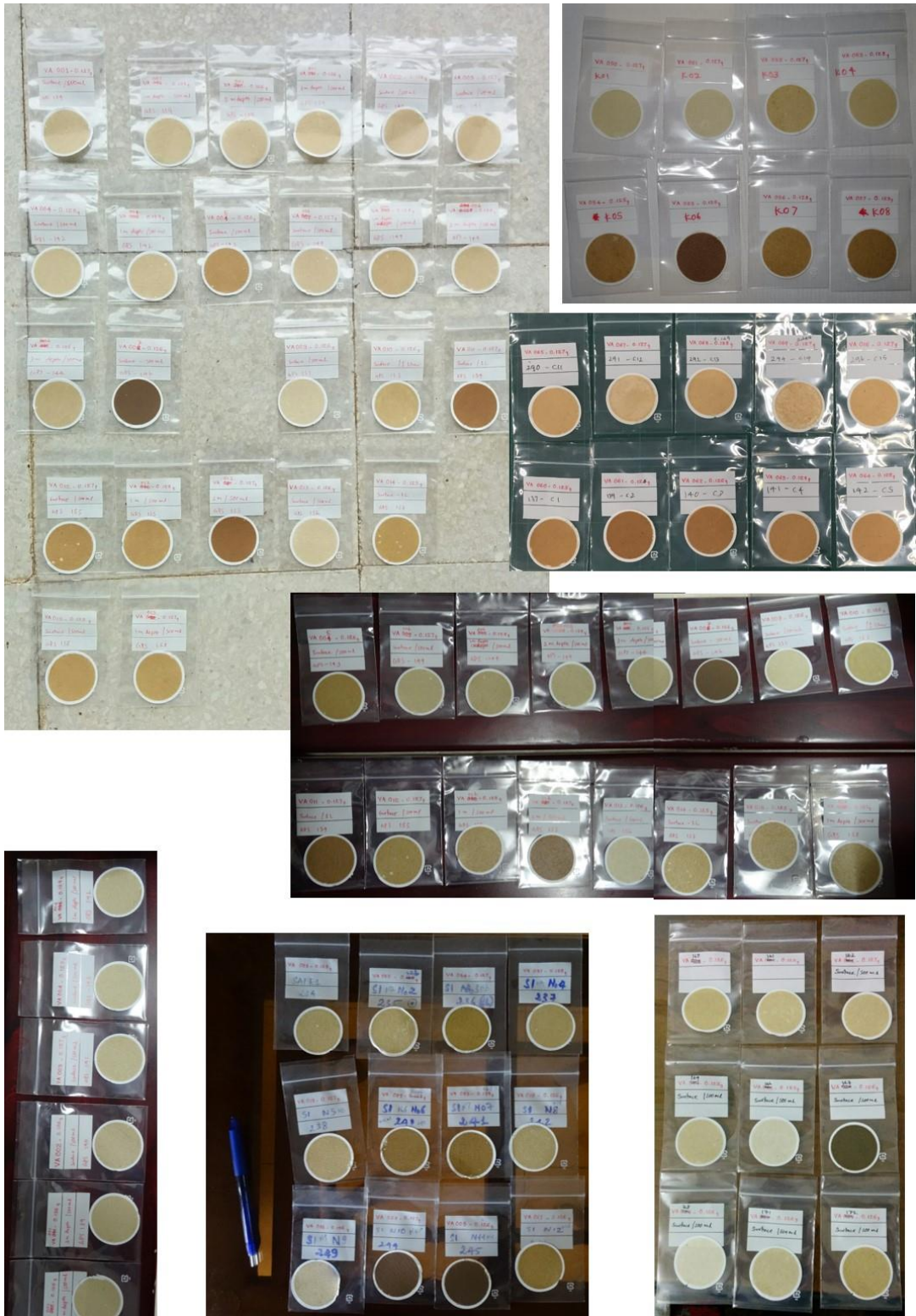
Figure 3.10 Photos of filtered samples

The portable filtration setup (bottom picture of Figure 3.9) was used to filter the samples at the study site. It consists of a vacuum pump to apply suction for filtration

of the highly turbid water. Pre-weighted glass microfiber filters (retention capacity of 0.7 μm) are used in the portable experiment setup. All the filter papers were stored in sealed plastic bags separately and brought to the laboratory to measure the SSC. Figure 3.10 shows some photographs of the filtered suspended sediments samples.

Several locations, especially the navigation channel in Hai Phong Bay were selected for depth-wise sampling. Figure 3.11 shows the filtered samples at the surface and at depths of 1m, 2m, and 3m.
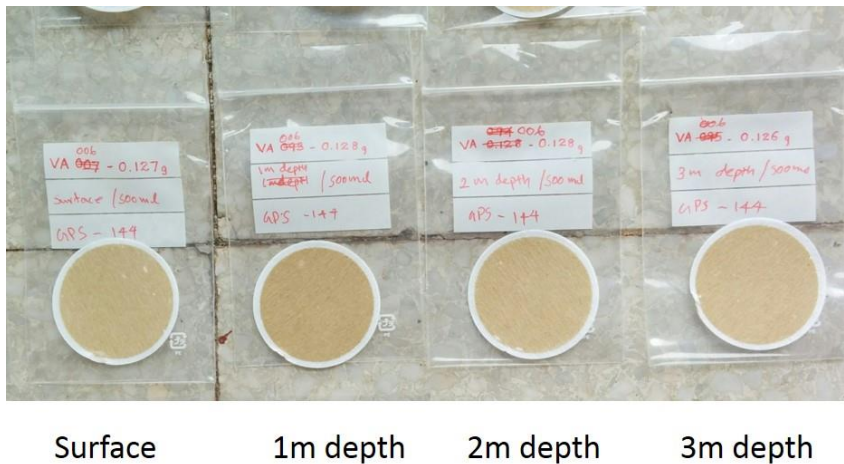
Figure 3.11 Depth-wise sampling

3.5.3 Laboratory experiment

Before measuring the weight, deionized water was thoroughly passed through the filter papers. The oven was set up at 220 ^{0}C and the samples were placed in it to remove any volatile objects on the filter papers. The samples were treated at a higher temperature for 15minutes then the samples were kept at 110 ^{0}C for another hour before the weights were measured. This procedure was repeated three times for all the samples to obtain the average weight of suspended sediments. Figure 3.12 shows some photographs during the laboratory experiment.

Figure 3.12 Sample preparation for weight measurements

CHAPTER FOUR

DEVELOPMENT OF SATELLITE-BASED MONITORING SYSTEM

4.1 Introduction

This section outlines the development of a satellite-based monitoring system for turbidity around the nearshore areas. All the procedures from scratch to the operation level are described and all the scripts developed in this study are attached as appendices. The unique cloud masking algorithm is one of the key sections of this chapter.

4.2 Automation of Data Download and Preprocessing

One of the main objectives of the system is to use all the archived MODIS satellite data for the analysis without manually selecting the "best images." The entire system should enable users to monitor arbitrary coastal areas without doing much prior preparation.

There are several ways to download the MODIS data based on processing levels. As we are interested in the level 2 and the whole archived data, the system should be able to download an arbitrary bulk data set out of the archives of MODIS. Among several tools available in USGS and NASA websites, this study selected the pyModis tool for the data download and preprocessing. The pyModis is a freely available tool based on the Python language (*www.pymodis.org*). It has several modules for preprocessing the MODIS data:

> *modis_download.py*: download MODIS data from NASA servers based on the specified product name and tile numbers.
>
> *modis_mosaic.py*: create a mosaic of all the specified tiles using MRT software or GDAL library.
>
> *modis_convert.py*: convert MODIS data to the TIF format and a different projection reference system. It is an interface to the MRT mrtmosaic software or GDAL library.
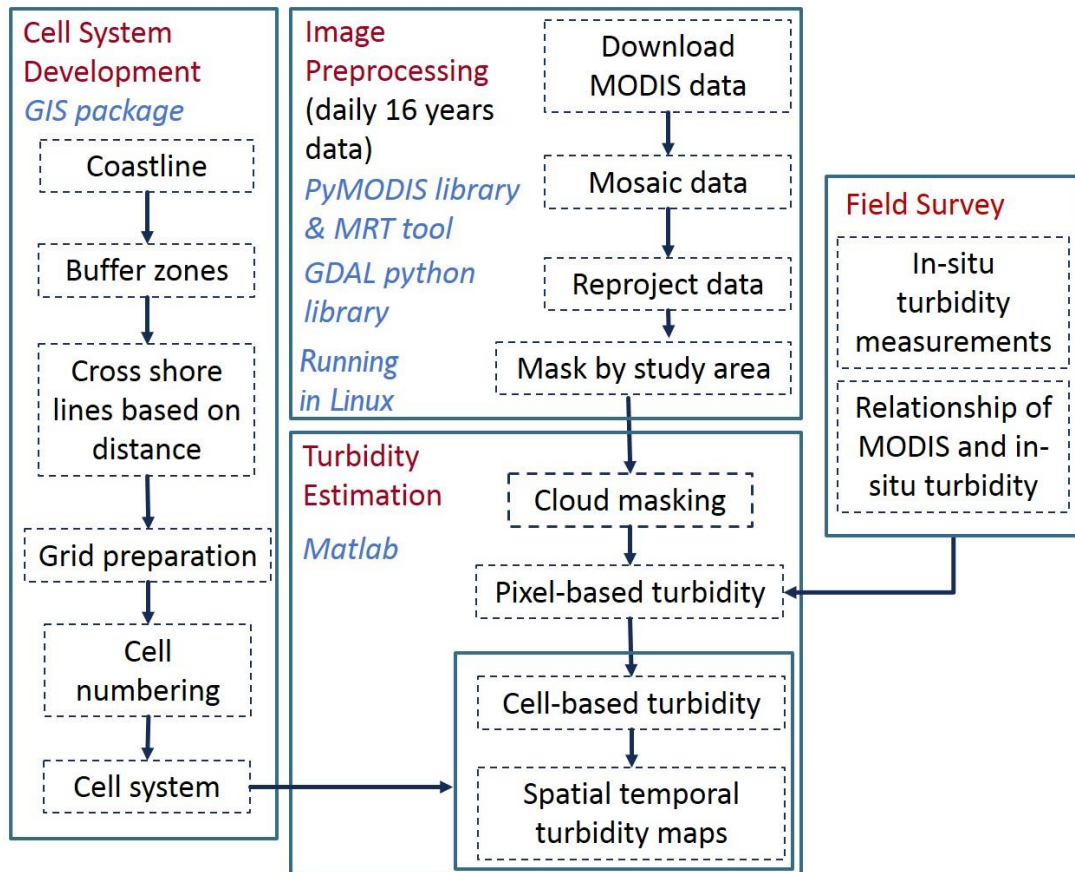
Figure 4.1 Schematic diagram of the monitoring system

Figure 4.1 shows the schematic diagram of the monitoring system. The pyModis tool is implemented in the Linux environment and executed through the Bash script. To complete the preprocessing of the MODIS data, a subset of the study area is necessary, but the pyModis library does not contain a module to subset an image. Therefore, the GDAL Python library (*www.gdal.org*) was used in the automated process in Bash script to subset MODIS images of the study area. The GDAL library is a Python package for various geospatial processing tasks.

The automated process up to this stage is documented in Appendix I. The next section of this chapter explains the cell system that was used in the monitoring system.

4.3 Relationship between Surface Reflectance and In-situ Turbidity

This study introduces a new fitting formula for estimation of the turbidity based on the in-situ turbidity data measured around Hai Phong Bay and the mouth of the Van Uc River. Daily MODIS images on the days of the field surveys were obtained, and the red band reflectance was extracted from the cloud-free pixels where the turbidity was measured in the field survey. Figure 4.2 shows the relationship between the MODIS red band surface reflectance and in-situ turbidity measurements. In the figure, the solid line indicates the following fitting curve of the relationship between the red band reflectance and the turbidity:

$$T = 23927(x - 0.097)^2 + 14.1$$
$$(0.097 \leq x \leq 0.15)$$

(1)

Here, T is the modeled turbidity (FTU), and x is the red band (band 1) reflectance of MODIS. It should be noted that this fitting formula can be applied within the range of 0.097<x<0.15. Applicability of the present formula in the range of higher turbidity needs to be validated with additional data. All the collected data (cloud free) with GPS locations are compiled in Appendix II.
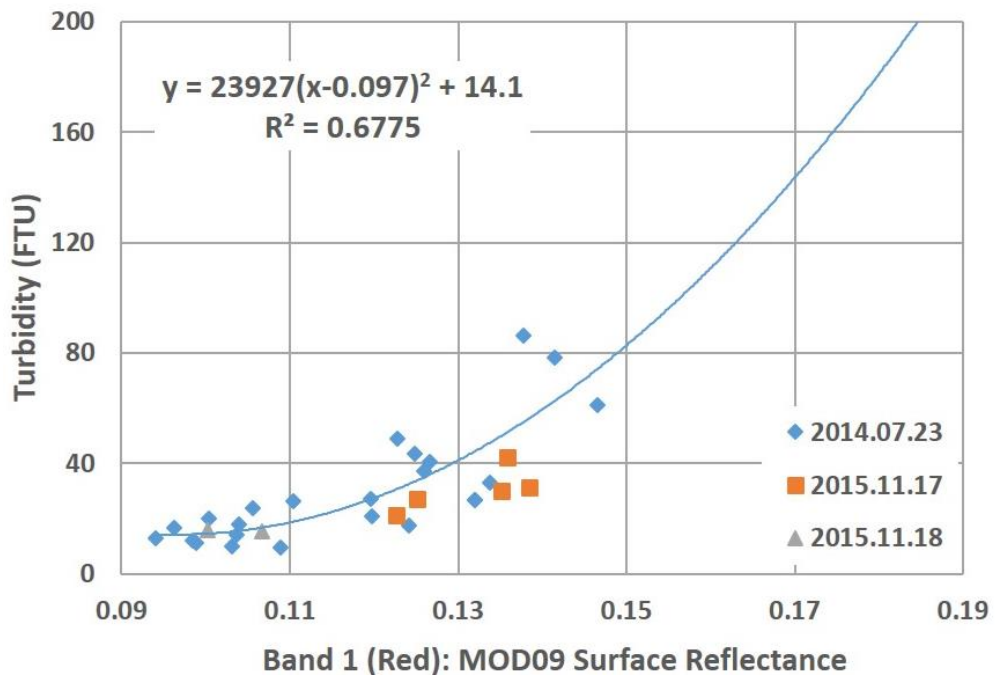
Figure 4.2 Relationship between red band reflectance of MODIS and corresponding in-situ turbidity measurements.

4.4 Relationship Between Turbidity and SSC

The measured suspended sediment concentration (SSC) and measured in-situ turbidity data were used to obtain the relationships. Figure 4.3 shows the relationship between measured turbidity and the SSC.

$$SSC = 1.2597\,x - 3.9096 \qquad\qquad (2)$$
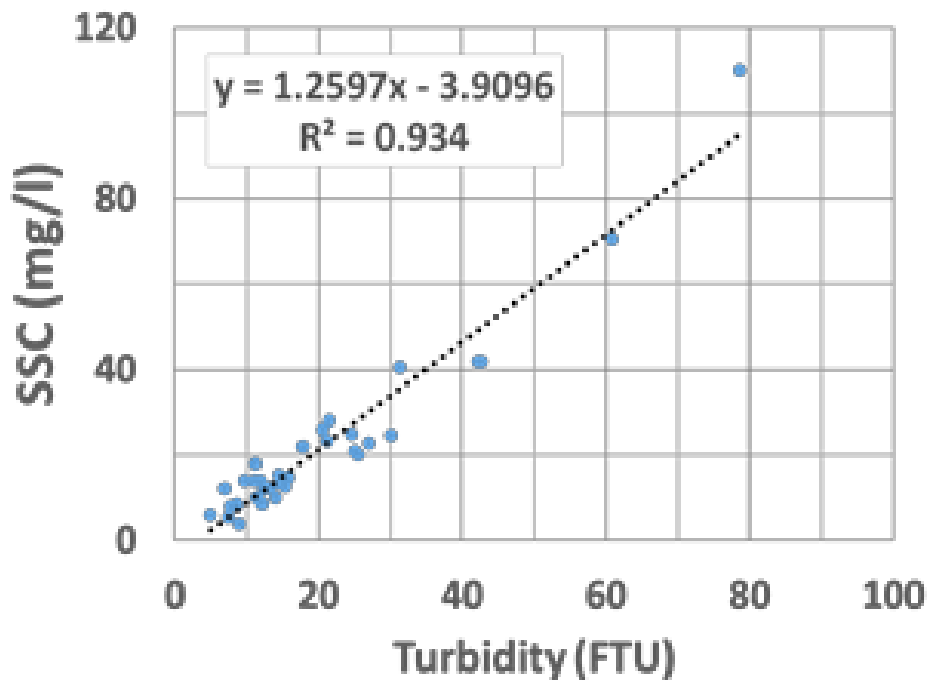
Figure 4.3 Relationship between measured turbidity and suspended sediment concentration

4.5 Pixel-based Data Extraction and Turbidity Maps

Figure 4.4 shows the derived turbidity maps of a selected date from December to January (dry season) and June to September (wet season) in 2014 around the mouths of the Ma and Day Rivers. The observed different levels of turbidity and patterns over the past 16 years are analyzed and discussed in-depth in the following chapter.
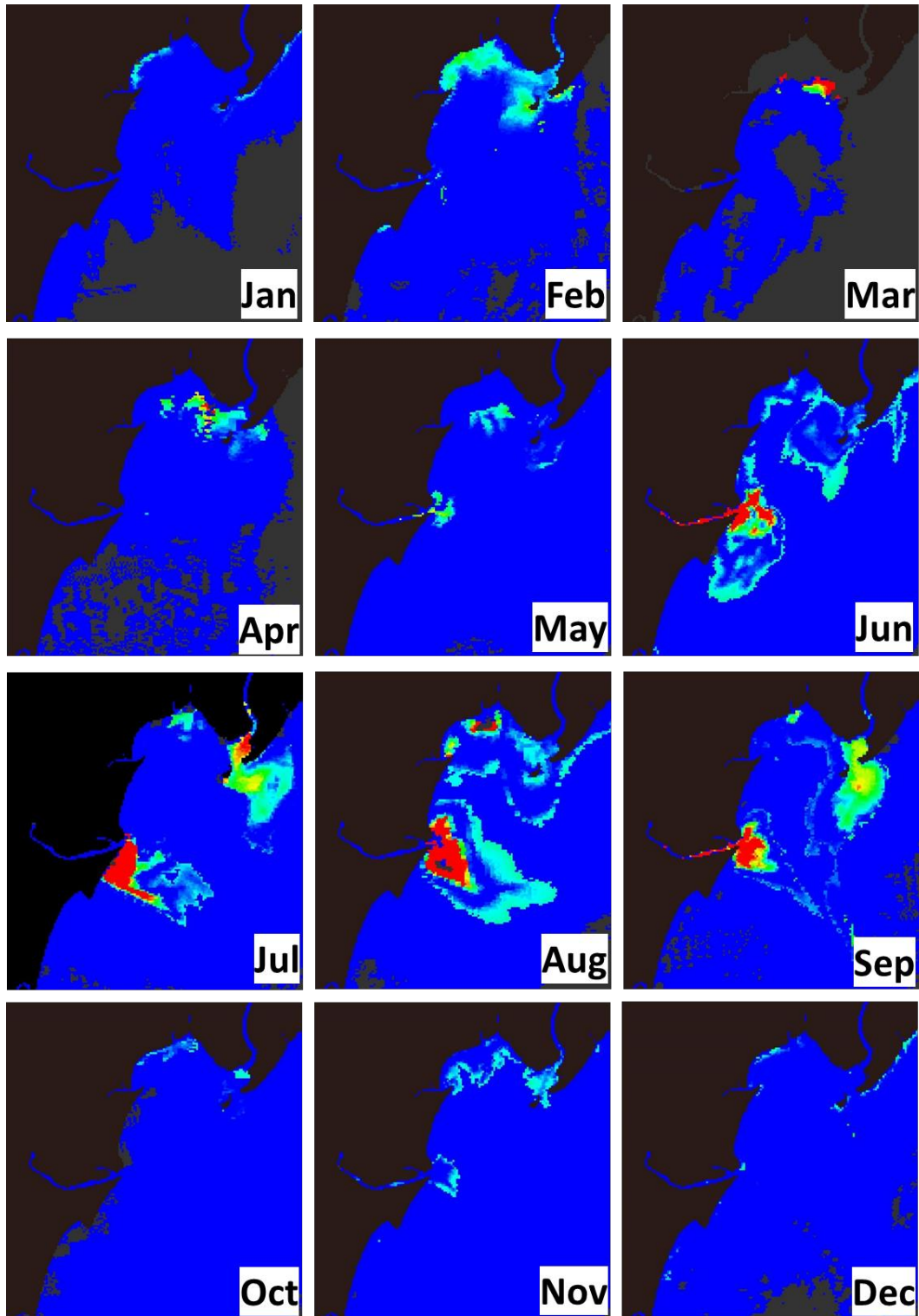
Figure 4.4 Turbidity maps of each month (Dec-Jan: dry season and Jun-Sep: wet season)

4.6 Introduction of Cell System

4.6.1   Background

One of the main objectives of the monitoring system is to best use the MODIS images for monitoring the water surface turbidity even though the obtained data is partially missing. The main limitation of the data is the cloud coverage. The sun glint phenomenon and data missing due to MODIS' polar orbit path occur relatively less frequently than the cloud coverage. The cloud masking is therefore one of the key components of the monitoring system, and is discussed in the coming sections from 4.7 to 4.8 of this chapter.

Figure 4.4 illustrates the status of the MODIS images in July 2014. Those images are selected to explain the limitations of the input data of the monitoring system and how important it is to conceptualize a method to utilize the available parts of the data even though the other parts are missing.

As seen in Figure 4.5, images of July 20th, 21st, 27th, 28th, and 31st are covered by clouds and could not be used in the analysis. The image on July 23rd is missing due to the path of the MODIS orbit. Images on July 22nd and 29th represent the occurrence of the sun glint. Images on July 24th and 31st are the best images among the selected images.

While thin cloud and haze appear in the images on July 25th and 26th, the turbid plume is also well recognized even though the area is mostly covered by thin cloud or haze. On the other hand, the observed horizontal length scale of the turbidity variation appears to be much larger than the pixels' size (250m). That is the main concept for the cell-based system. The pixel-based turbidity extraction method produces turbidity maps of all the pixels but misses the turbidity data on any pixel covered by cloud. Since the horizontal scale of the turbidity patterns is much larger than the pixel's size, the missing turbidity data may be reasonably represented by those on the pixels nearby. Based on this assumption, this study introduces a unique cell system to represent spatial-temporal turbidity patterns. Each cell contains more than 16 pixels and the averaged turbidity value is obtained over each cell. Even if the cell is partially covered by cloud, this study computed the average turbidity based on the rest of available turbidity data on the cell. The next section further discusses the development of this unique cell system.

July 20	July 21	July 22	July 23
July 24	July 25	July 26	July 27
July 28	July 29	July 31	July 31
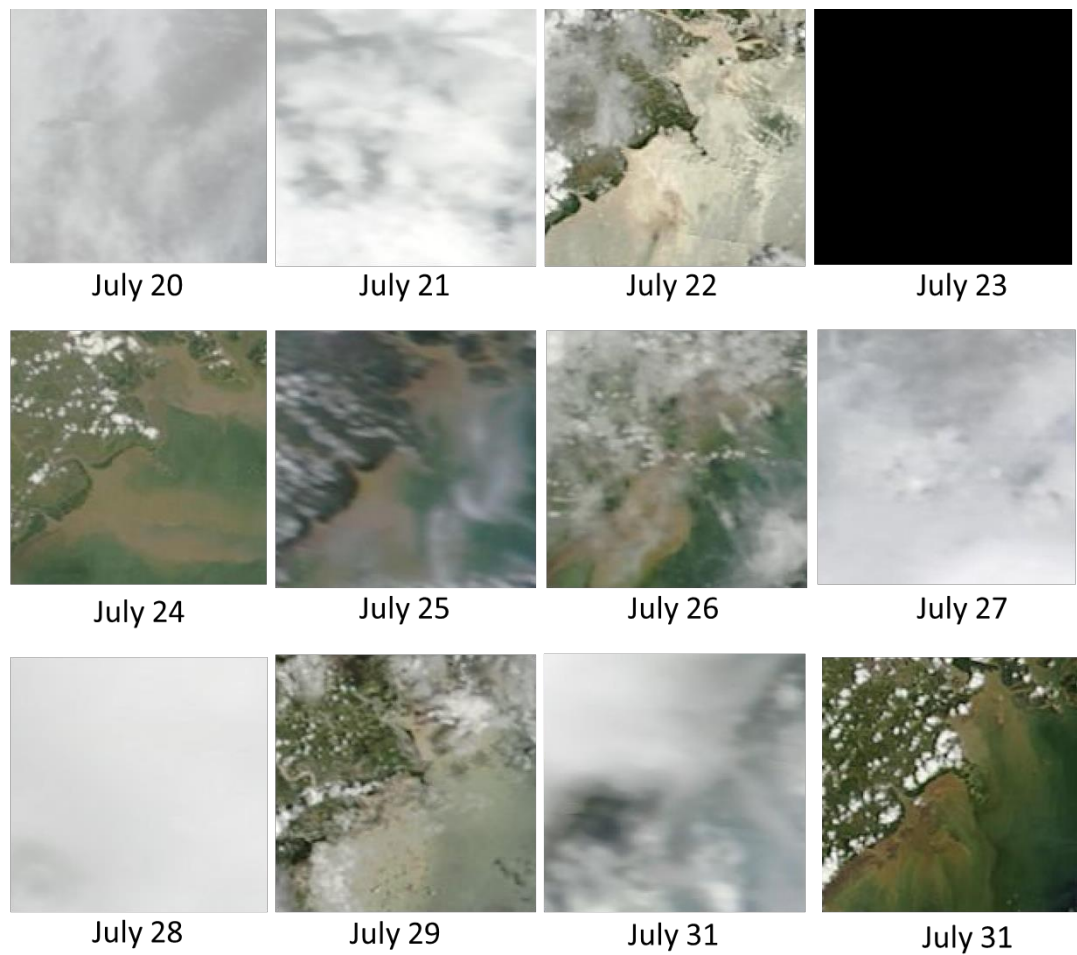
Figure 4.5 Status of MODIS images in study site in 2014, Vietnam

4.6.2 A unique cell system

Figure 4.6 (a) shows the schematic diagram of the cell system and (b) represents the derived turbidity output. The alongshore boundary of the cell was determined parallel to the shoreline and the first set of cells implemented around 500m away from the shoreline. That is to avoid the contribution of pixels that represent land and the wave-breaking zone. In the wave-breaking zone, the surface reflectance tends to reach very high values due to diffused reflection. Several GIS tools were utilized to develop the entire cell system for the study area; Figure 4.7 shows the entire cell system
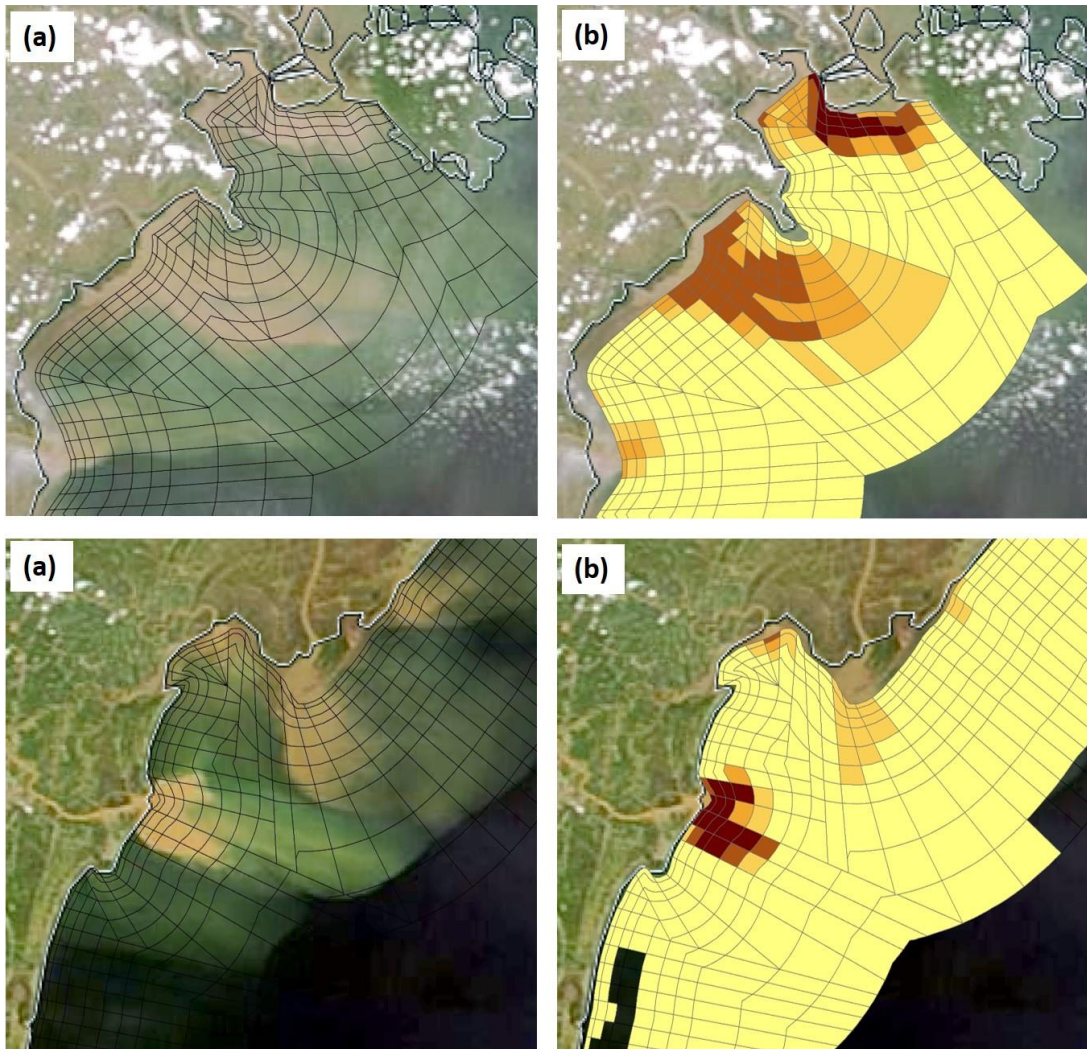
Figure 4.6 (a) shows the schematic diagram of the cell system; (b) derived turbidity output in July 24, 2014 (Terra)

4.6.3 Identification Numbers of the cells

The alongshore length of a cell was kept constant and was 2 km in the Vietnam study site. The cross-shore width of the cell defines differently towards offshore. In the Vietnam study site, 500m, 1km, 1km, 2km, 2km, 2km, 2km, 5km, 5km and 5km widths were maintained from nearshore to offshore. This length and these widths were decided considering how much detail of the turbidity patterns would be needed for further analysis at each location.

Five digit identification numbers (noted as ID, hereafter) were introduced for each cell; the first three digits represent the alongshore location, and next two digits represent the cross-shore direction. This ID is used in the Matlab script to locate an

interested cell for assessment of turbidity variation. Figure 4.8 illustrates the naming convention of the cells.
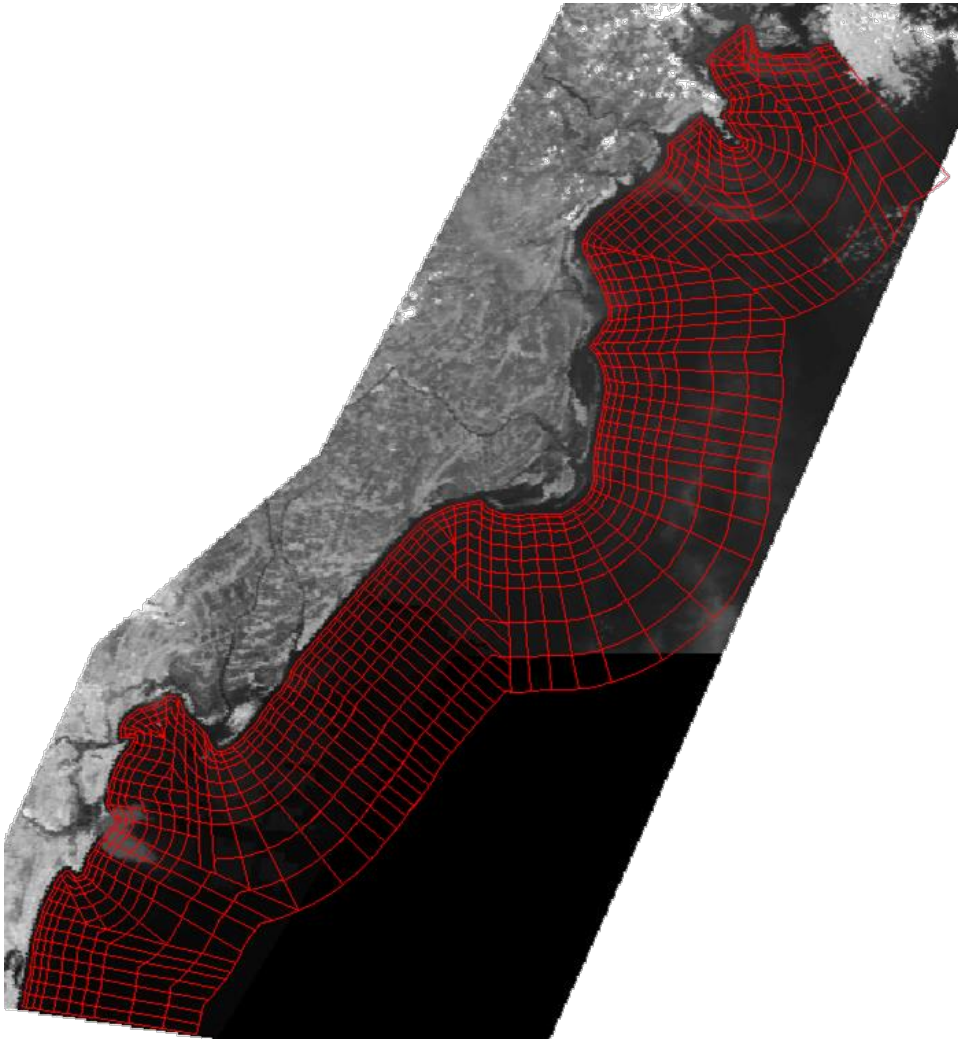
Figure 4.7 The entire cell system developed for the study site, Vietnam
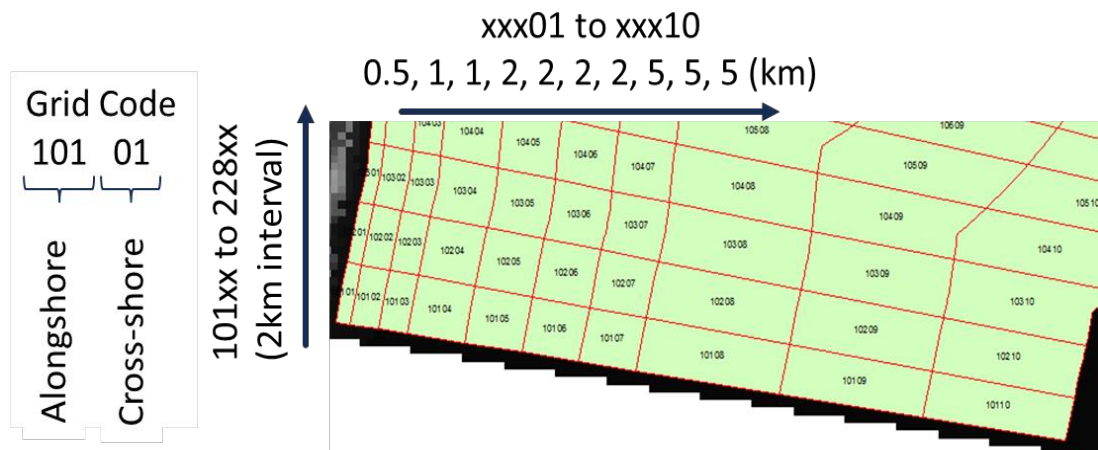
Figure 4.8 The naming convention of the cells

4.7 Cloud Masking

This section describes a newly developed cloud masking technique which is capable of automatically masking out clouds in the MODIS data.

4.7.1 Background

Existing cloud masking techniques, which are developed for open ocean applications, perform well with the assumption that marine reflectance in the near-infrared (NIR) band is equal to or nearly equal to zero. Basically, most of the global ocean color remote sensing applications use the threshold value on the NIR to distinguish clouds and water pixels (Nordkvist et al., 2009; Robinson et al., 2003). The open ocean water is considered to be black in the NIR band and that leads to better cloud masking performance.

Since our focus is cloud masking around the nearshore areas (case-2), suspended matter causes considerable reflectance even in the range of NIR (Farooq, 2011). A simple threshold of NIR is therefore no longer applicable for appropriate cloud masking. This simple threshold, for example, may end up by masking out cloud-free high turbid pixels and thus lose the observed available turbidity data.

Many studies have been conducted to mask clouds around coastal regions (Wang and Shi, 2006; Nordkvist et al., 2009; Liu and Liu, 2013). These models use multiple band data but differ from each other in their specific usage of different band data and also their focusing observation period. As outlined in the next sub-section, all those

studies differ from the intention of this study in the following features: (i) the intention to automate the cloud masking for the entire data set; (ii) the consideration of only nearshore water (excluding land); (iii) to the evaluation of qualified pixels under the cell-based system (to produce the average value); (iv) the capability of having cloud masking based on a 250m spatial resolution.

4.7.2 Review of existing cloud masking methods

The dedicated MODIS product for cloud masking, MOD35, is generated by comprehensive statistical analysis for each observation to determine whether it is cloudy or clear using 19 out of the MODIS 36 bands (Ackerman et al., 1998). The product we used for the analysis (MOD09) is also delivered with one quality control (QC) layer which indicates the presence of clouds, aerosols and snow. The QC layer is built up based on the MOD35 product. Although the MOD35 uses advanced cloud screening techniques, uncertainties of the approach still lead to poor cloud detection performance that causes inconveniences in MOD09 products (Liu and Liu, 2013). In most of the cases, for example, the MOD35 cloud mask product tends to over-detect the cloud and thus to lose the number of usable pixels for analysis.

Nordkvist et al., (2009) proposed an algorithm to mask clouds in two steps for MODIS and the Sea-viewing Wide Field-of-view Sensor (SeaWiFS) data in case-2 waters. The first step uses a threshold value on the NIR data to determine cloud-free pixels. In the second step, data from four bands (blue, green, red and NIR) are used to categorize cloudy pixels based on the minimum and maximum surfaces. Moreover, this algorithm also calculates cloud thickness for better masking out of the thin clouds.

Liu and Liu, (2013) also proposed an algorithm to mask clouds based on MODIS bands 1, 2, 3 and 7. This study has been carried out to mask clouds over both the land and ocean. This study uses an assumption that there is an inflection between the time series of clear sky and cloudy pixels.

All of the previous studies use several bands and in-depth analysis for cloud detection which is quite difficult to execute for the daily archive data for 16 years and most of the products have a coarser resolution. Therefore, this study proposed a new algorithm to mask cloud specifically for the costal studies and is explained in the following section.

4.7.3 Newly introduced cloud masking algorithm

This study proposes a step-wise cloud masking method which avoids overdetection of the cloudy pixels, especially around the nearshore area with a turbid water surface. The land portion of an image is always excluded at the beginning and this helps to reduce more heterogeneous surfaces in mixed pixel classification. Basically, different levels of turbid water, clear water, cloud and haze are the main features that need to be considered in the present cloud masking technique.
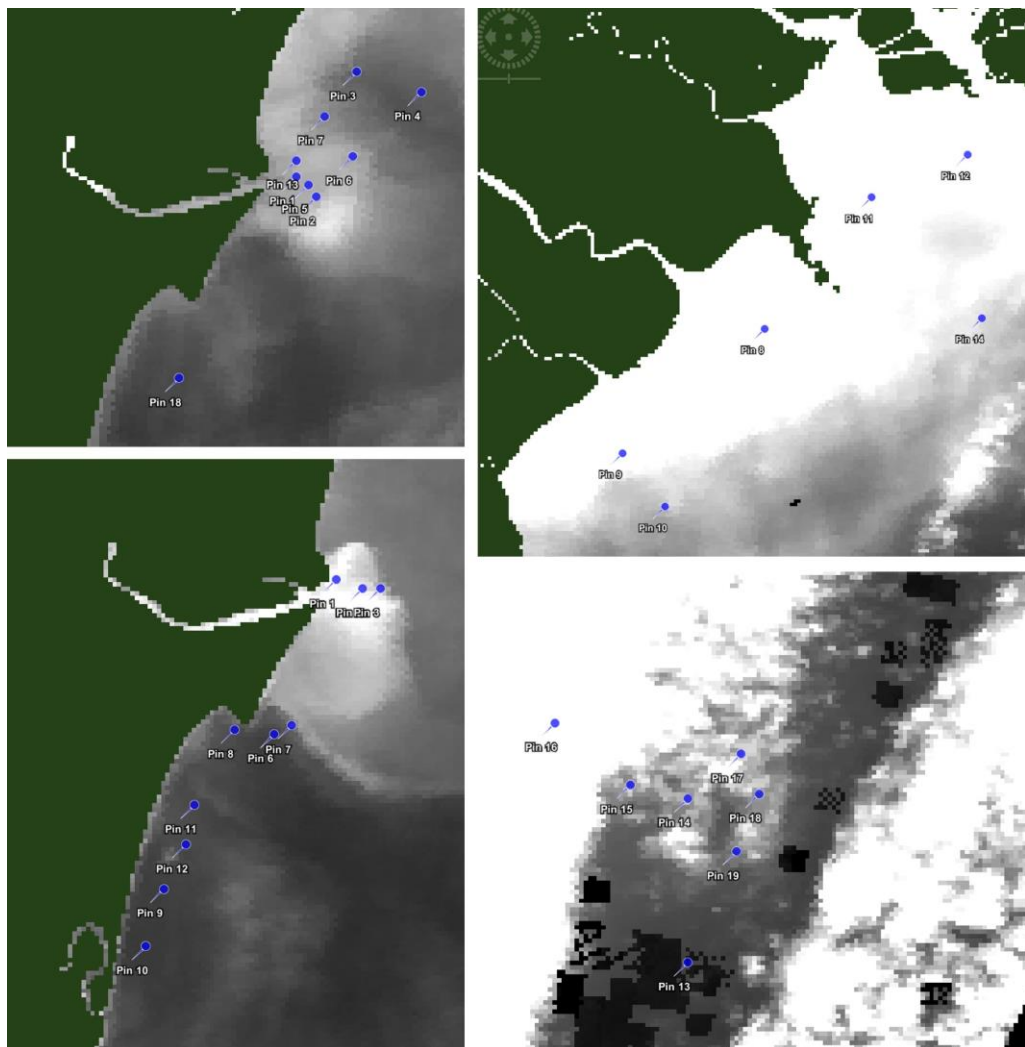
Figure 4.9 Selected POIs for comparison of Red and NIR band response

To find a formula for determination of cloud/non-cloud pixels based on band 1 and band 2 data of MOD09, the pixels' values of cloud, partial cloud and sea water with different turbidities were sampled out of several MODIS images. Figure 4.9 shows the selected points of interest (POI) where band 1 and band 2 data were sampled. Table

4.1 shows the featured classes used for determination of the formula. The images were selected to cover the clear images without turbidity and clouds, cloudy images and mixed images. Both the Aqua and Terra satellite MODIS images were used for the threshold identification. This procedure is mainly conducted based on visual interpretation with the help of two online image viewers; the NASA MODIS world view (https://worldview.earthdata.nasa.gov) and Google Earth Engine MODIS dataset (https://explorer.earthengine.google.com).
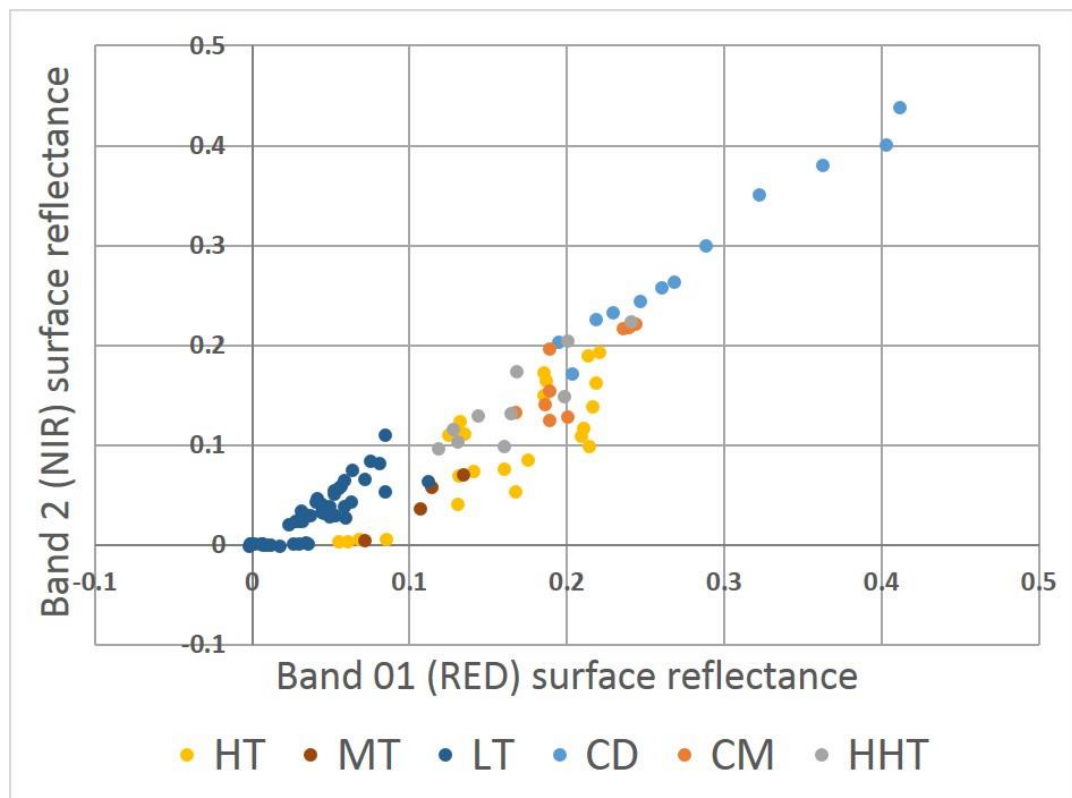
Figure 4.10 Red and NIR response of POIs

Table 4.1 Categories of POIs

CODE	Description
HT	High turbidity
MT	Medium turbidity
LT	Low turbidity
CD	High dense cloud
CM	Medium dense cloud
HHT	Haze high turbidity (turbid water under the haze)

Table 4.1 identifies the status of the categorized abbreviations shown in Figure 4.10 and Figure 4.11. As seen in Figure 4.9, high dense cloud (CD) is easy to separate from other classes but medium dense cloud (CM) is mixed with the high turbidity (HT) pixels. Therefore, for better separation of MT from CM, a band ratio is proposed using bands 1 and 2

$$Index\ ratio\ = \frac{abs(band\ 1 - band\ 2)}{band\ 1}$$

Figure 4.11 shows the response of the selected POI of different classes for the proposed index ratio and band 1. The proposed new algorithm is based on the step-wise separation of cloud from other classes of interest. The separation of the suitable pixels for the analysis is proposed in this section:

1. Band 1 surface reflectance > 0.25; mask out as CD (area A of Figure 4.11).
2. Band 1 surface reflectance < 0; error pixels due to atmospheric correction are masked out as "No data".
3. Band 1 surface reflectance < 0.097 assigned as 14 FTU; below this level the relationship of turbidity and red band reflectance is not stable.
4. Index ratio < 0.25 and band 1 surface reflectance > 0.17; mask as cloud (area B of Figure 4.11) and assign CD.
5. Remaining pixels are regarded as pixels without cloud and are used for estimation of turbidity based on the developed formula (Eq. (1) determined in Section 4.3).

Many days of MODIS natural color images with different conditions of cloud status were used to test the developed algorithm and to define the reliable threshold value for the index ratio. There are still some turbidity pixels masked out with cloudy pixels but this has less influence on the analysis due to the cell-based system. Figure 4.12 shows the performance of cloud masking in the Japanese study site.
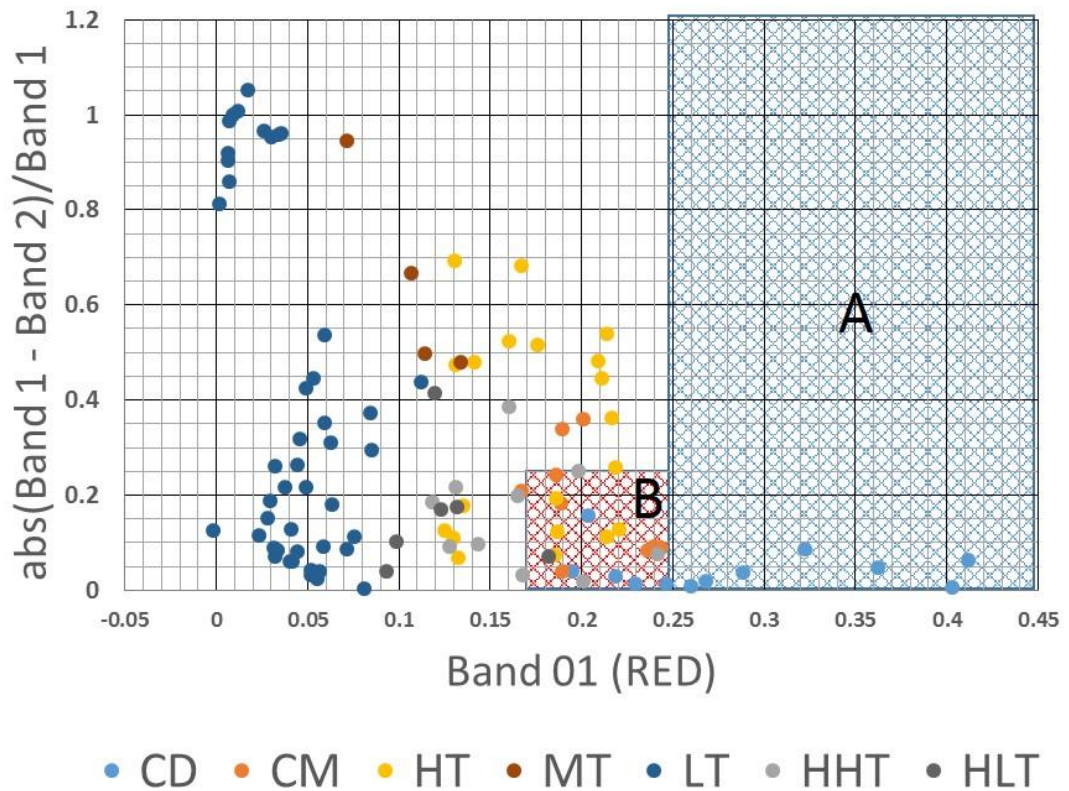
Figure 4.11 Index ratio and band 1 response of POIs

4.8   Cell-based Data Extraction and Analysis

The data extraction and turbidity calculation are developed in the Matlab computing environment. The coordinates of each cell are used to obtain the turbidity value and the average value of turbidity of the pixels in a cell is assigned to each cell. The process is automated for all the cells and for all the input images over 16 years. Finally, each cell containing the daily turbidity for 16 years (except for cloudy days) is obtained. Figure 4.11 shows the main steps involved in the cell-based data extraction.
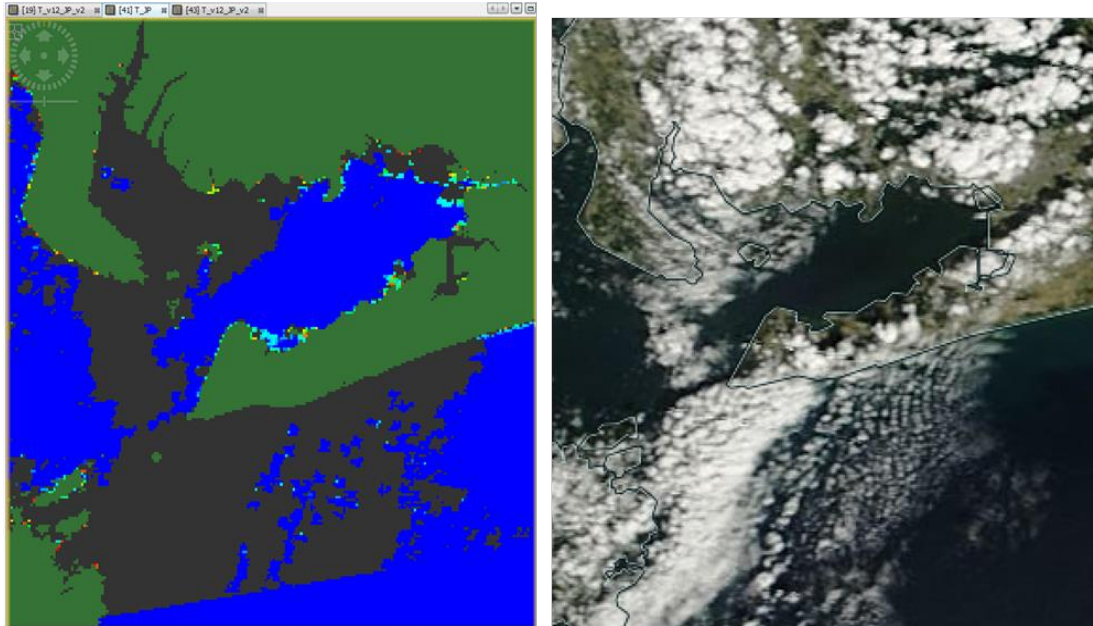
Figure 4.12 performance of cloud mask in Japan study site (Green color: land mask; left: turbidity map with cloud mask (gray color); right: MODIS natural color image
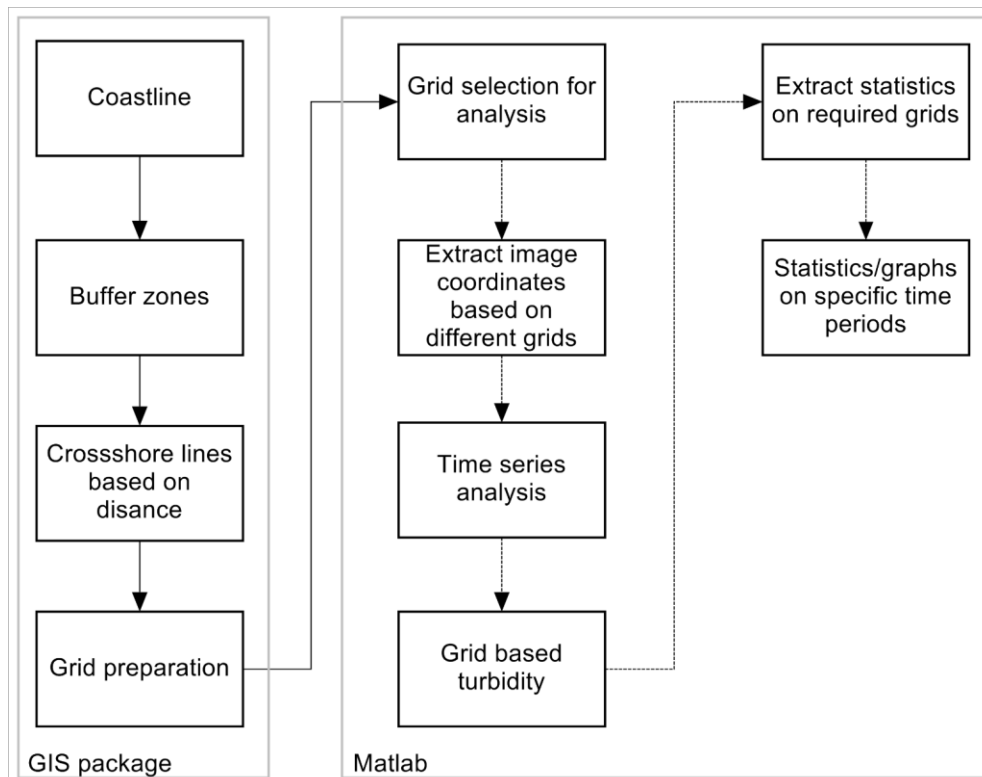
Figure 4.13 Schematic diagram of data extraction

SPATIAL TEMPORAL SUSPENDED FINE SEDIMENT DISCHARGED PATTERNS

5.1   Introduction

The extracted fine sediments (turbidity) data over the past sixteen years are presented by different means with maps and figures in this chapter. The suspended fine sediment patterns were analyzed at different time intervals such as daily, monthly, yearly and different seasons. Several rivers were considered for analysis of the area of the extent of the turbidity over the period based on different levels of turbidity. Moreover, a later part of this chapter focuses on the contribution of the turbidity plume to the alongshore direction.
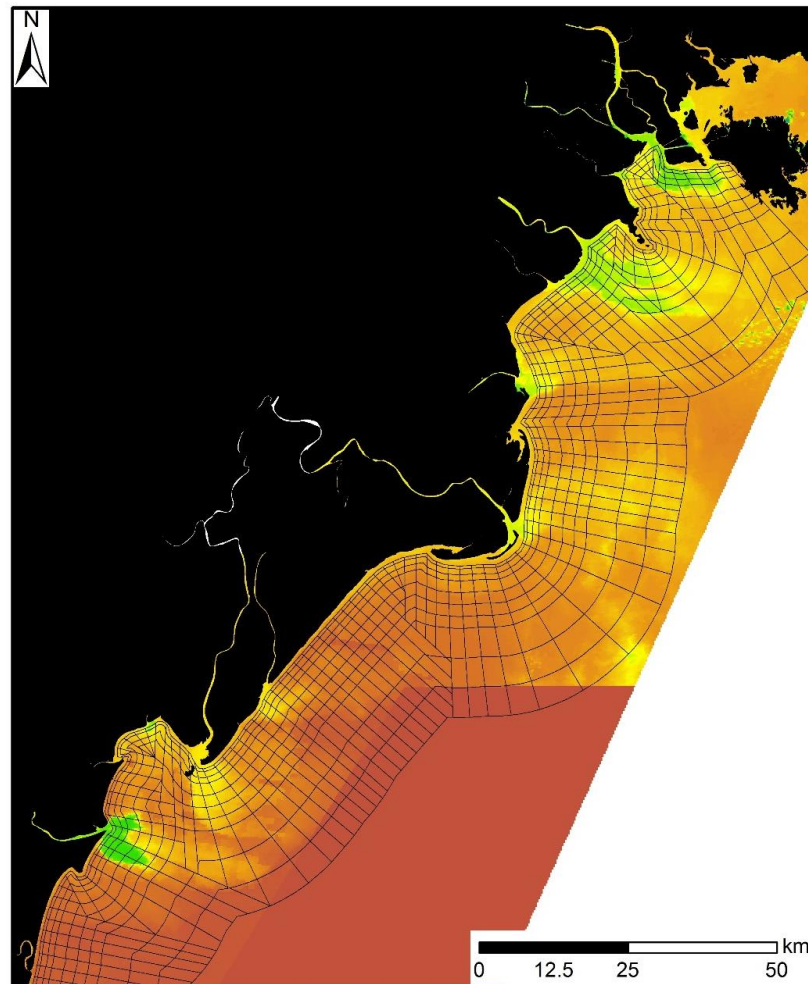
Figure 5.1 Map of cell systems and locations where the turbidity shown in Fig 5.2 was obtained

5.2   Investigation of Data Availability

To investigate the feasibility of the present monitoring system, temporal and spatial distributions of estimated turbidity were first extracted. Figure 5.1 shows the cell system introduced in this study with identification numbers. Based on each of MODIS data, estimated turbidity was extracted from the cells along the coast closest to the shoreline. Figure 5.2 then shows the color maps of extracted turbidity along the entire coast line of the study area, i.e., from Hai Phong to the south side of the Ma River mouth. In the figure, the vertical axis indicates the identification number of the cell along the coast and the horizontal axis indicates the Julian dates of the year of 2015. Since MODIS observes the target site twice a day, two different turbidity data at the same cell are plotted with avaerage value in each date. In the figure, blanks (white color) represents missing data due to the presence of clouds or other image preprocessing errors (atmospheric correction).
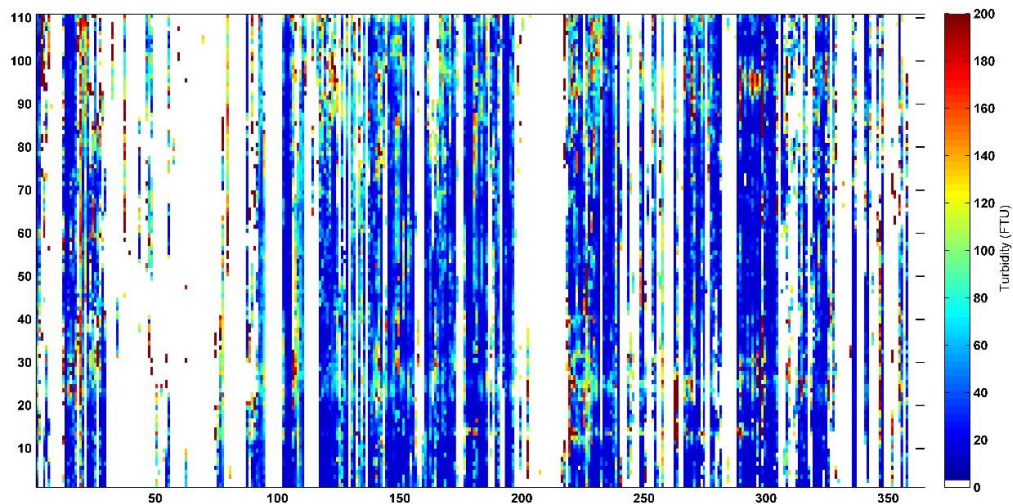
Figure 5.2 Daily alongshore turbidity from south of Ma River to Hai Phong

Similarly, Figure 5.3 (a)-(d) shows sixteen years of daily turbidity along the entire coast. As seen in these figures, it is found that high cloud coverage frequently appears during the dry season around February (Julian dates: 32 to 59) and March (Julian dates: 60 to 90). On the other hand, it is also seen that the MODIS-based observation reasonably captures most of the days and the coastal area from March to October, including the rainy seasons. Based on this frequency of the data availability, it may be reasonably concluded that the yearly or monthly average of the turbidity data in each cell reasonably represents the overall characteristics of the turbidity

distributions of the target site. This set of figures, thus, may be rather useful for assessing the feasibility of the MODIS data coverage for other applications than comparing the relative differences of the turbidity patterns.
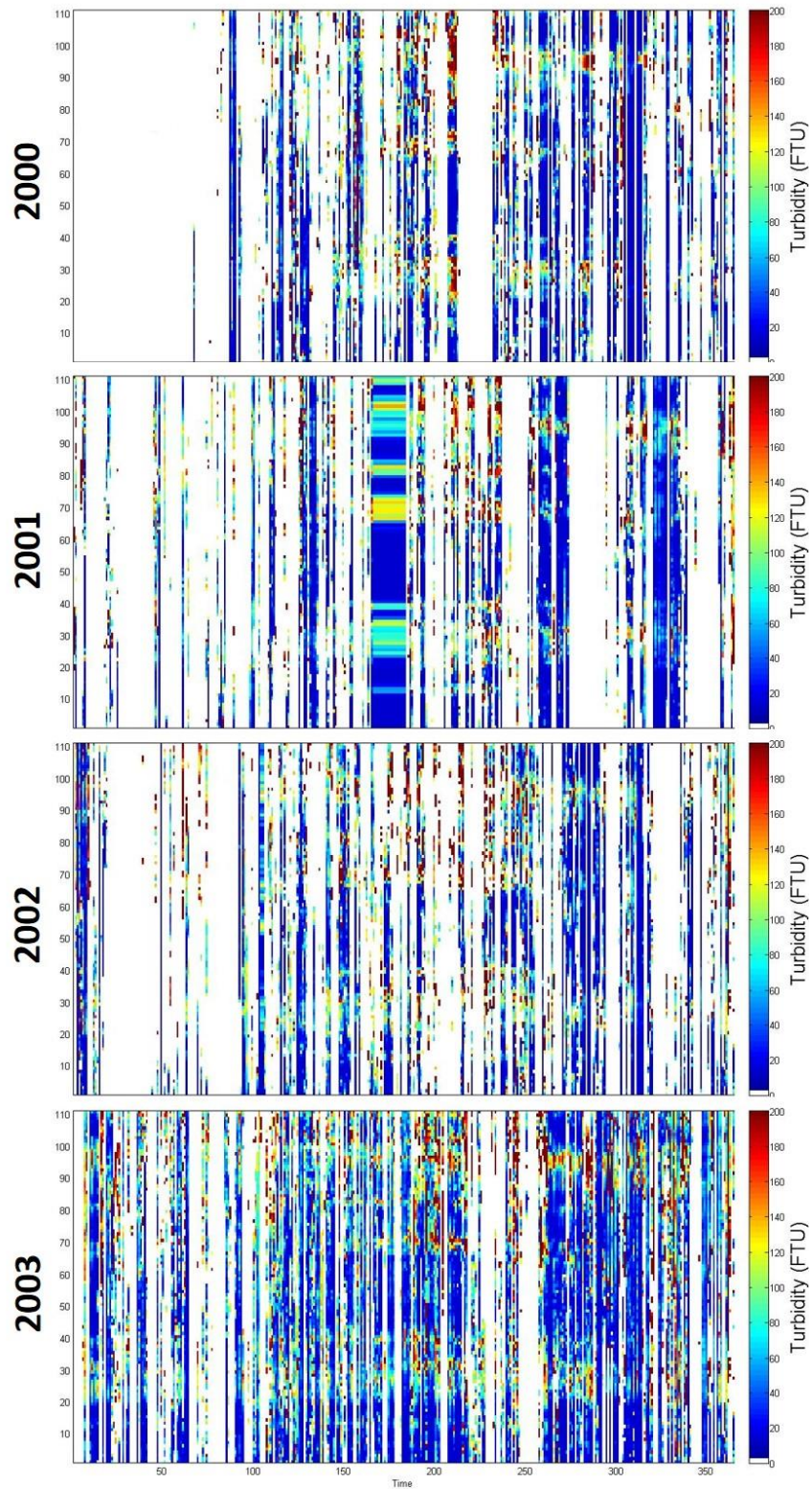
Figure 5.3 (a) Daily alongshore turbidity from south of Ma River to Hai Phong
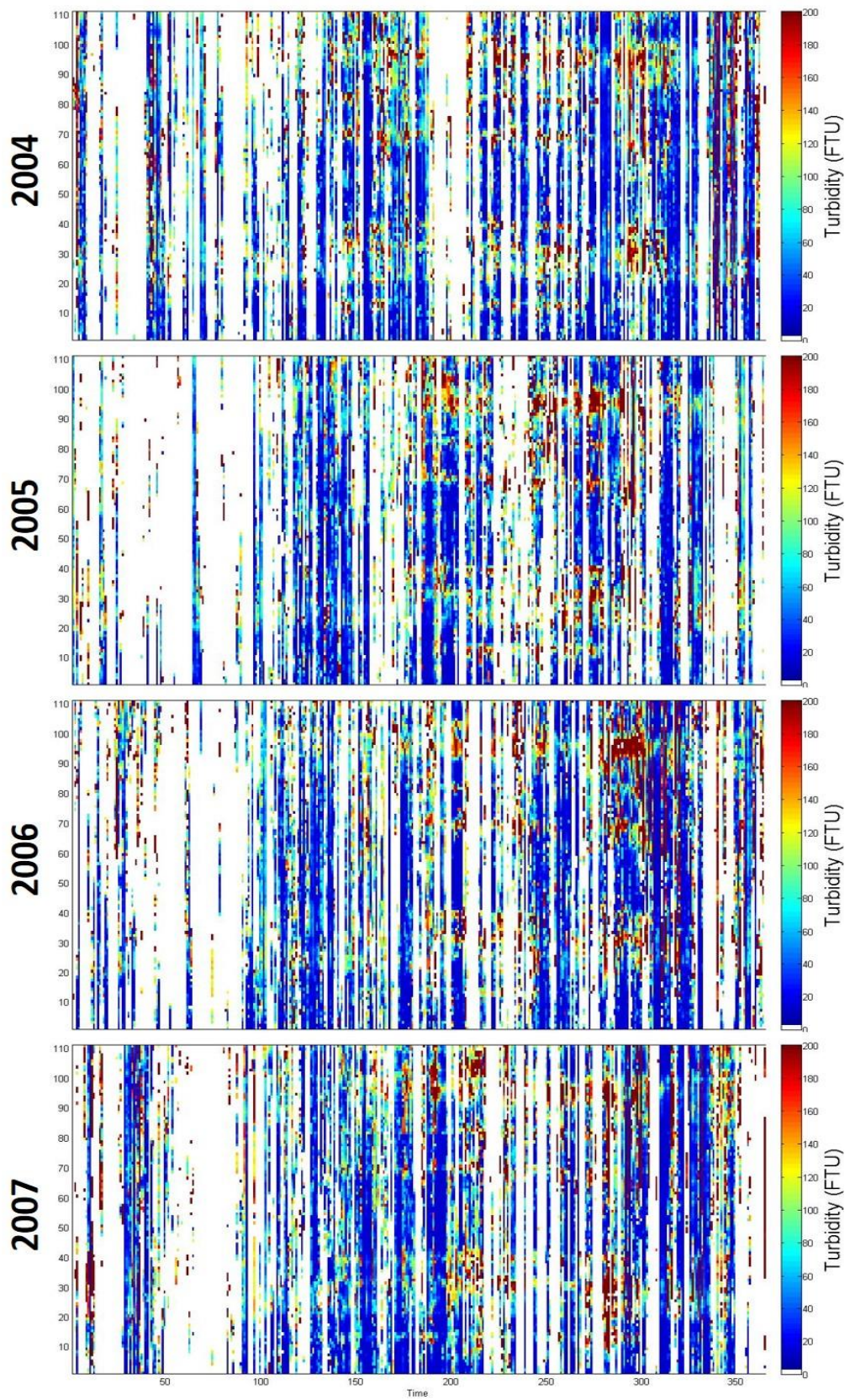
Figure 5.3 (b) Daily alongshore turbidity from south of Ma River to Hai Phong
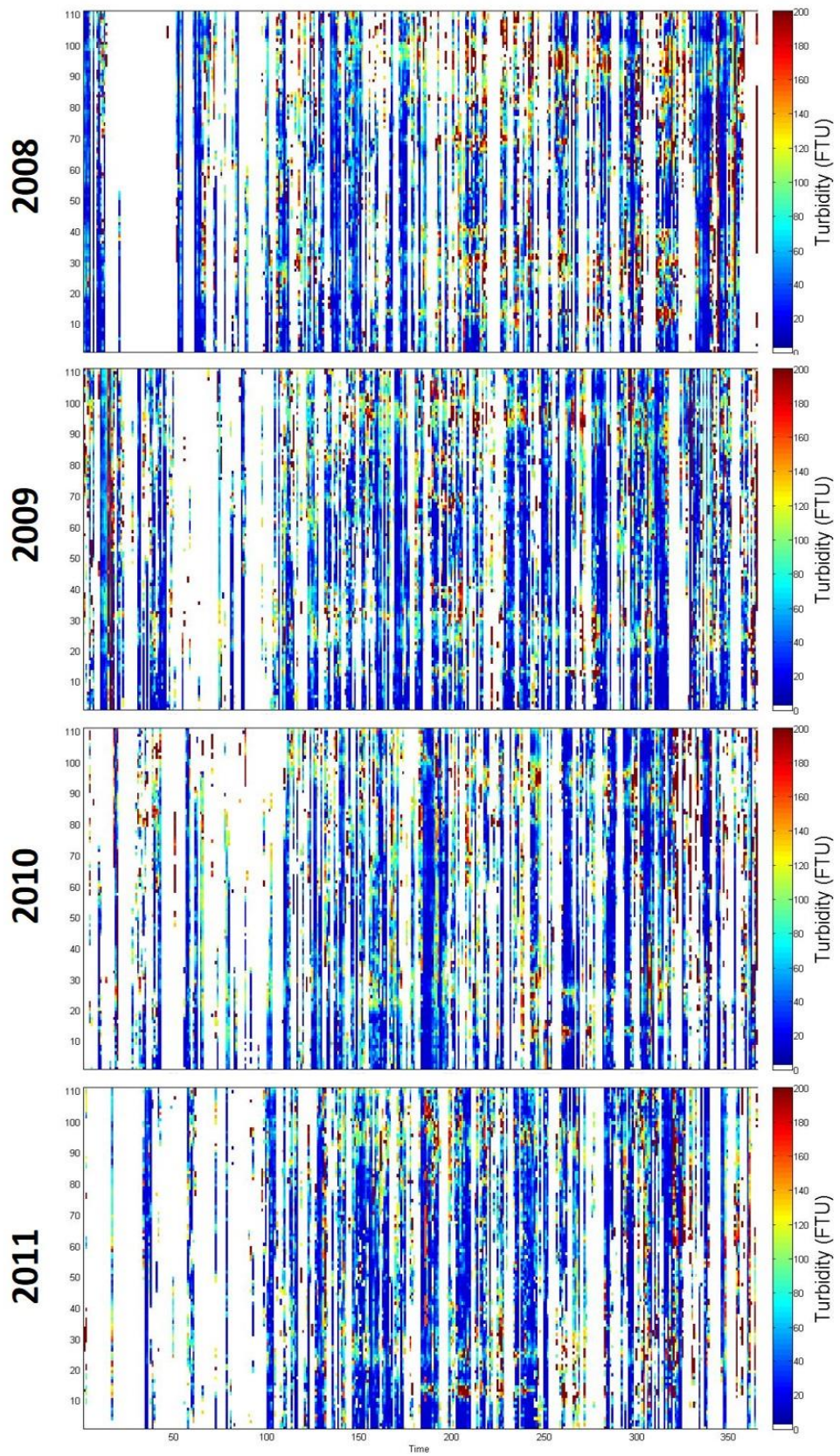
Figure 5.3 (c) Daily alongshore turbidity from south of Ma River to Hai Phong
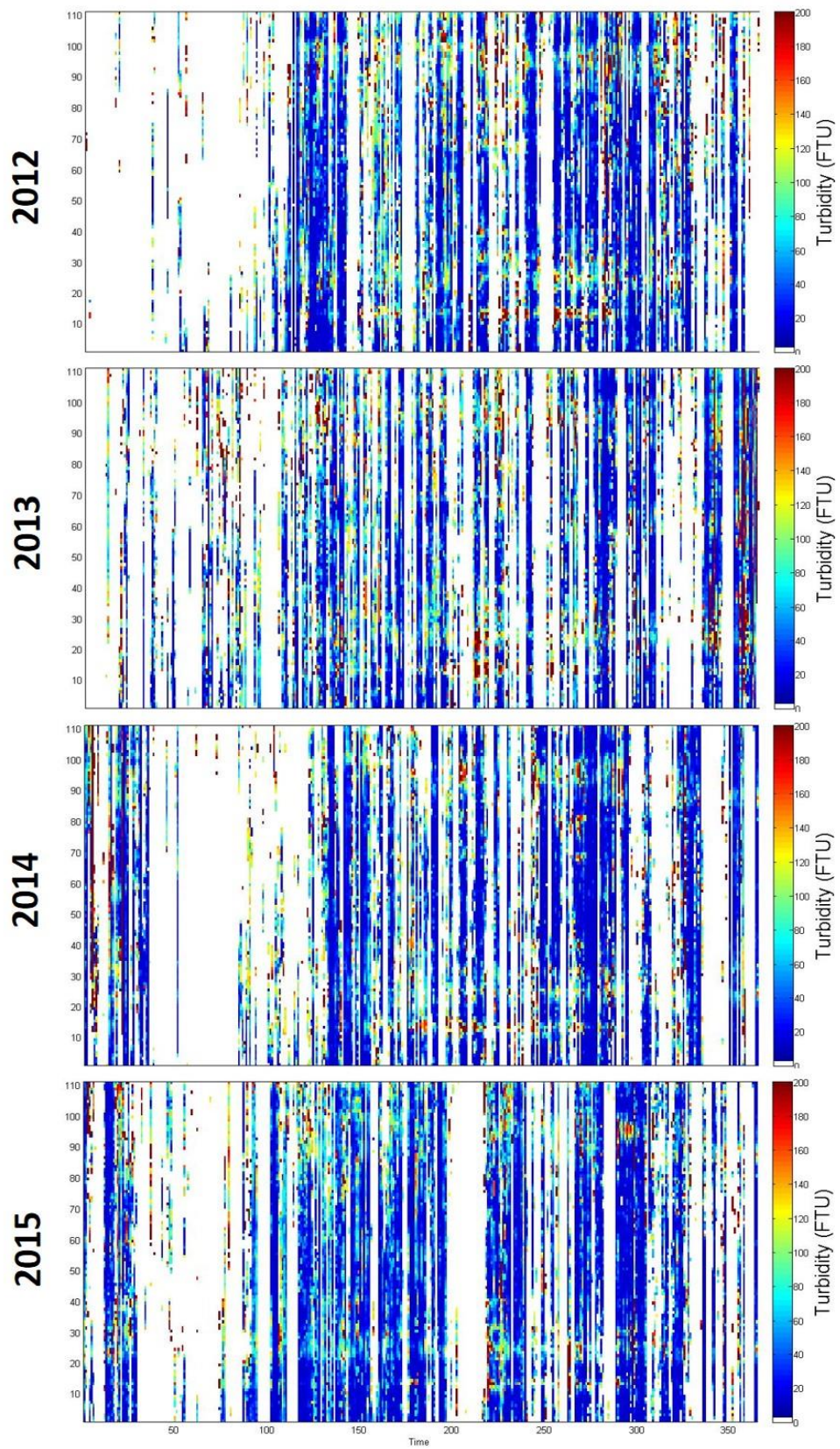
Figure 5.3 (d) Daily alongshore turbidity from south of Ma River to Hai Phong

5.3   Application of the Observed Data

This section aims to investigate the potential applicability of the obtained data for monitoring and understanding the behavior of suspended fine sediments discharged from multiple rivers. The northeast coast of Vietnam was selected as a case study site. The same technique will be applied to the Enshu-nada coast, which will be discussed in Chapter 6.

5.3.1   Long-term trend of observed turbidity
(1)   Long-term trend along the entire coastline

This section focuses on the long-term trend of the turbidity through observation of the averaged turbidity over the year.

Figure 5.4 shows the yearly average turbidity from south of the mouth of the Ma River to the middle of Hai Phong Bay (where the Cam River enters into the ocean). It
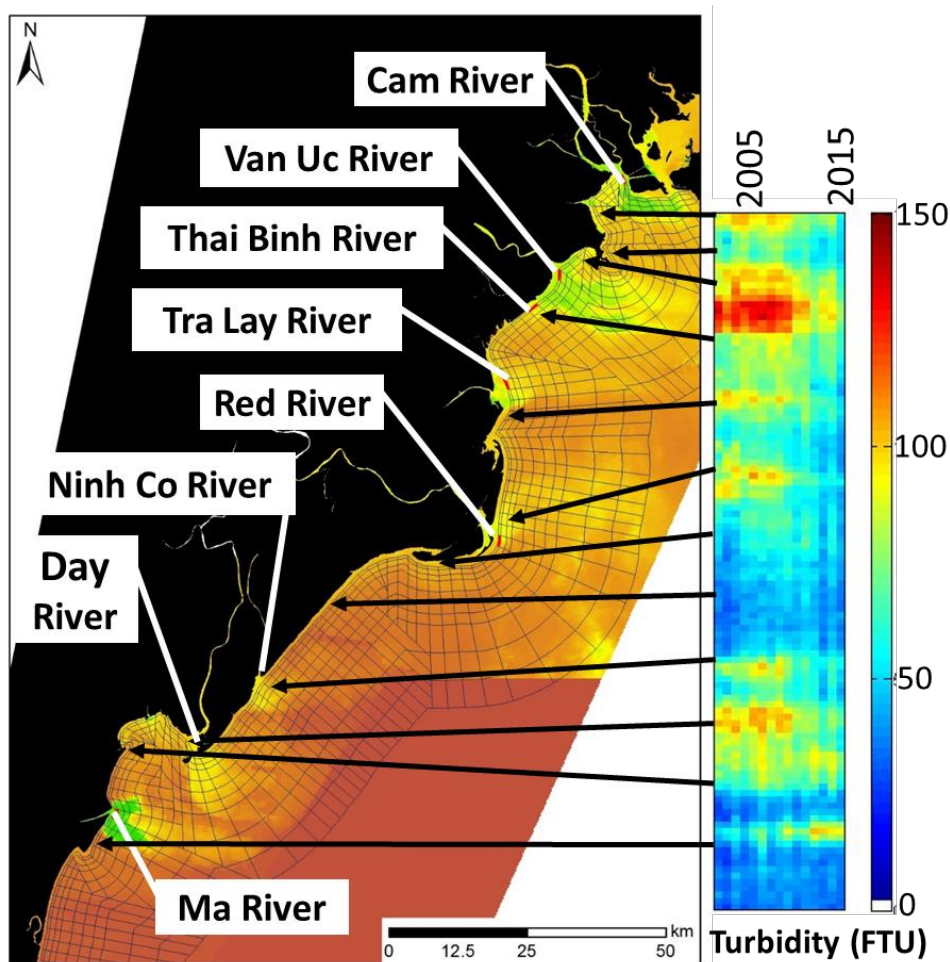
Figure 5.4 Yearly average turbidity along the coast from 2000 to 2015

58

clearly shows the high turbidity discharge near the river mouths, and a different magnitude highlights the different levels of river discharge over the time and alongshore. The mouth of the Van Uc River is the most influential part of the Red River system and releases higher turbidity compared with the other rivers, but its turbidity has reduced in recent years especially after 2008. It can be seen near the river mouths how much distance the turbid water travels along the coast.
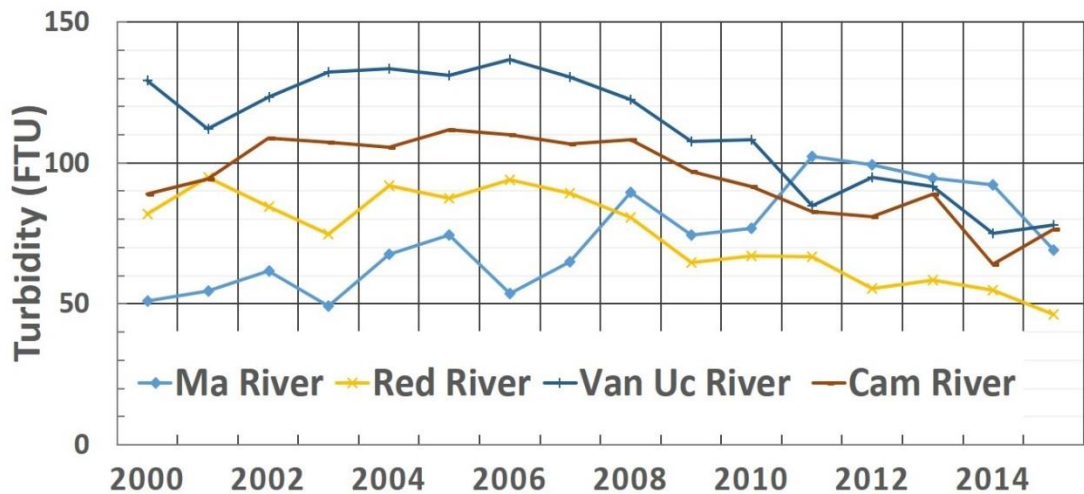
Figure 5.5 Yearly average turbidity of selected rivers from 2000 to 2015
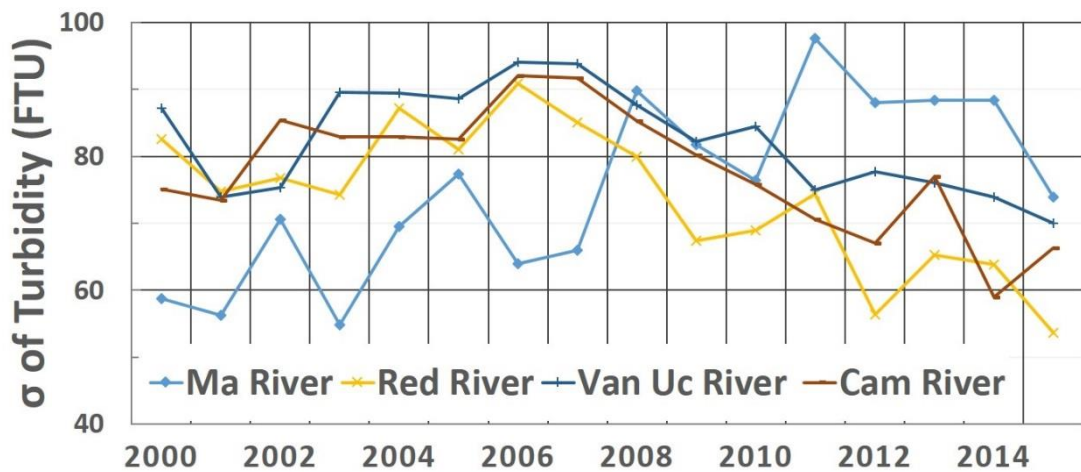
5.6 Standard deviation of yearly averaged turbidity of selected rivers

Figure 5.5 shows the time series of the estimated turbidity at selected cells located at the mouths of several rivers. The location of each cell corresponds to those shown in Figure 5.4. Figure 5.5 clearly shows the difference of the relative magnitude of the turbidity change at different river mouths. As seen in Figure 5.5, the Ma River

discharge tends to increase with the time while all the other rivers, the Red River, the Van Uc River, and the Cam River, show a clear decreasing trend in the turbidity. It should also be noted that a clearly lower turbidity was observed at the mouth of the Red River and this feature is consistent with the severe erosion observed around the river mouth.

Figure 5.6 illustrates the time series of the standard deviation of the observed turbidity in the same cells as Figure 5.5. It is interesting to observe that the standard deviations of the turbidity at each river mouth show a similar trend to that of the yearly averaged turbidity, i.e., the standard deviation tends to increase with each year at the mouth of the Ma River whereas the standard deviations of the other rivers tend to decrease especially after 2008. The Ma River tended to get higher peaks in 2011, and these specific turbidity fluctuations rather depend on the cloud-free image coverage within the calculated period.

Figure 5.7 shows the observed river discharge data at two river gauging stations upstream on the Ma River and the Chu River. The trend of the observed data and MODIS-based turbidity trend (Figure 5.5) closely correspond with each other. That is a good representation of the actual turbidity variation by the remote sensing approach where it could be utilized in places with no data available.
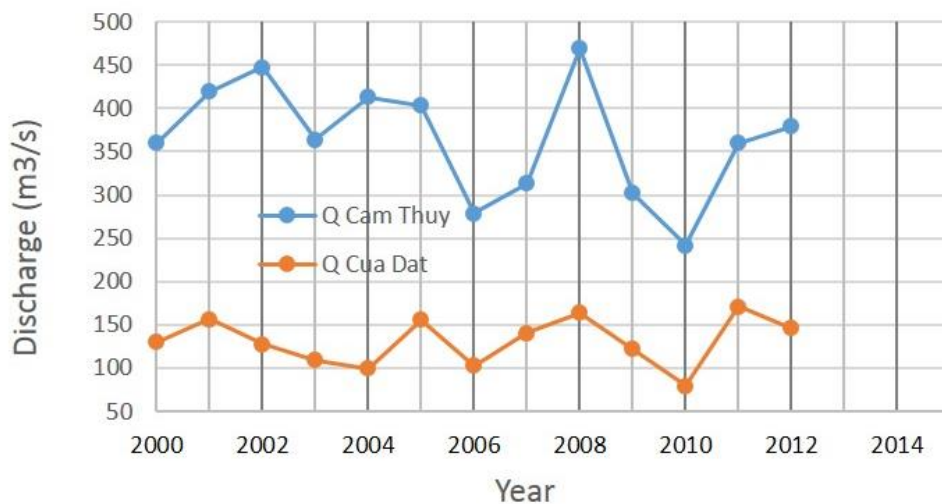
Figure 5.7 Yearly average river discharge (observed data at Cam Thuy station - upstream on the Ma River, and Cua Dat station - upstream on the Chu River)

60

Figure 5.8 shows the monthly average turbidity along the coast from 2000 to 2015. This figure clearly shows the turbidity variation within a year and the trend of all the years. The y-axis of the figure represents the alongshore direction from the south to the north (the first row of the cell system).
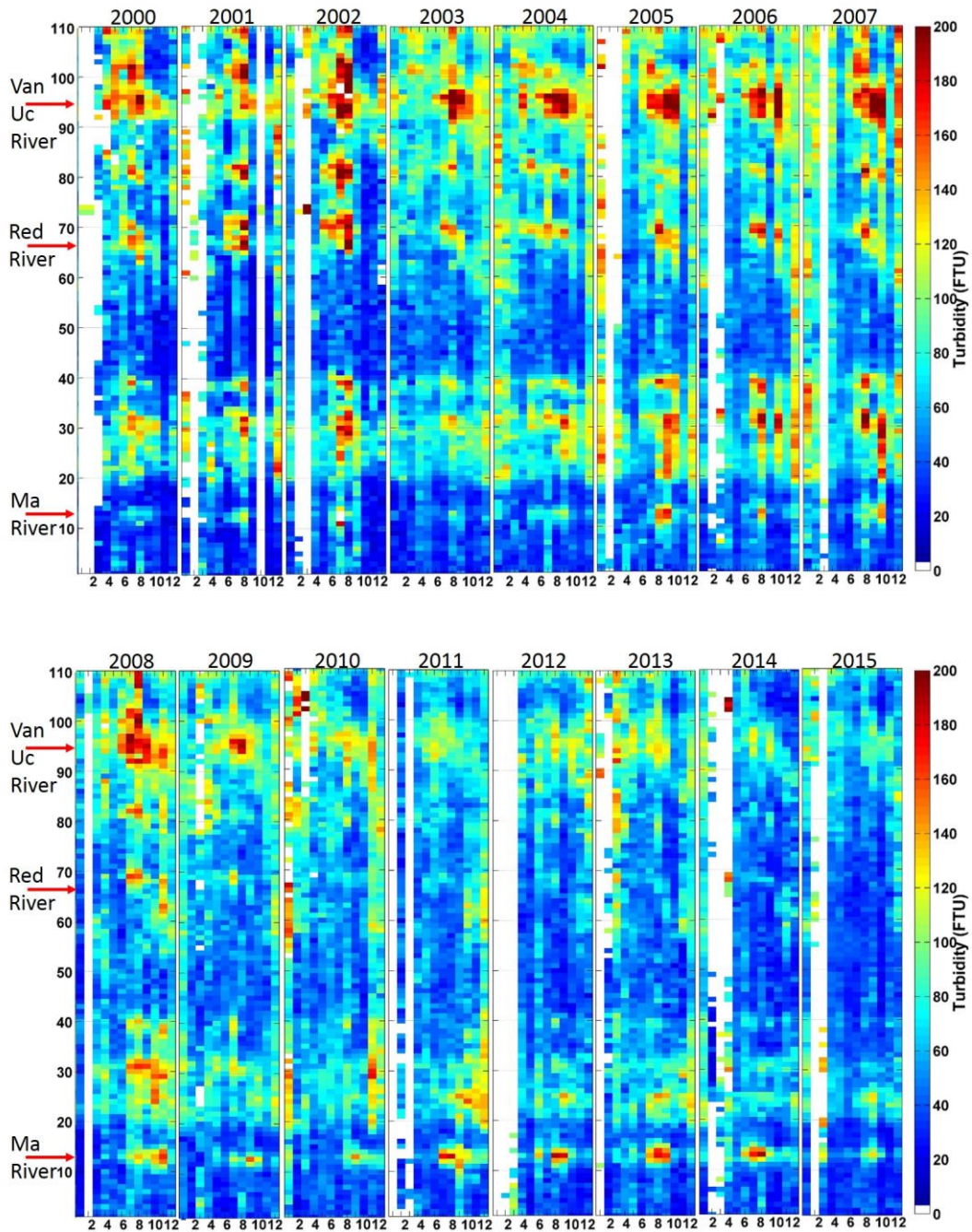
Figure 5.8 Monthly average turbidity along the coast from 2000 to 2015
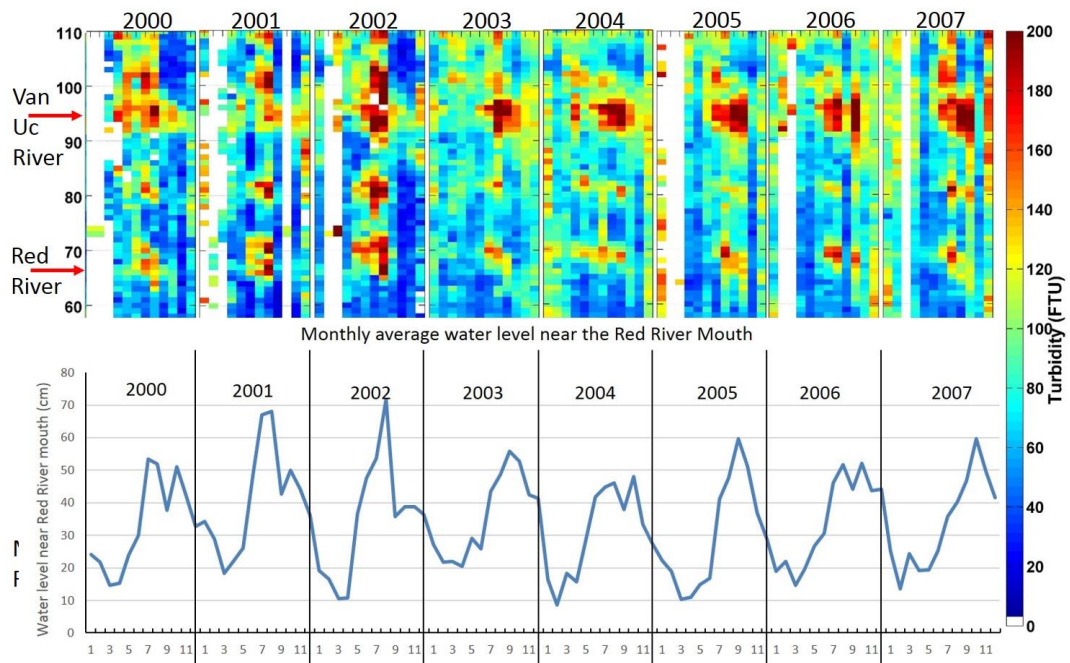
Figure 5.9 The selected cells for the comparison of long-tern turbidity trend

The monthly average water levels from 2000 to 2007 were obtained in the mouth of the Red River and Figure 5.8 illustrates those with the monthly average turbidity from the MODIS data. The monthly peaks of the variation clearly match with the observed water level and somehow the magnitude of the average monthly water level shows a direct relationship with the magnitude of the turbidity as well.

(2)   Turbidity around Hai Phong Bay
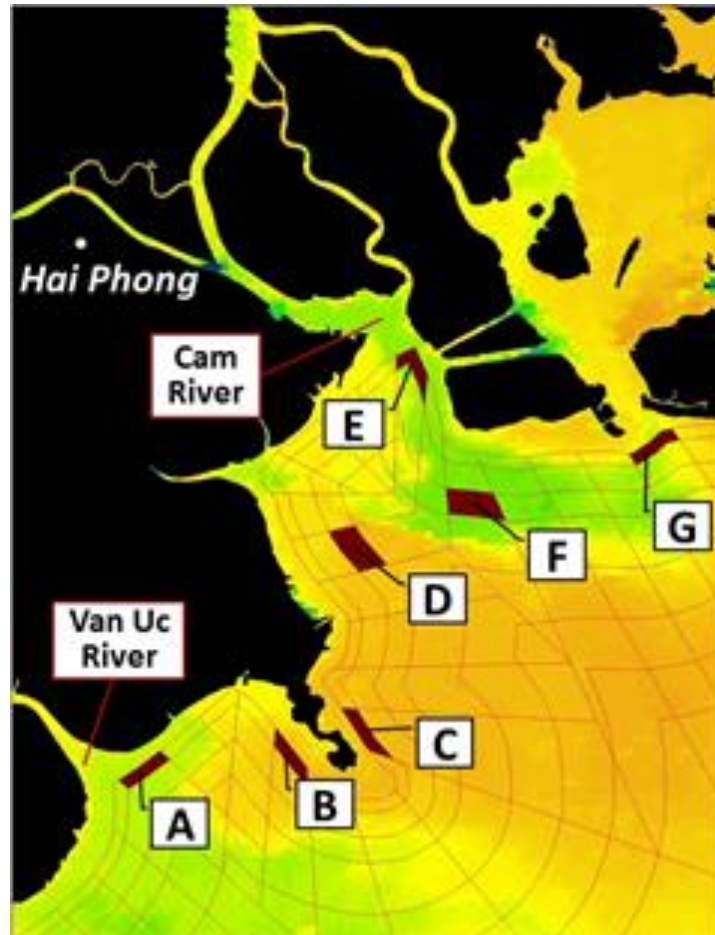
Figure 5.10 The selected cells for the comparison of long-term turbidity

In contrast to section (1) above, where turbidity only along the coast was compared, this part investigates how the turbidity changes in and around the bay which suffers serious turbidity and deposition problems. Hai Phong Bay is one of the most significant sites regarding higher turbidity patterns. Several cells have been selected for comparison around Hai Phong Bay and the mouth of the Van Uc River. Figure 5.10 shows the selected cells for the comparison.

Figure 5.11 (a) shows the time-history of the spatial and temporal average of the turbidity in the selected cells and each year. Figure 5.8 (b) also shows the time series in each cell and year, but the values are based on the standard deviations of the turbidity.

As seen in the figure, cells A and B show the highest average turbidity among other locations until 2009, and this feature indicates the dominant influence of the Van Uc River. The turbidity at cell E, around the mouth of the Cam River, was

relatively lower than those in A and B but the turbidities at these cells are nearly equal to each other after 2009. Low and stable turbidity at cell G indicates that high turbidity around Hai Phong Bay has little influence on Ha Long Bay. It is interesting to note that relatively high standard deviations are observed at cells C and D which are away from the river mouth, and the turbidity level may also be affected by some other external factors.
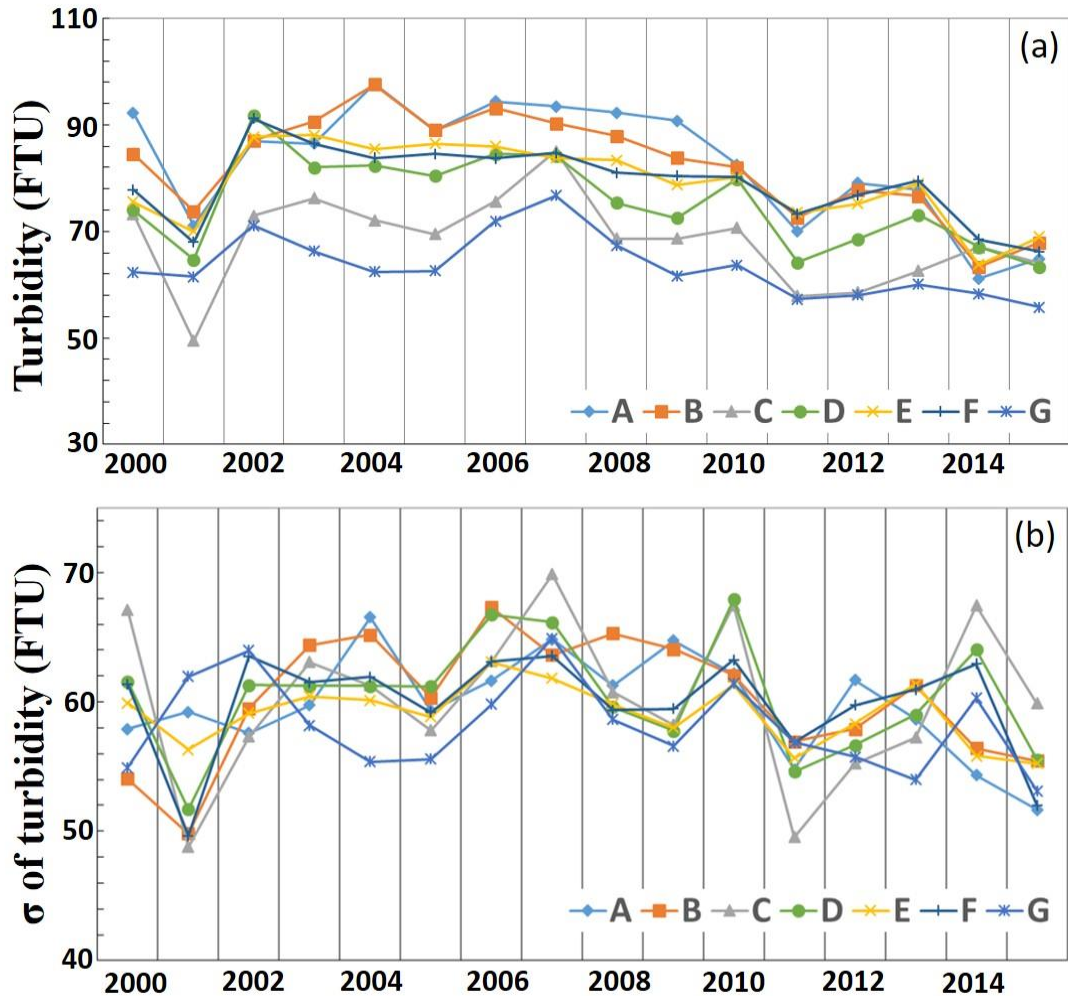
Figure 5.11 Time series of the turbidity characteristics in each selected cells indicated in Fig.5 ((a) yearly average and (b) standard deviation)

The overall decreasing trend of the turbidity was observed in Figure 5.11 (a) especially after 2006. Along the Red River system, two dams, the Thac Ba and Hoa Binh dams were constructed from 1989 to 2006 and three other dams, the Tuyen Quang, Son La and Lai Chau dams were constructed from 2007 to 2014. Figure 5.12 shows the decreasing trend of the total volume of sediment fluxes at different

locations (National Research project (code KC08.34/11-15), (2015)). The dominant decrease of sediment discharge is observed at the mouth of the Van Uc River, and this feature is consistent with the observed decreasing trend of turbidity from the MODIS data.
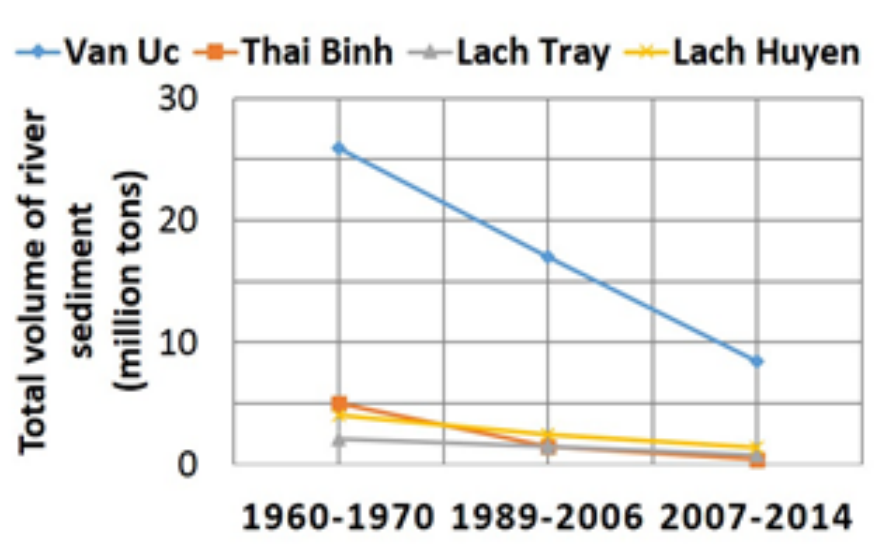
Figure 5.12 Total volume of river sediment discharge over the three time periods

Figure 5.13 shows the spatial distribution of the normalized average (top) and standard deviations (bottom) of the estimated turbidity from 2000 to 2005 (left) and from 2006 to 2015 (right), respectively. A significant decrease of the turbidity is also observed around the mouth of the Van Uc River. Standard deviations of the turbidity tend to be larger in the offshore cells. Relatively high turbidity is spread on both sides of the mouth of the Van Uc River while slightly higher turbidity is observed on the southern side of the river mouth. It is also interesting to note that, along the east side of Don Son resort (on the peninsula), the patterns of turbidity both in the average and standard deviations appear to be more affected by the turbidity on the west side of the peninsula. This feature indicates that the influence of turbid water from the Van Uc River reaches around the peninsula.
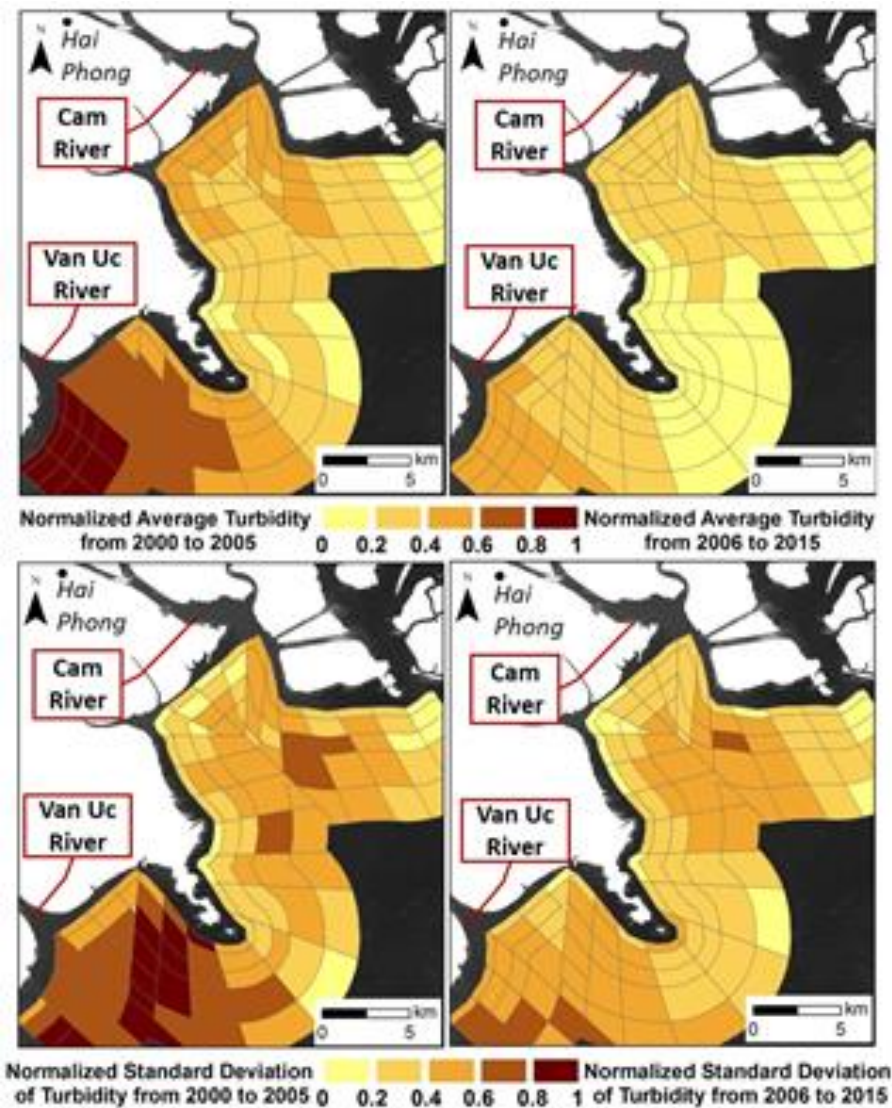
Figure 5.13 Spatial distribution of normalized average turbidity from 2000 to 2005 and from 2006 to 2015 (top); standard deviation of turbidity in those periods (bottom)

To evaluate the seasonal patterns of turbidity, two months were selected in the dry (April) and rainy (July) seasons and spatial distributions of the normalized average turbidity in each month were compared in Figure 5.14. As seen in the figure, the rainy season shows a clearly higher average turbidity around the river mouth while relatively high turbidity is widely expanded in the dry season. Further analysis is needed to understand the behavior of the turbidity affected by various external factors.
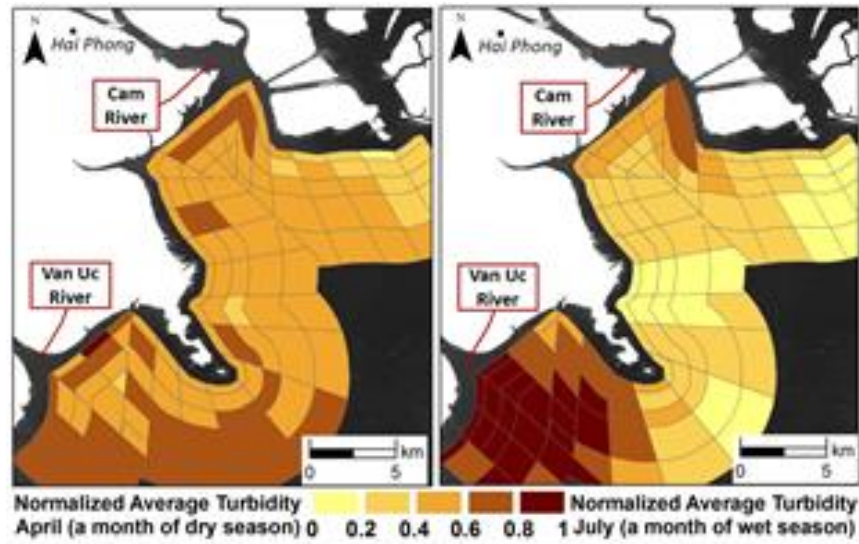
Figure 5.14 Spatial distribution of normalized average turbidity in dry (left) and wet (right) seasons

(3)   Detail investigations around the Ma River

This section further investigates the long term trend, especially focusing on the coast around the Ma River which suffers from an erosion problem. Figure 5.12 (a) shows a map of the Ma River site including two tributaries of the Red River system (RRS). There are several cells highlighted for the discussion, namely A to I.

A and B: The south side of the Ma River

C: The mouth of the Ma River

D: The north side of the Ma River

E: A mouth of a Ma River tributary

F: Right side of the Day River

G: The Day River (RRS)

H: The Ninh Co River (RRS)

I: The south side of the Red River

Figure 5.15 (b) shows the yearly average of turbidity around the Ma River. The Ma River has greater turbidity around the river mouth especially after 2007. Before 2007, on the other hand, the observed turbidity was relatively low even during the rainy season. According to Higashi (2015), drastic shoreline deterioration was
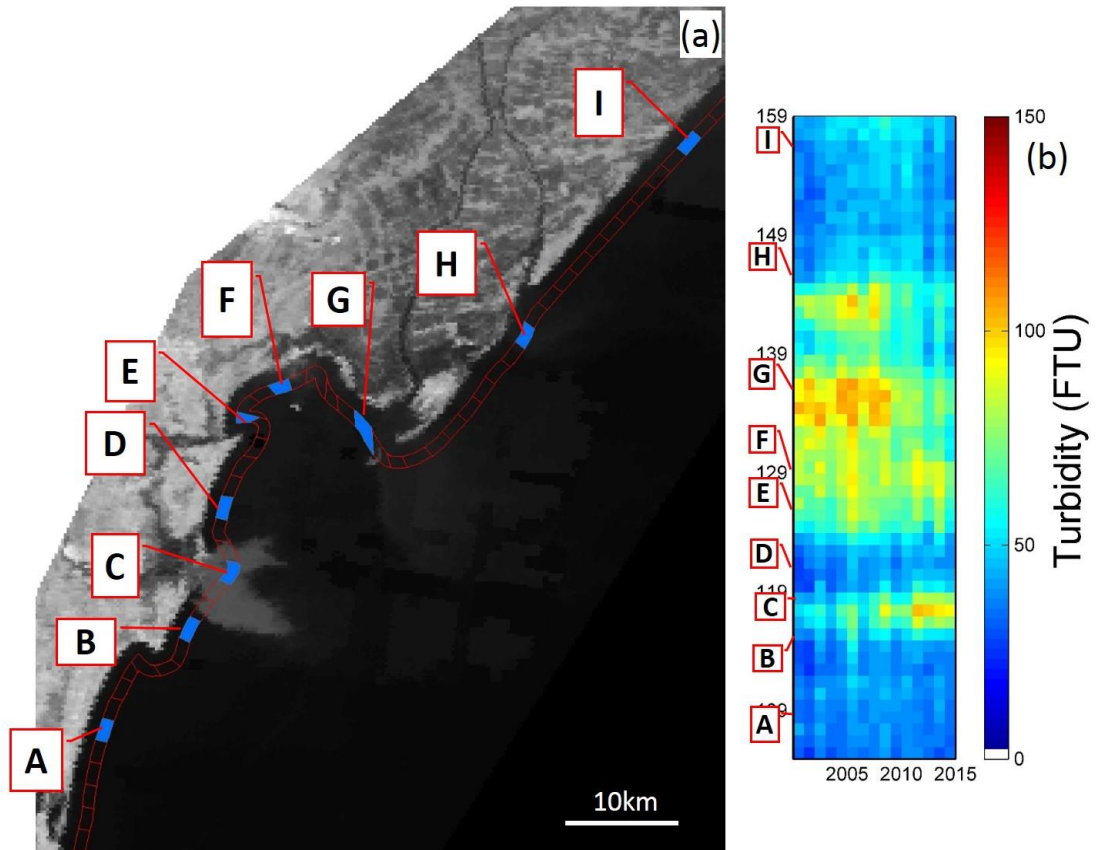
Figure 5.15 A detailed map of the Ma River and yearly average turbidity

observed from 2000 to 2007 and the shoreline became stabilized after 2007. This feature somehow corresponds to the observed turbidity at the mouth of the Ma River.

The average monthly turbidity from the south coast of the Ma River (location A, Figure 5.1) to the south coast of the Red River (location I, Figure 5.15) in the period of 2000 to 2015 is presented in Figure 5.16. Location C represents the mouth of the Ma River, and it clearly shows the increasing trend of turbidity over the past years. The discharge of the Ninh Co River (location H) shows a clearly decreasing trend and it is almost insignificant in recent times. There is no considerable turbidity level in the north part of the Ninh Co River; this indirectly implies that there is no considerable turbidity discharge from the Red River contributing to the southern part of the Red River Delta.

Turbid plumes near the mouth of the Ma River always show a very narrow extent, and this could relate to the observed thermo-luminescence (TL) variation that sediment tends to be transported more slowly on the south side of the Ma River.
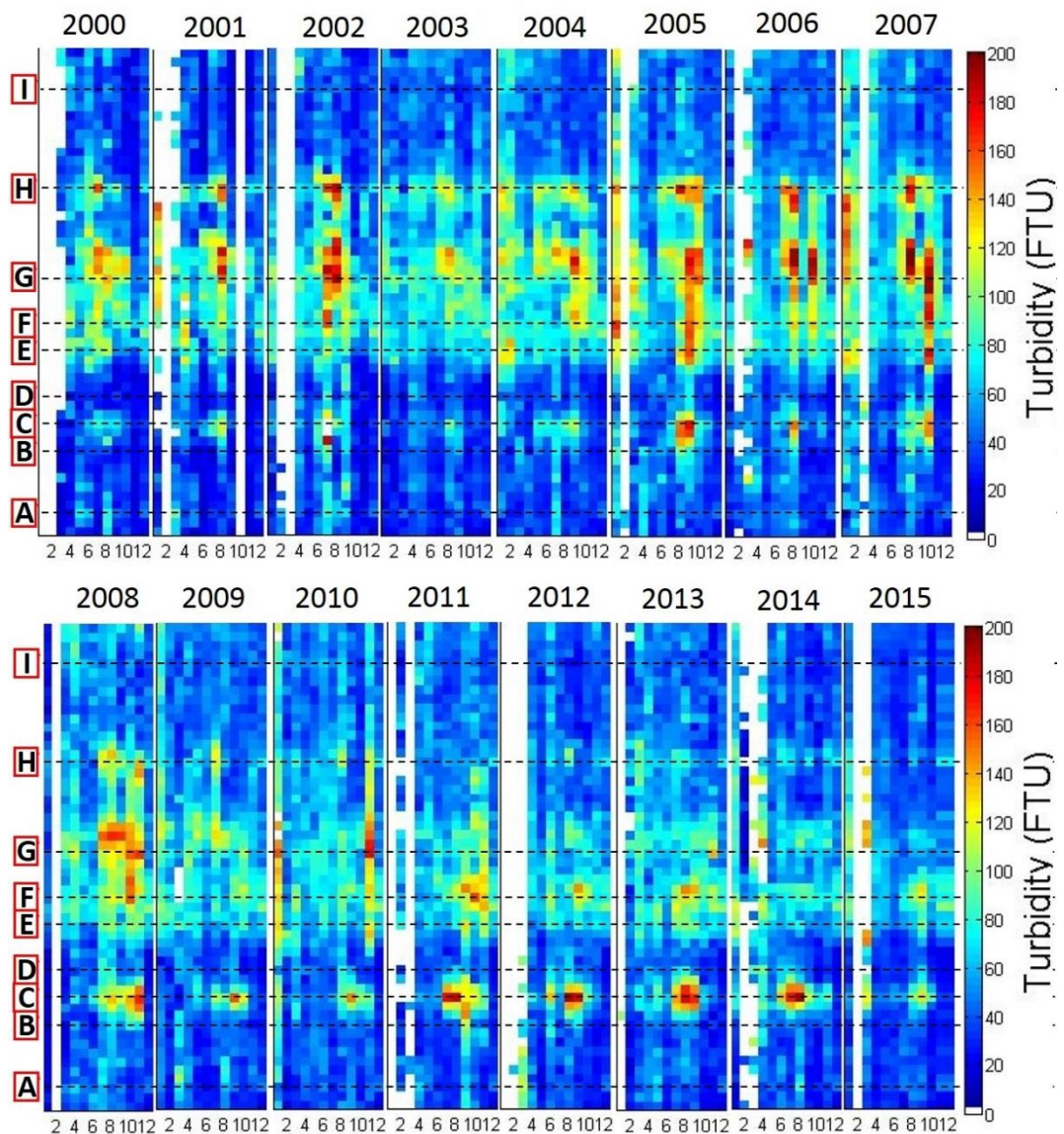
Figure 5.16 Monthly averaged turbidity around the Ma River from 2000 to 2015

Section 3.4 of chapter 3 contains a detailed discussion of the TL variations around the Ma River.

5.3.2 Area of high turbidity around the river mouth

(1) Time variations of the area

This section has been extended after looking at the trend of the monthly averaged turbidity. It is very essential to know the contribution of the turbid discharge on both sides of a river mouth. All the rivers in the study area have been divided into two sections at each river's mouth. Figure 5.17 and Figure 5.18 show the schematic

diagrams of the sections of a river and the symbols that have been used in the Figures 5.19 to Figure 5.21).
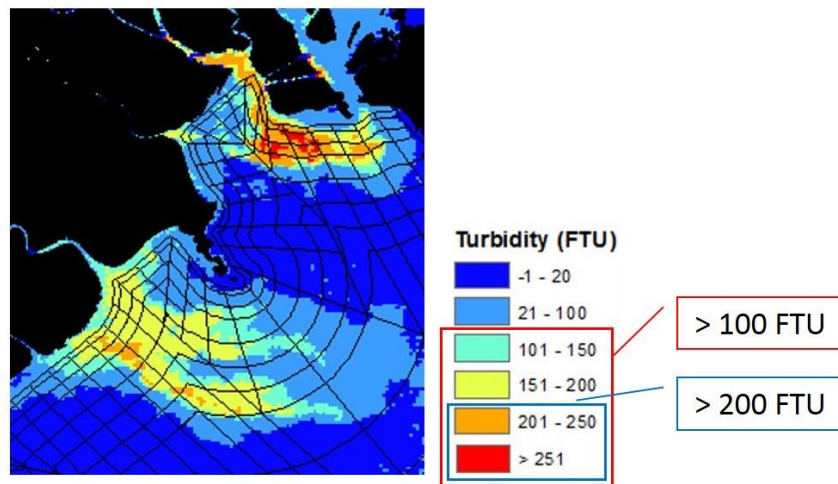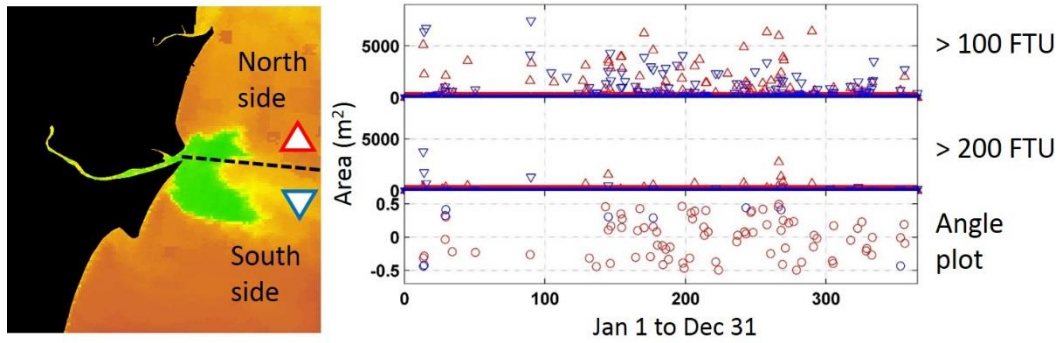
Figure 5.17 Schematic diagram of symbols that used in turbid area plot
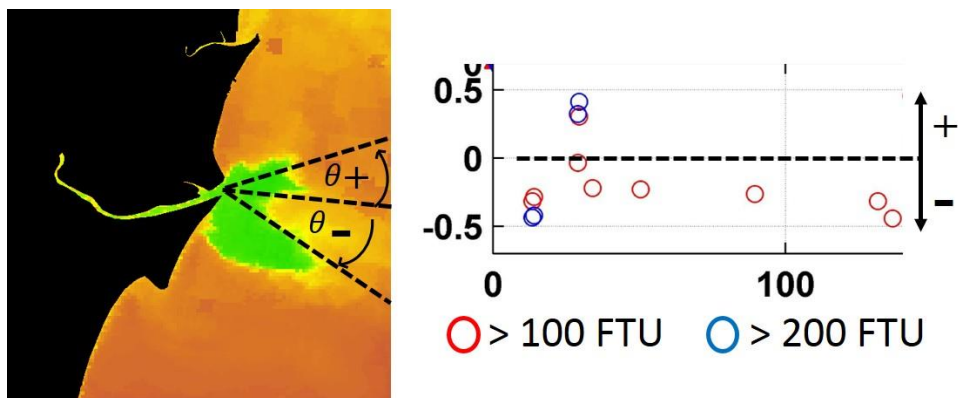
Figure 5.18 Schematic diagram of symbols that used in turbid plume direction plot

The pixel-based daily turbidity has been divided into two levels to represent the magnitude of the turbidity plume. Looking at the high discharge events, 100 FTU are considered to be divided into two levels. There are no references to the level of turbidity and its importance in the Vietnam study site. In the category of more than 100 FTU, 0 to 99 FTU pixels are eliminated; in the category of more than 200 FTU, 0 to 199 FTU pixels are eliminated.
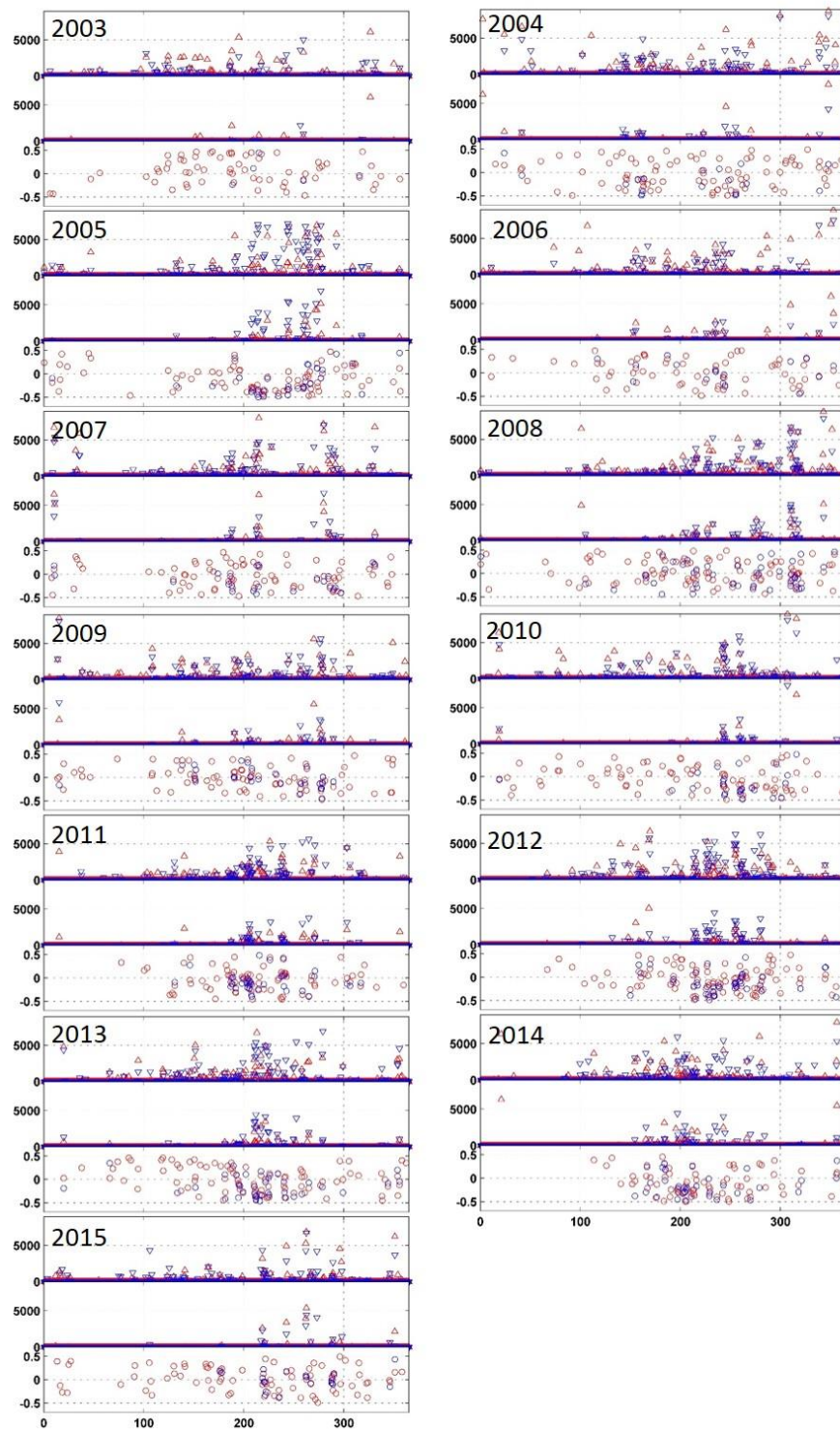
Figure 5.19 Area and direction of different turbidity levels around the Ma River (the x-axis in all the figures represents the Julian date of the year; the y-axis of the top and middle charts of each figure represents the area in square meters; the y-axis of the bottom chart of each figure represents the angle of the turbid plume (+ ve values: northwards from the river outlet direction; – ve values: southwards from the river outlet direction)

72
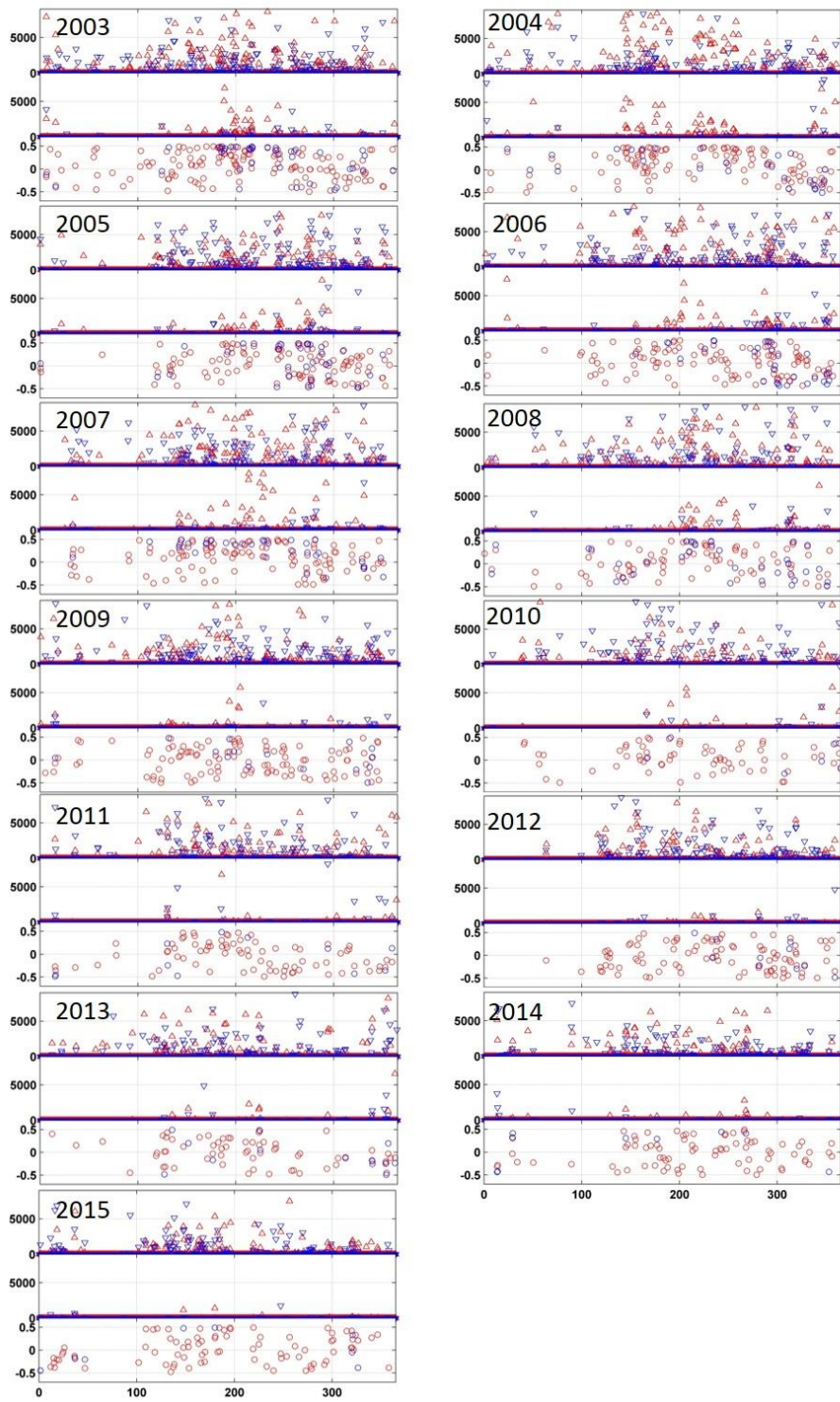
Figure 5.20 Area and direction of different turbidity levels around the Red River (the x-axis in all the figures represents the Julian date of the year; the y-axis of the top and middle charts of each figure represents the area in square meters; the y-axis of the bottom chart of each figure represents the angle of the turbid plume (+ ve values: northwards from the river outlet direction; – ve values: southwards from the river outlet direction)
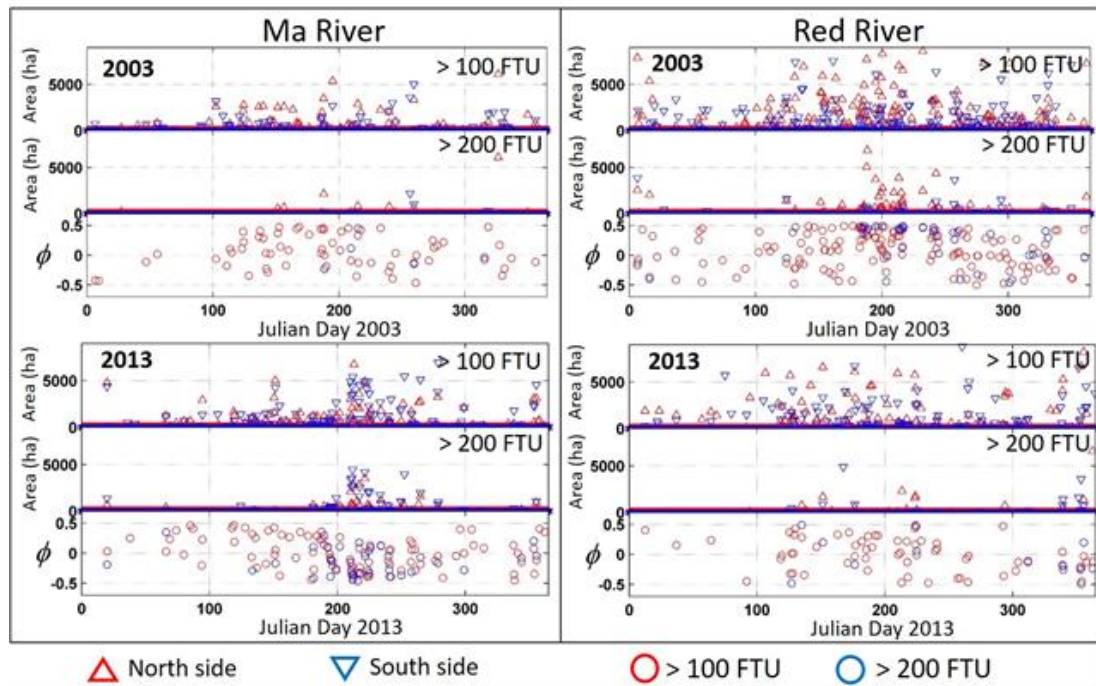
Figure 5.21 Comparison of the area and direction with respect to different turbidity levels around the Ma and Red Rivers (the x-axis in all the figures represents the Julian date of the year; the y-axis of the top and middle charts of each figure represents the area in square meters; the y-axis of the bottom chart of each figure represents the angle of the turbid plume (+ ve values: northwards from the river outlet direction; − ve values: southwards from the river outlet direction)

Figure 5.21 shows a comparative study that has been carried out around the mouths of the Ma and Red Rivers based on the daily turbidity maps. The top chart in each case represents the area of the plume with turbidity greater than 100 FTU while the middle charts shows the same area with turbidity greater than 200 FTU. In these figures, the estimated plume was split by the straight cross-shore line at the river mouth and the areas of the plume on the northern and southern sides of the line, A_N and A_S, were separately estimated. The bottom chart then compares the relative magnitude of A_N and A_S by an angle, $\phi=\arctan(A_N/A_S)/\pi$.

Based on these figures, several features can be observed. At the Red River, for example, both the area and the number of the plumes with high turbidity were larger in 2003 than those in 2013. The plume tends to symmetrically spread on both sides of the river mouth. Around the Ma River, on the other hand, the number of higher discharge events and degree of the turbidity plumes tended to increase in 2013. Interestingly, the turbid discharges of more than 200 FTU tend to be spread towards the south.

(2)   Tidal dynamics of the area
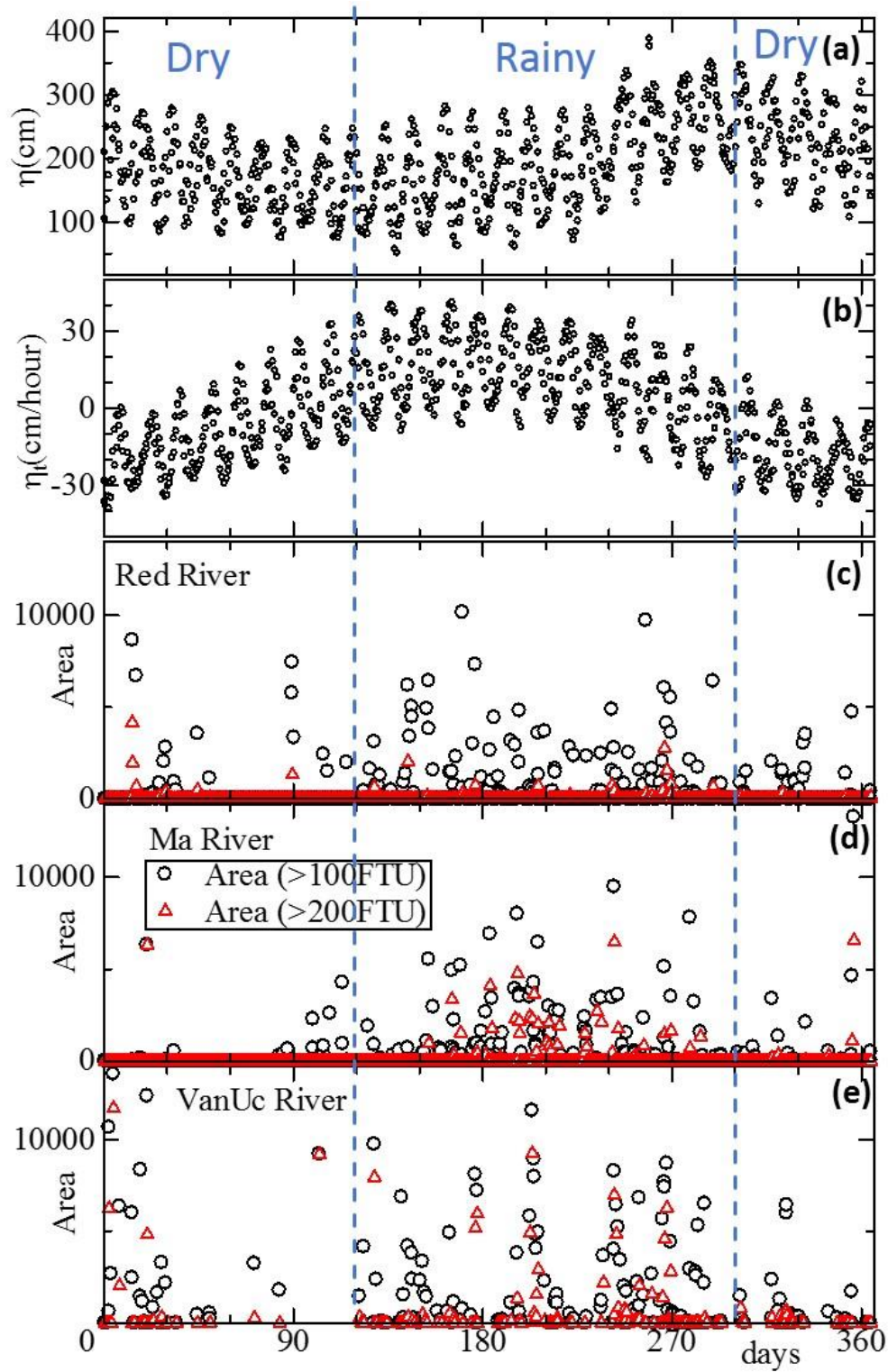
Figure 5.22 (a) Tide level at the MODIS acquisition time (η); (b) speed of elevating tide level at the MODIS acquisition time (η$_t$); (c) to (e) high turbidity areas around the mouths of Red, Ma, and Van Uc Rivers, respectively

Figure 5.22 (a) shows the tide level at the MODIS acquisition time (η) in 2014; (b) the speed of the elevating tide level at the MODIS acquisition time (η t); (c) to (e) the high turbidity areas around the mouths of the Red, Ma, and Van Uc Rivers, respectively. The tide level at the MODIS recording time distributed over the year and η and η$_t$ are reasonably well distributed in the wet and dry seasons. The Red and Van Uc Rivers show the same tendency while the Ma River shows a different tendency.
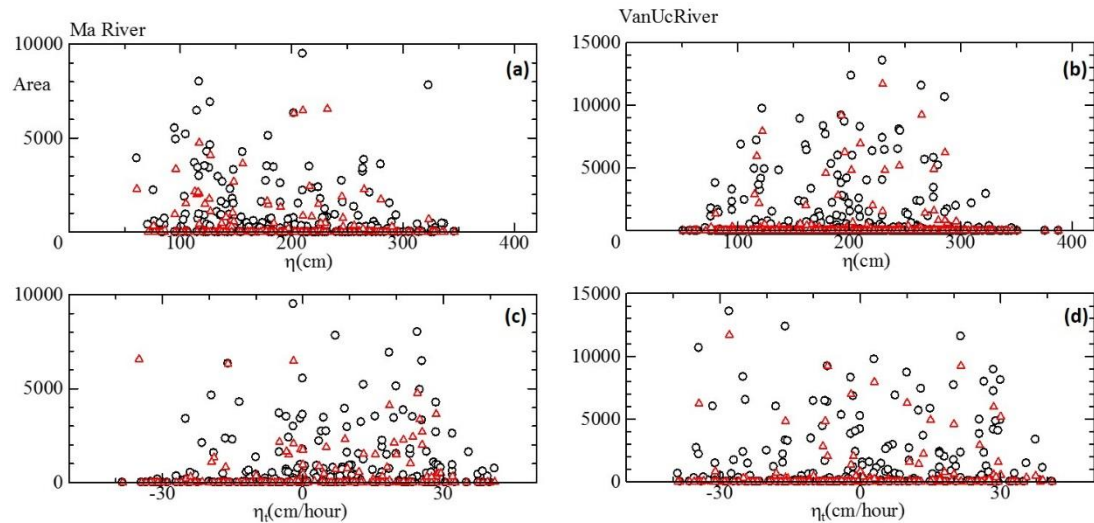
Figure 5.23 Correlation of tide level at MODIS acquisition time (η) and speed of elevating tide level at MODIS acquisition time (η t) on turbid plume area and level of turbidity between Ma and Van Uc Rivers

Figure 5.23 shows correlation of the tide level at the MODIS acquisition time (η) and speed of the elevating tide level at the MODIS acquisition time (η t) on the turbid plume area and level of turbidity between the Ma and Van Uc Rivers. The Ma River and Van Uc River show different trends of the turbid area distribution. In the Ma River, there is a relatively larger area during the flood tide and low tide (and a clearly smaller area during the high tide). Tidal currents have a smaller effect but the influence of waves on shallower water during the low tide may have a more dominant influence.

Figure 5.24 shows the correlation of the tide level at the MODIS acquisition time (η) and speed of the elevating tide level at the MODIS acquisition time (η t) on the turbid plume area and the level of turbidity between the Red and Van Uc Rivers. By comparing Figures 5.23 and 5.24, it is clear that the Red and Van Uc Rivers show

similar characteristics while the Ma River shows a different trend. There is a relatively larger area during the ebb tide and a smaller area during the high tide and low tide in both rivers in Figure 5.24. Tidal currents have a dominant influence on these two rivers since the amount of tidal exchange may be larger in these two big rivers.
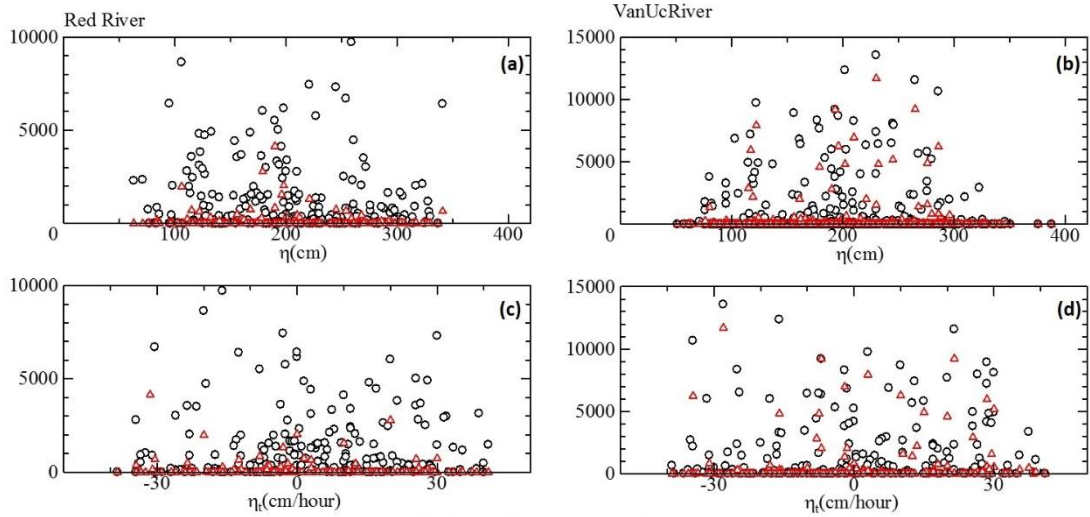
Figure 5.24 Correlation of tide level at MODIS acquisition time (η) and speed of elevating tide level at MODIS acquisition time (η_t) on turbid plume area and level of turbidity between Red and Van Uc rivers

Figure 5.25 shows the variation of the area of the turbid plume (the north side, south side and total) from 2000 to 2015 in the Red River. In the mouth of the Red River, the high turbidity area of the top 10% average shows a clear decreasing trend whereas the average of the all the obtained area is nearly constant over the past 15 years. The integral of the product of turbidity and the area shows a gradually decreasing trend in the top 10% average. The amount of effective data was less in 2000, 2001 and 2002 due the presence of just a single satellite.

Figure 5.26 Variation of the area of the turbid plume (the north side, south side and total) from 2000 to 2015 in the Ma River. The high turbidity area of the top 10% average shows high fluctuations and a slightly increasing trend. Moreover, the relative magnitudes of A_N and A_S switch in 2007 and the integral of the product of turbidity and area are nearly constant over the 15 years.
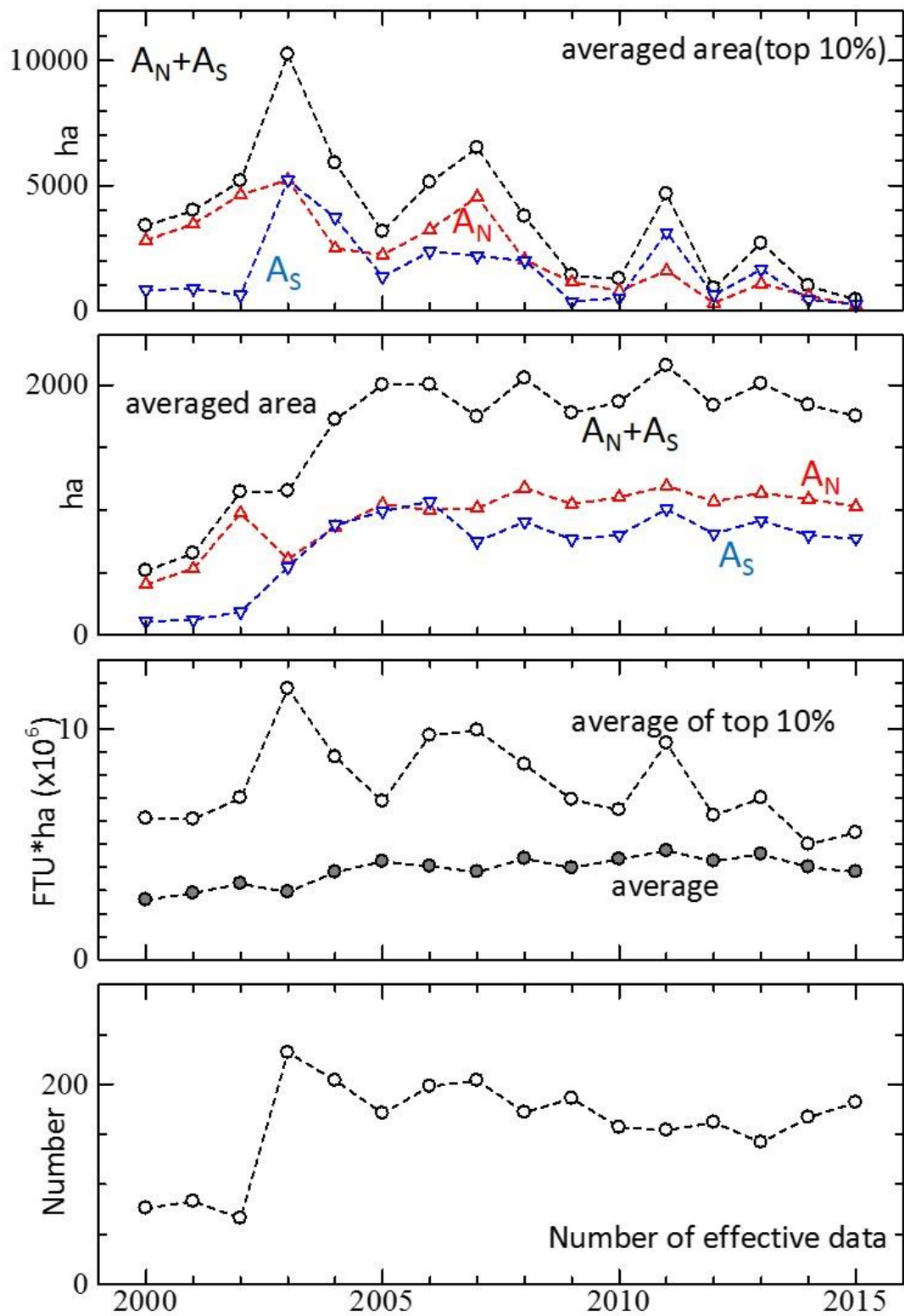
Figure 5.25 Variation of area of turbid plume (North side, South side and total) from 2000 to 2015 in the Red River
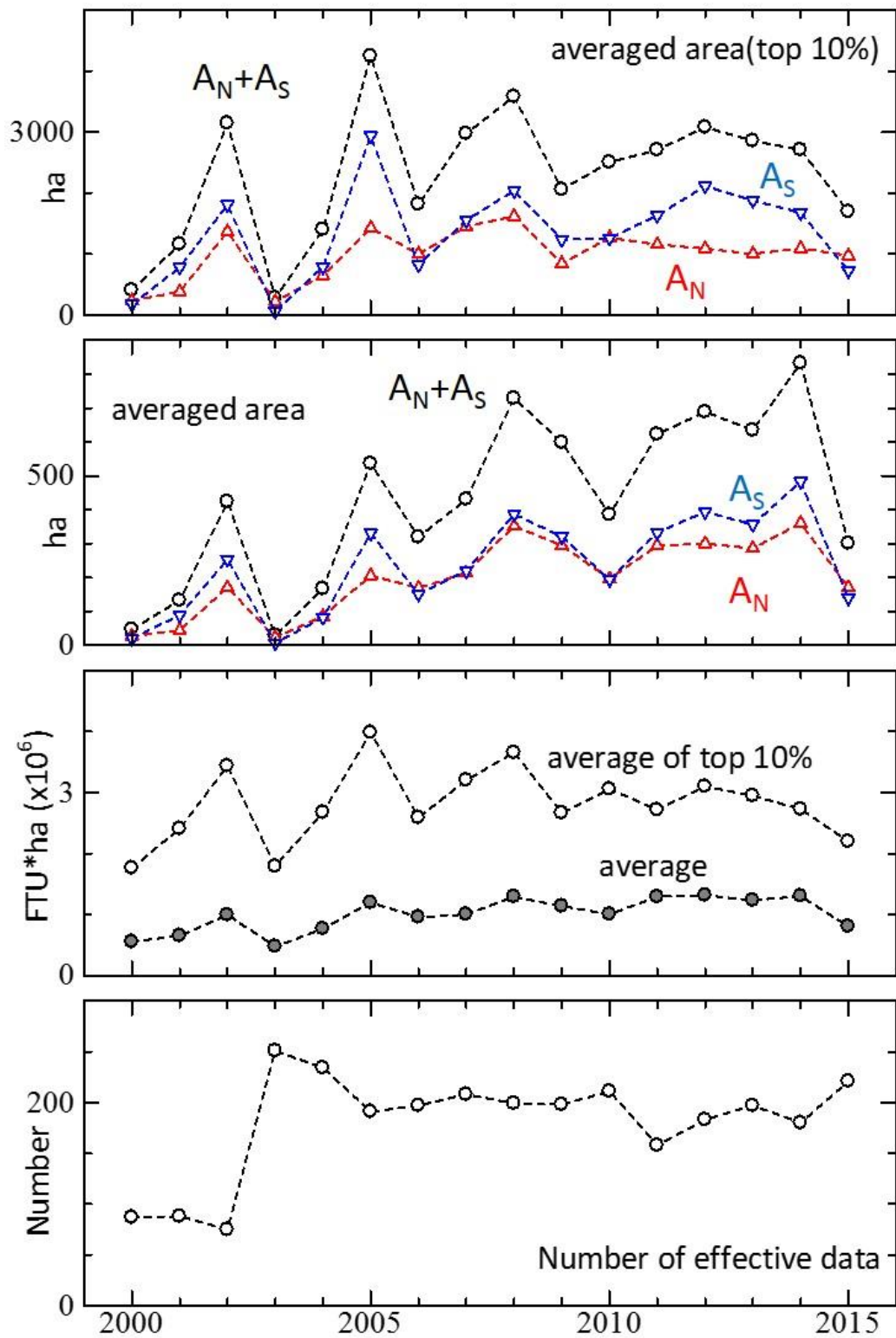
Figure 5.26 Variation of area of turbid plume (North side, South side and total) from 2000 to 2015 in the Ma River

CHAPTER SIX

FEASIBILITY AND APPLICABILITY OF THE PROPOSED MONITORING SYSTEM IN THE OTHER AREAS (ENSHU-NADA COAST)

6.1   Introduction

The MODIS red band surface reflectance shows a better prediction of turbidity in the Vietnam case study. As a proxy measurement of turbidity, the variation of the red band reflectance was thoroughly examined around the mouth of the Tenryu River and surrounding river mouths.

In recent times, the east side of the Tenryu River has experienced relatively higher erosion than the west side of the river. Some researchers have claimed that the west side is well protected by coastal structures while another group suggests different phenomena, the shape of the sand spit and the opening of the river mouth located on the east side which direct the river discharge eastward. This river flow momentum may affect the balance of the sediment supply on both sides of the river mouth. An attempt has been made to explain the above mechanism using the results of the monitoring system.

The monitoring system that has been developed in this study directly used the obtained raw data and process from 2000 to 2015. The study area coordinates and corresponding image tiles were changed prior to execution of the monitoring system. The results of the monitoring system together with the hydrodynamic conditions were thoroughly analyzed to understand the turbidity patterns around the mouth of the Tenryu River.

6.2   Geographical Setting of Study Area and the Cell System

Figure 6.1 (top) illustrates the study area, which covers the mouth of the Tenryu River and the Hamana inlet. The entire cell system was also overlaid on the study area map. In this site, the unique grid size is defined for the monitoring system (1000m x 500m) which approximately includes eight MODIS pixels per cell. Figure 6.1 (bottom) shows the cell number of selected cells which are those that have been used in the detailed

analysis. The dominant turbid discharge could be seen after the typhoon season on the Enshu-nada coast. Figure 6.2 shows the pre- and post-MODIS images of typhoon Phanfone.
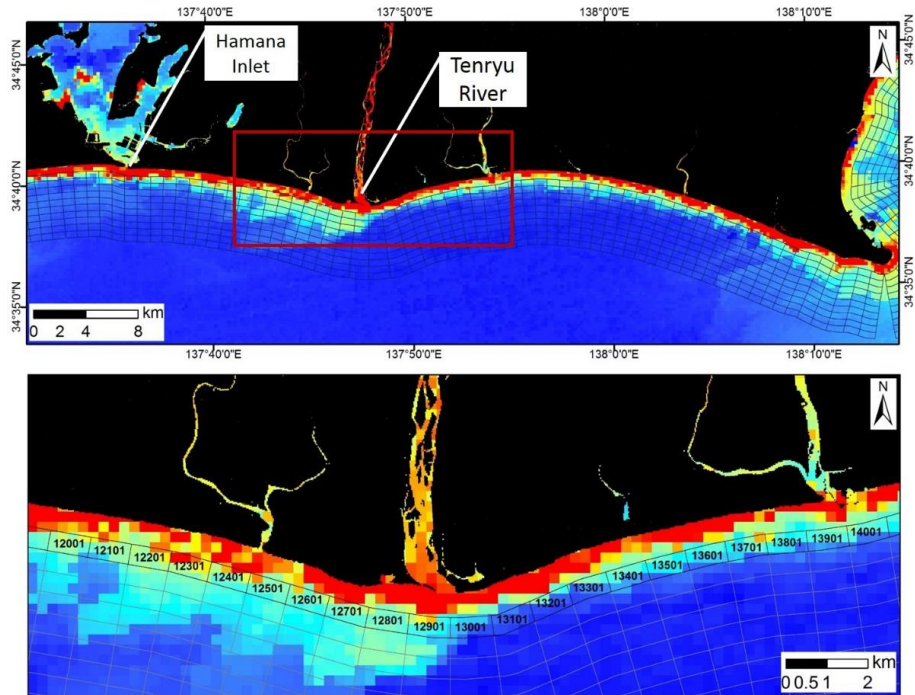
Figure 6.1 Map of study area of Ensu-nada coast and the cell system
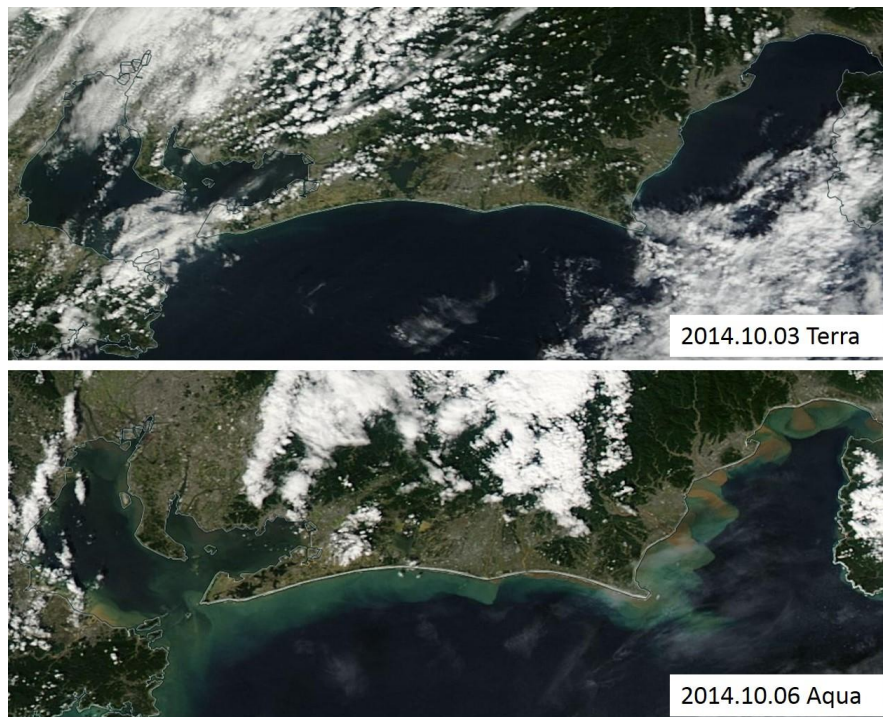
Figure 6.2 Pre and post MODIS images of Typhoon Phanfone

6.3   Cloud Masking

The similar approach that had been used in the Vietnam study site is used to mask out cloud in this study site as well. For the evaluation and definition of the threshold values for the algorithm, several sample images over 16 years' time period were used to extract the surface reflectance values of the red (band 1) and NIR (band 2) bands. Table 6.1 shows the classes used for the classification of pixels.

Table 6.1 Classes of classified pixels

CODE	Description
HT	High turbidity
MT	Medium turbidity
LT	Low turbidity
NT	No turbidity
DC	Dense cloud
MC	Medium cloud
LC	Thin cloud (haze) and boundary pixels of a cloud patch

Figure 6.3 shows some of the red band images with extracted points of interest (POI) for the threshold calculation. All the extracted surface reflectance values with the corresponding class and image coordinates are documented in Appendix III. The images were selected to include clear images without turbidity and clouds, cloudy images and mixed images. Both the Aqua and Terra satellite MODIS images were used for the threshold identification. This procedure is mainly conducted based on visual interpretation with the help of two online image viewers: the NASA MODIS world view (https://worldview.earthdata.nasa.gov) and Google Earth Engine MODIS data set (https://explorer.earthengine.google.com).

According to the previous algorithm, three threshold values are identified to extract qualified pixels for the river turbid discharge analysis. Procedures similar to Chapter 4 are followed to define the ratio index and plot against the red band reflectance. Figure 6.4 is used to identify the threshold values, in which the x-axis represents the normalized band 1 (red) surface reflectance of the Aqua and Terra satellites, the y-axis represents the ratio index developed based on Equation 1 in Chapter 4. The threshold
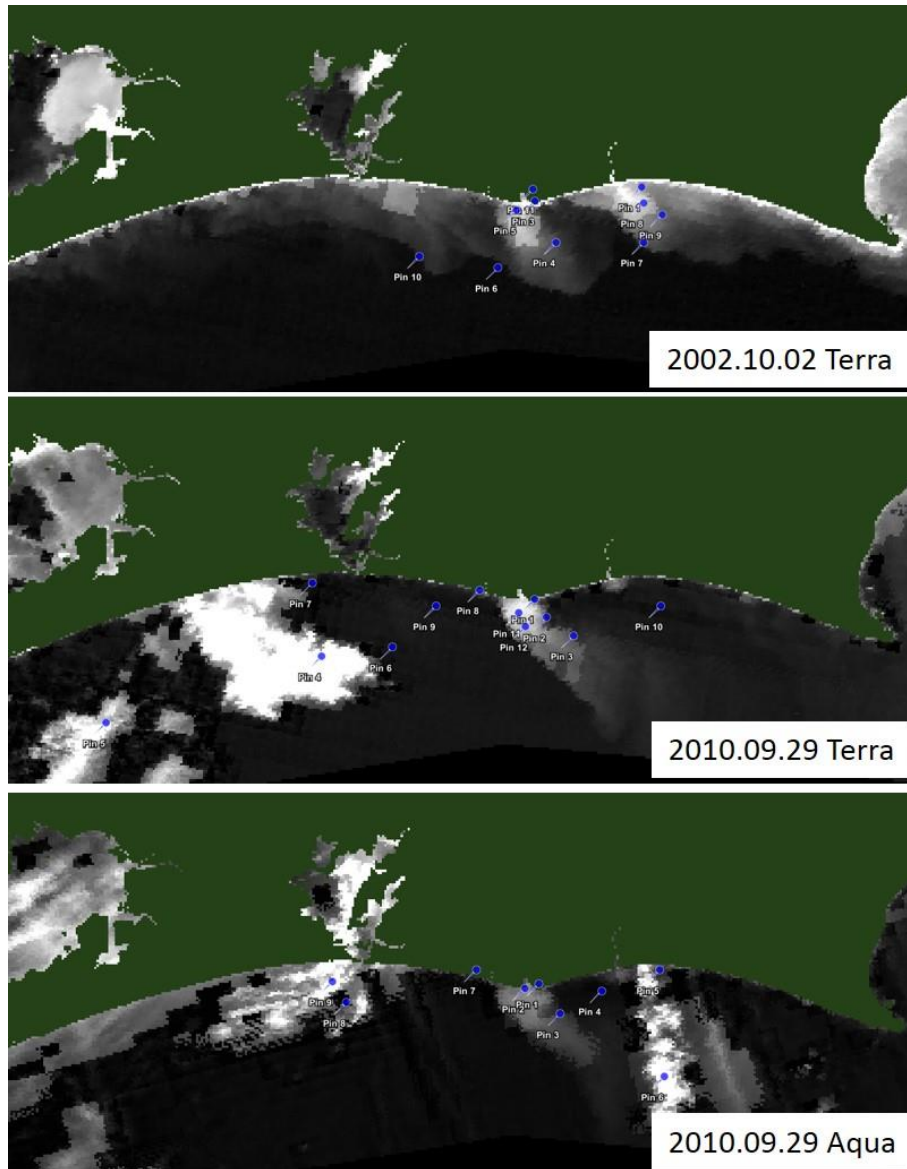
Figure 6.3 Selected red band data with POIs

1 value (B1 >= 0.2) was used to mask out dense cloud which is quite easy in this process. After that, the threshold value 2 (B1 <= 0.06) was used to assign a very low proxy value to represent low turbid water. The threshold value 3 (ratio <= 0.3 AND B1 >= 0.06) was used to mask out medium dense cloud patches.

As seen in Figure 6.4, values under threshold value 2 consist of the LC class pixels, but the contribution of those pixels in the final turbidity pattern is very low. Therefore, the analysis was confined by that limitation. Finally, the qualified pixels were used for the comparison of the 16 years' data set. Figure 6.5 shows the performance of cloud masking and extracting the qualified pixels for the analysis.
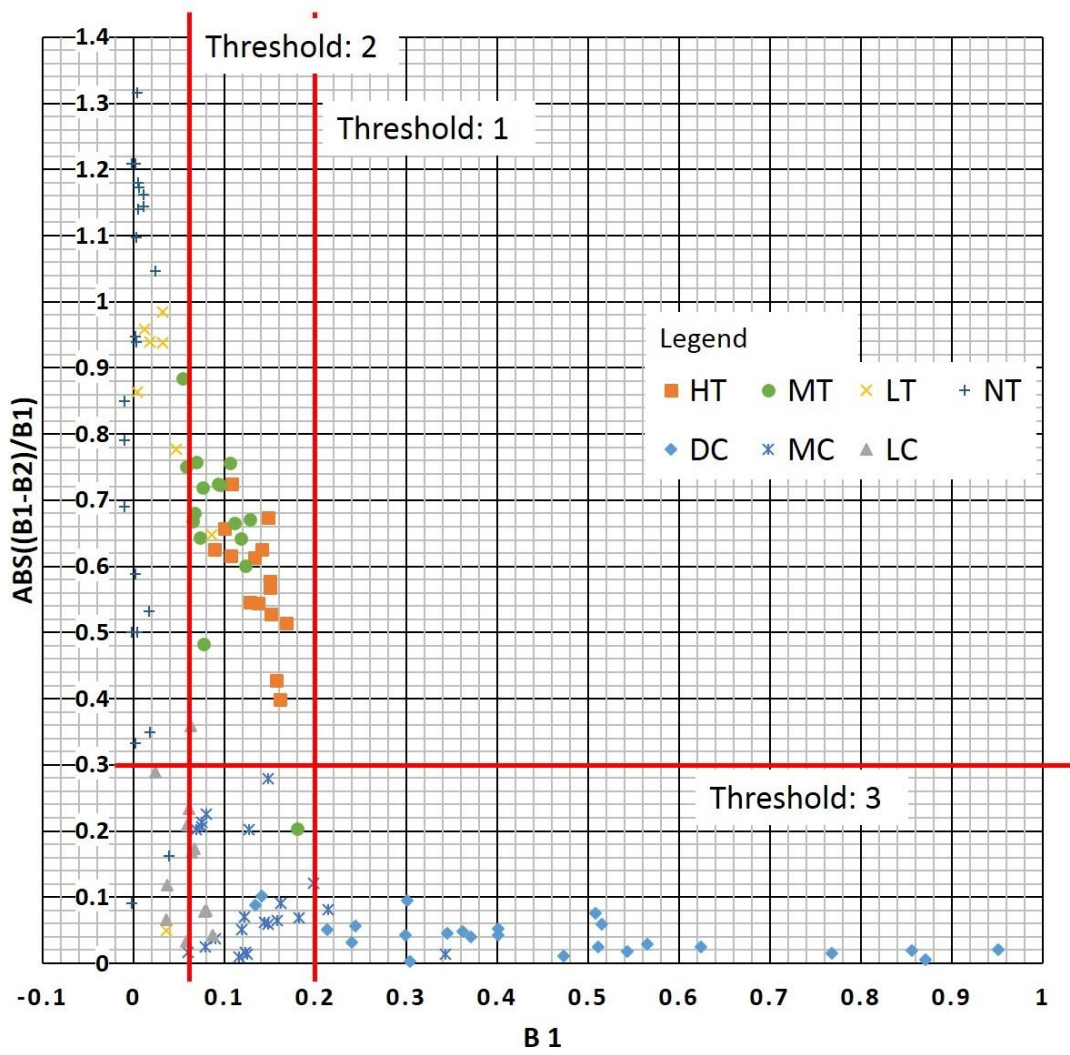
Figure 6.4 Threshold values for qualified pixels identification
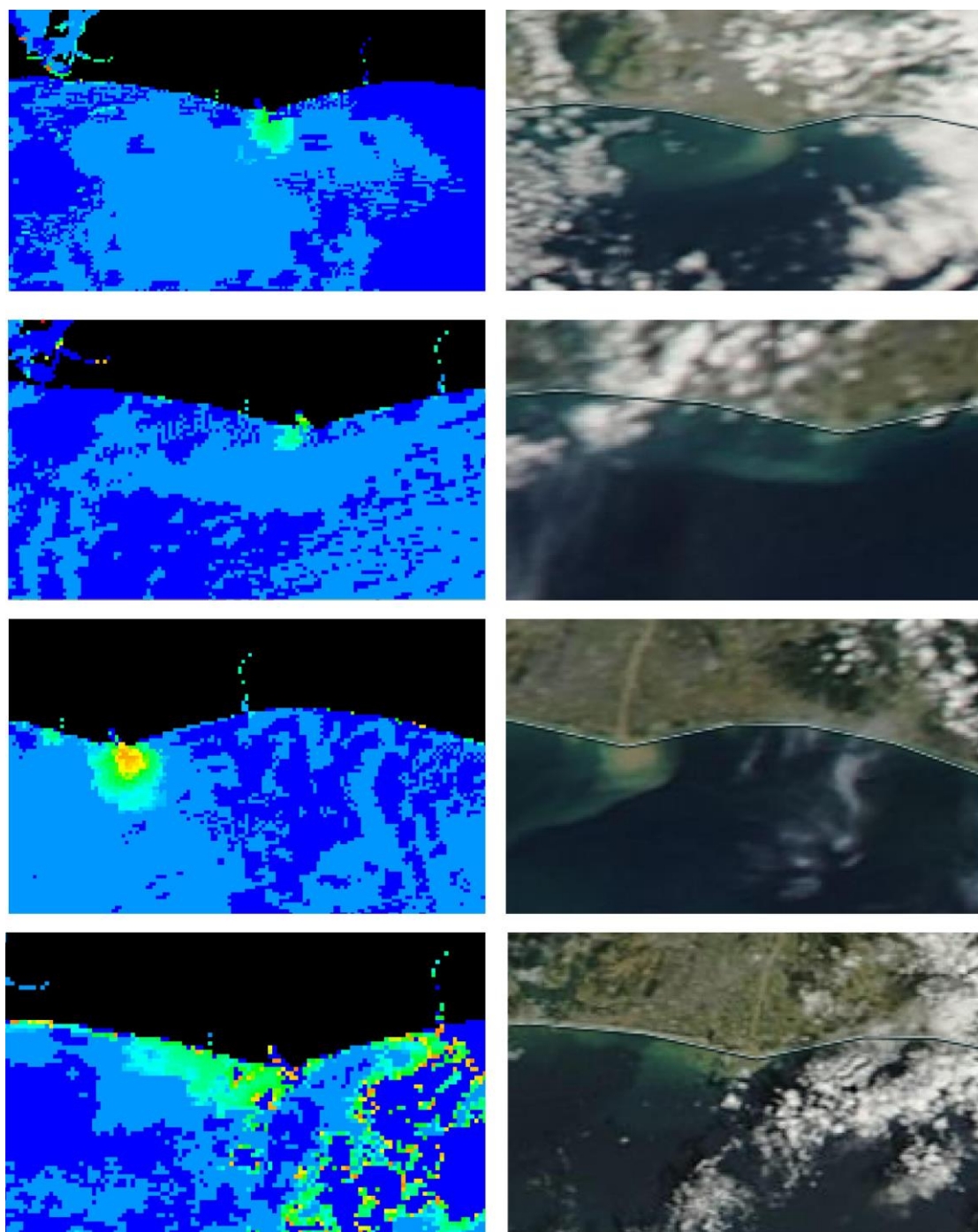
Figure 6.5 Performance of cloud masking

6.4 Trend of Turbidity Patterns

In this section, a cell-based estimation of the turbidity is used for the analysis of the turbidity variation from 2000 to 2015. After identification of the qualified pixels by the process of cloud masking and calculating normalized surface reflectance values, the average value of the normalized surface reflectance was calculated for each cell. The cells with numbers from 12001 to 14001 represent the alongshore direction from the west side to the east side of the mouth of the Tenryu River. Figure 6.1 (bottom) shows the corresponding cells.

6.4.1 Daily turbidity patterns

Figure 6.6 a-d represents the daily turbidity of cells from 12001 to 14001 in the alongshore direction over 16 years on the y-axis. The x-axis represents the Julian date of the corresponding year and cell 12901 represents the mouth of the Tenryu River.
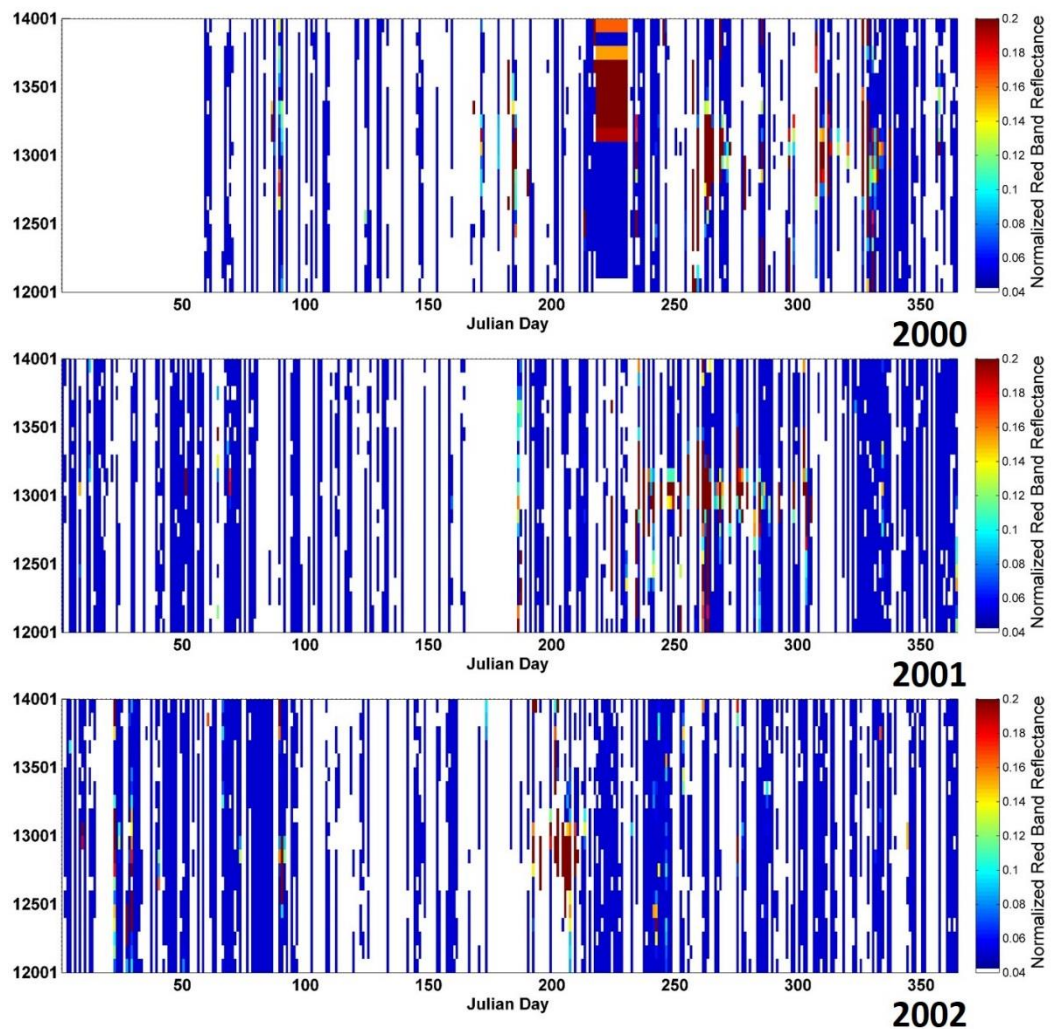
Figure 6.6 (a) Daily turbidity variation around Tenryu River from 2000 to 2002

86
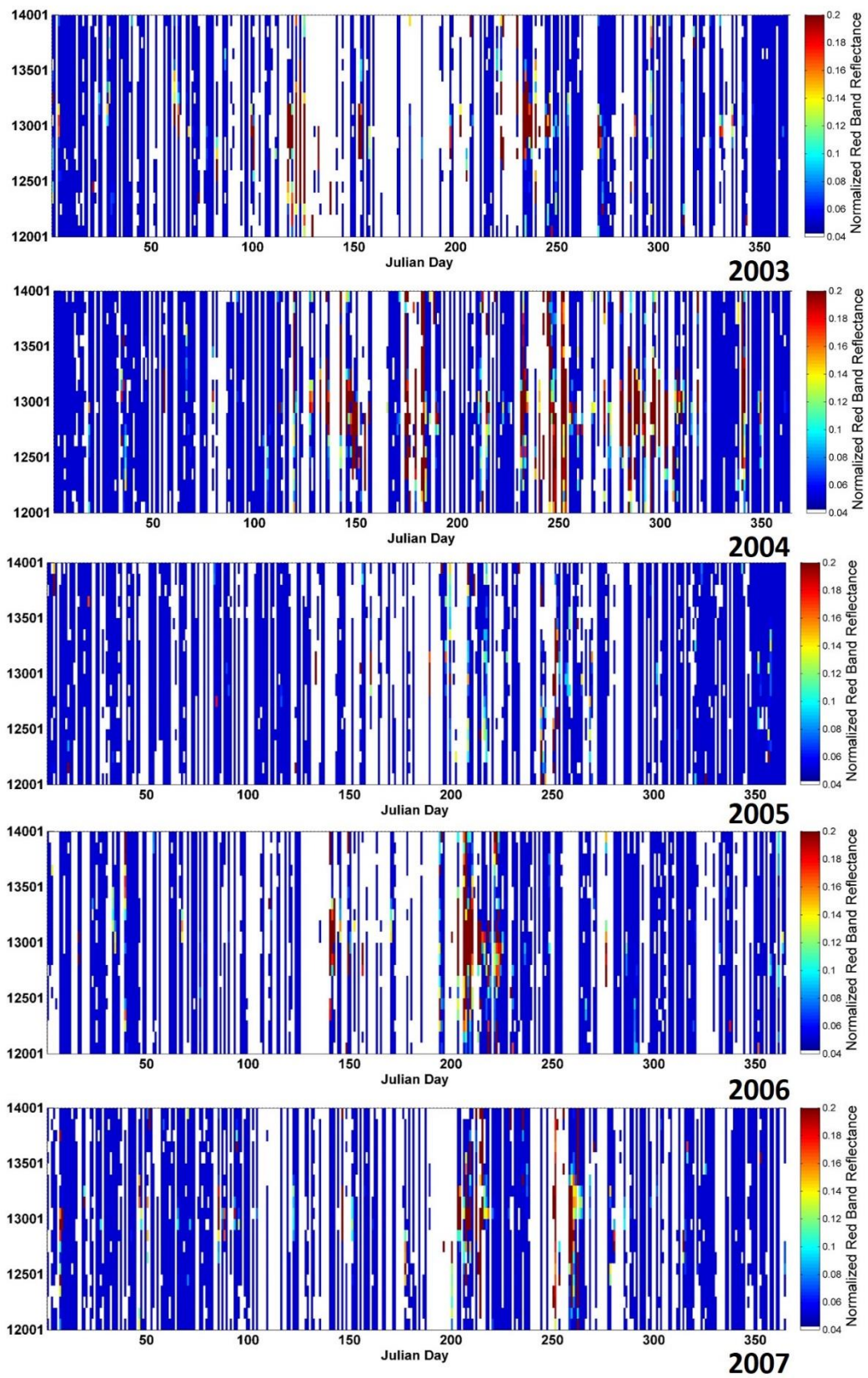
Figure 6.6 (b) Daily turbidity variation around Tenryu River from 2003 to 2007
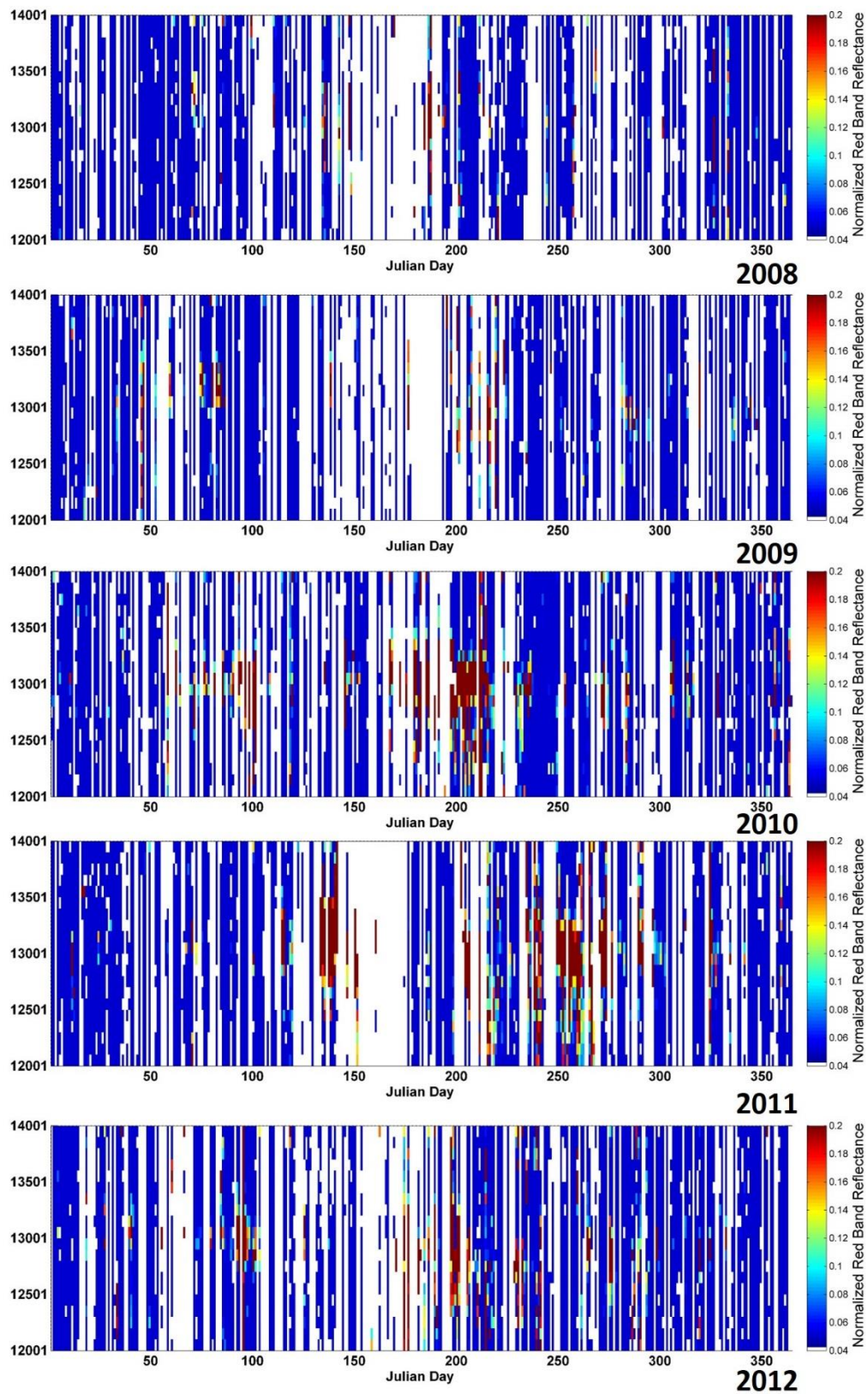
Figure 6.6 (c) Daily turbidity variation around Tenryu River from 2008 to 2012
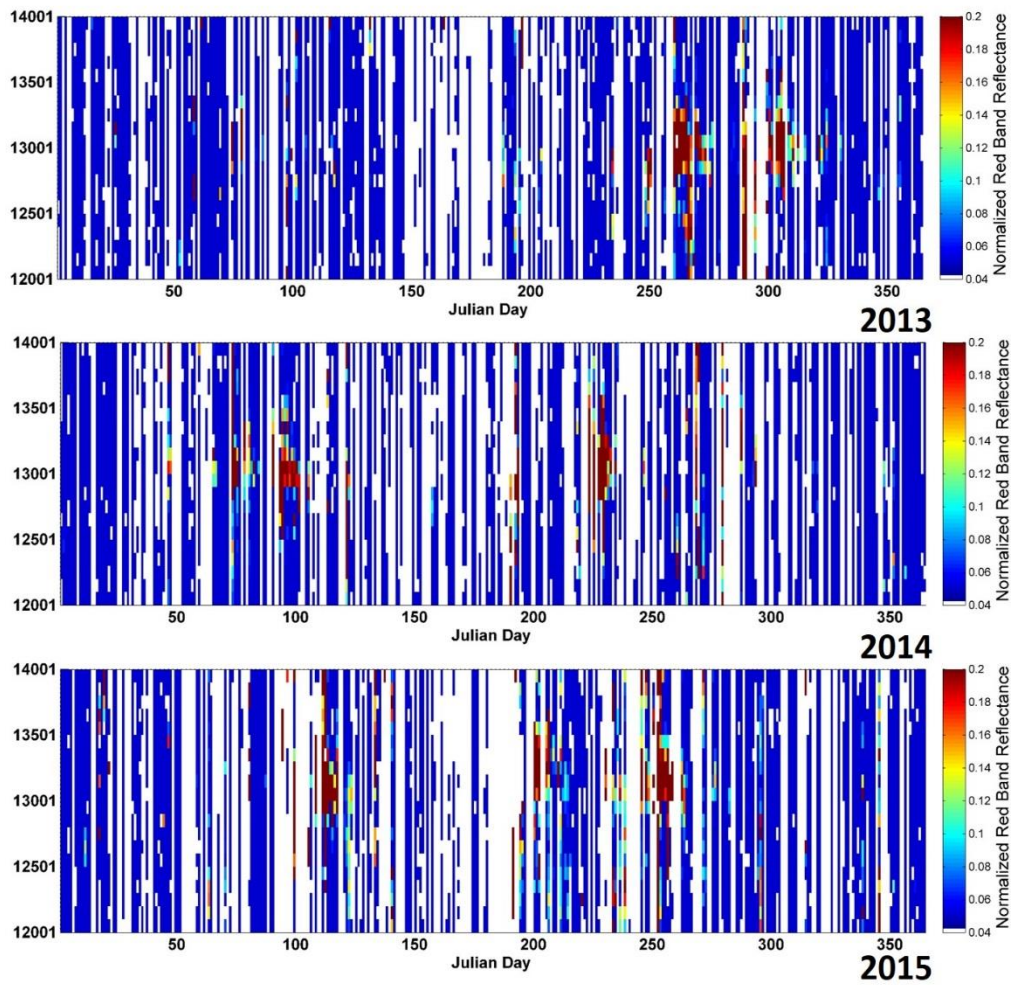
Figure 6.6 (d) Daily turbidity variation around Tenryu River from 2013 to 2015

The blank spaces in the above figure represent the missing data based on the cell-based analysis. Data availability is comparatively better than for the Vietnam study site.

The Julian dates around 150 to 200, i.e., days in June and July, show that there was less data available for the analysis. By looking at the cell-based daily average over the year, the following features in Table 6.2 can be extracted and Figure 6.7 illustrates the same observations in more understandable way.

Table 6.2 Extracted features from cell-based daily average turbidity variations

Year	Features
2000	Turbid plume entered into both sides of the river mouth; several high turbid discharge events (September to November)
2001	Turbid plume entered into both sides of the river mouth; several high turbid discharge events (August to October)
2002	West side dominant turbid plume at end of July; seems to be no high turbid plume afterwards
2003	Beginning of the year tends to have a turbid plume on both sides but after the middle of August an eastward dominant turbid plume was observed
2004	Turbid plume entered into both sides of the river mouth; several high turbid discharge events (May to November)
2005	Lesser number of turbid discharge events than previous year; more data are missing in July; no turbid discharge observed from September to December; difficult to extract the direction of turbid plume
2006	Turbid plume entered into both sides of the river mouth; no turbid discharge observed from September to December
2007	Turbid plume entered into both sides of the river mouth; no turbid discharge observed from September to December
2008	Appears to be a lesser number of turbid discharge events; dominant direction difficult to recognize
2009	Appears to be a lesser number of turbid discharge events; direction of turbid plume appears to be both sides
2010	Turbid plume entered into both sides of the river mouth; many high turbid discharge events all through the year (especially around end of July to beginning of August)
2011	Turbid plume entered into both sides of the river mouth; quite similar to previous year but higher turbid discharge events shift to month of September
2012	Turbid plume entered into both sides of the river mouth; a lesser number of turbid plume discharge events compared to previous two years
2013	Turbid plume mainly entered to east side of the river mouth; a lesser number of turbid discharge events (not observed before September);
2014	East side dominant turbid discharge observed; higher turbid discharge events observed from March to April and July to September; a lesser number of events at the end of the year
2015	East side dominant turbid discharge observed; higher turbid discharge events observed from March to September and a lesser number of events at the end of the year

Year	Features		
2000	●		↑↑
2001	●		↑↑
2002		▼	↑
2003	●	▲	↑↑↑
2004			↑↑↑
2005		☐	↑
2006	●		↑↑
2007	●		↑↑
2008		☐	↑
2009	●		↑
2010	●		↑↑↑
2011	●		↑↑↑
2012	●		↑↑
2013		▲	↑↑
2014		▲	↑↑↑
2015		▲	↑↑↑

● Both side turbid plume

▲ East side dominant turbid plume

▼ West side dominant turbid plume

☐ Direction can not decide

↑ Degree of dominant high turbid events

Figure 6.7 Summary of extracted features from cell-based daily average turbidity variations

Detail investigation is carried out to check the accuracy of the MODIS derived turbidity pattern and visual images of corresponding dates. Figure 6.8 shows the alongshore cell numbers where detail investigation is carried out. Figure 6.9 a-c represent the turbidity variations around the Tenryu River mouth from September 1 to September 9, 2015 and September 16 to October 3, 2015. Those figures clearly shows the alongshore turbidity variation in both East and West sides of the river mouth. There are three colors in the daily turbidity plot and in the corresponding visual images too. One color represents consecutive three days in the time period.

91
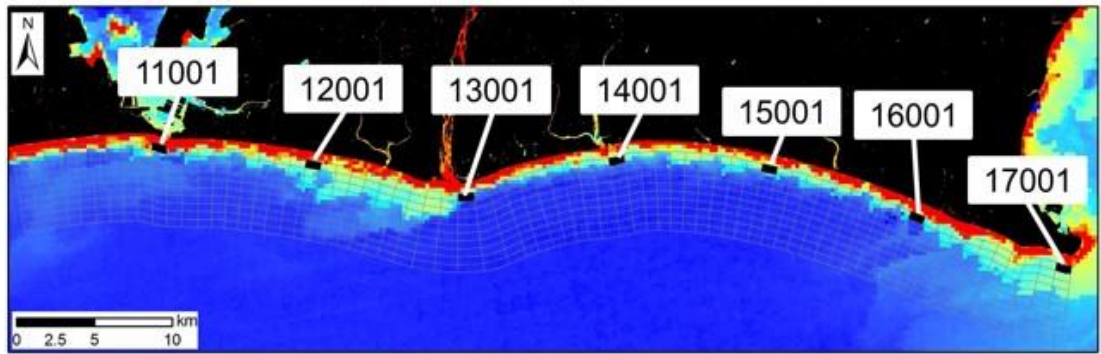
Figure 6.8 Alongshore cell numbers
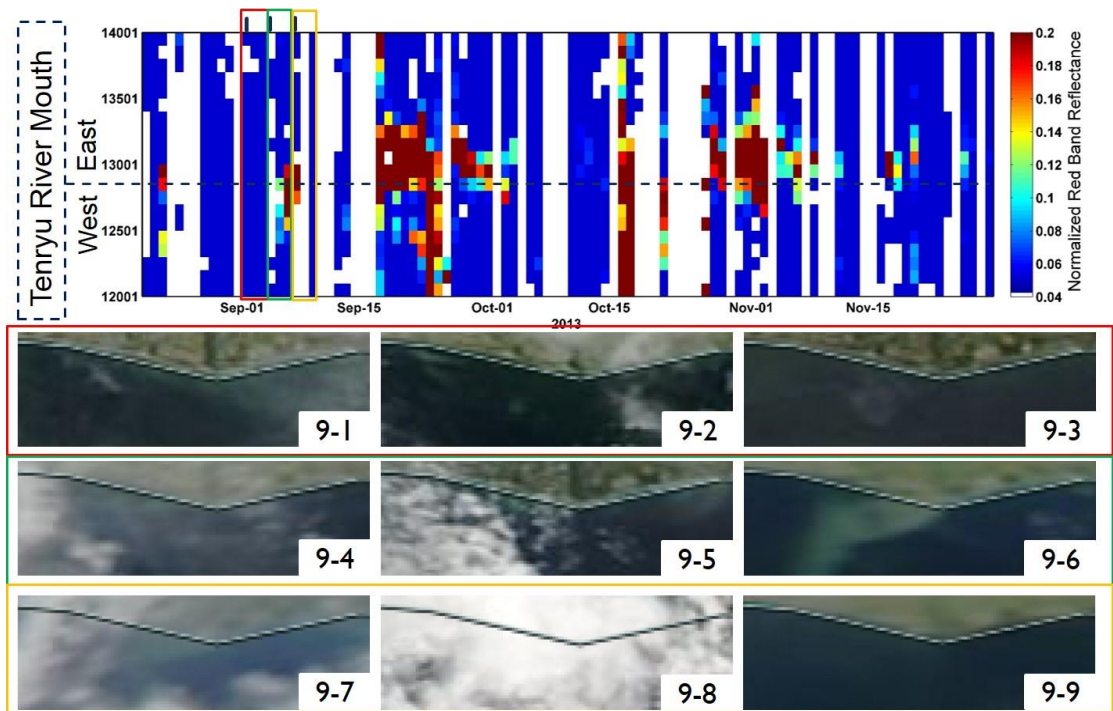
Figure 6.9 (a) Daily turbidity variations from September 1st to September 9th
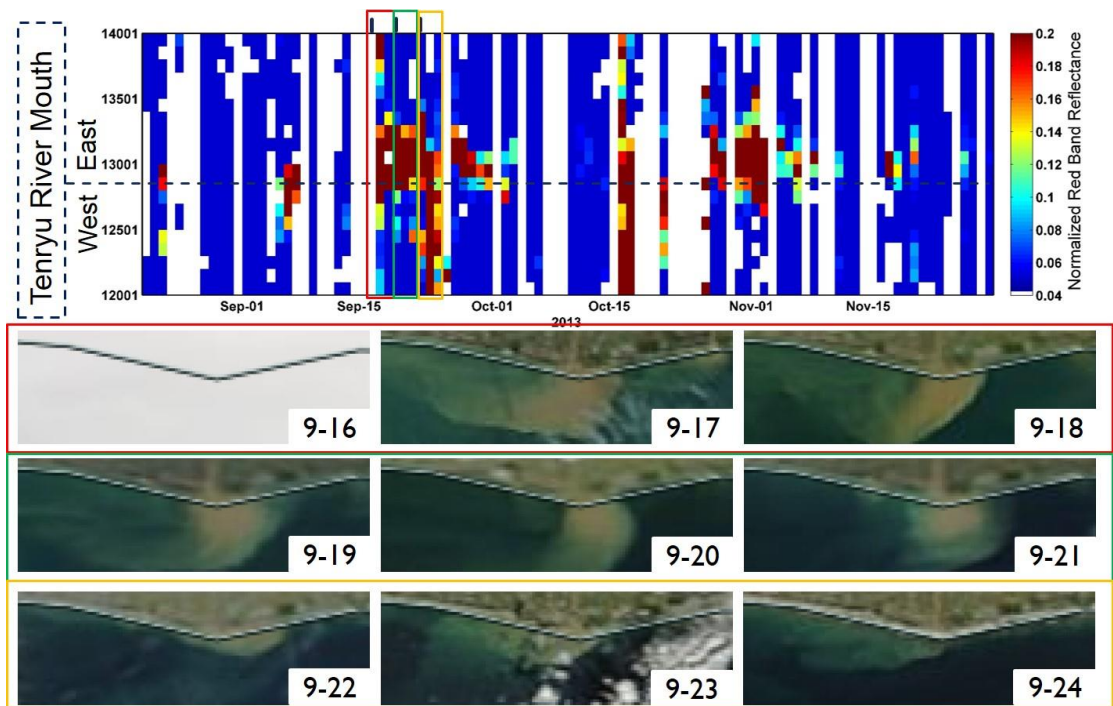
Figure 6.9 (b) Daily turbidity variations from September 16th to September 24th
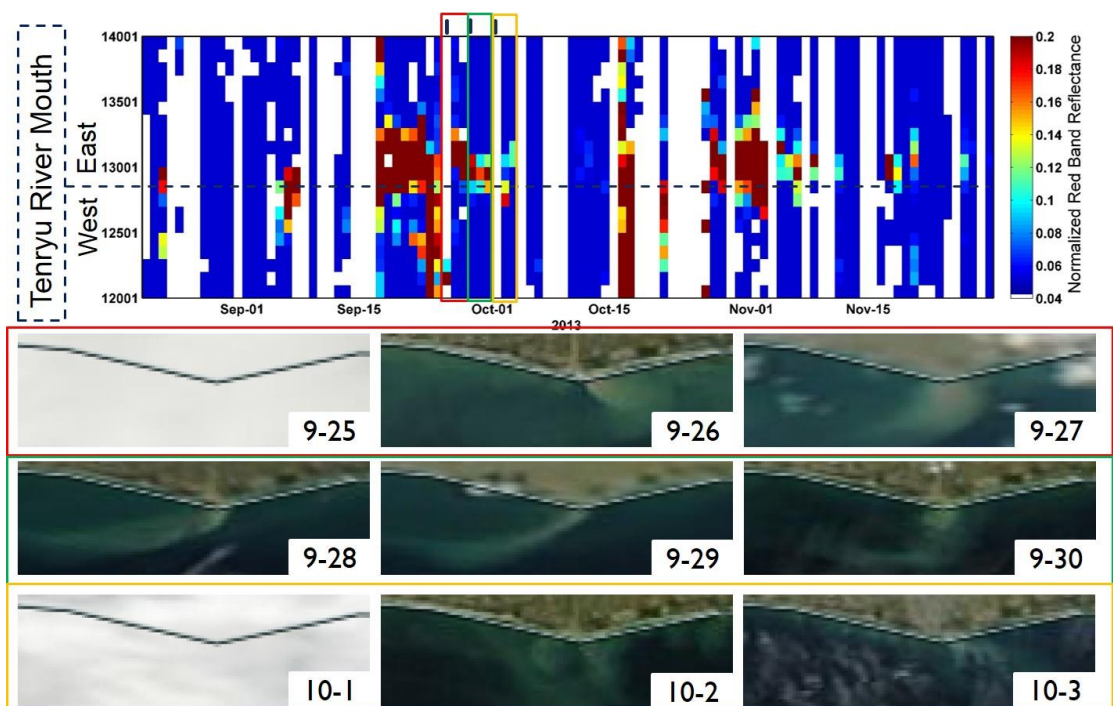
Figure 6.9 (c) Daily turbidity variations from September 25th to October 3rd

6.4.2 Monthly Average of Turbidity

The extracted values of the first set of cells along the coast, i.e., cells closest to the shoreline, were used to generate the monthly average from 2000 to 2015. Figure 6.10 shows the alongshore monthly average of turbidity alongshore. The y-axis and x-axis represent the alongshore cell numbers and months of each year, respectively. The figure clearly shows the highest turbid discharge patterns over a year. The accuracy of these results depends on the available data and can be referenced by Figure 6.6 which shows the daily turbid patterns. The month of June has relatively less data coverage compared to the other months at the Tenryu site.
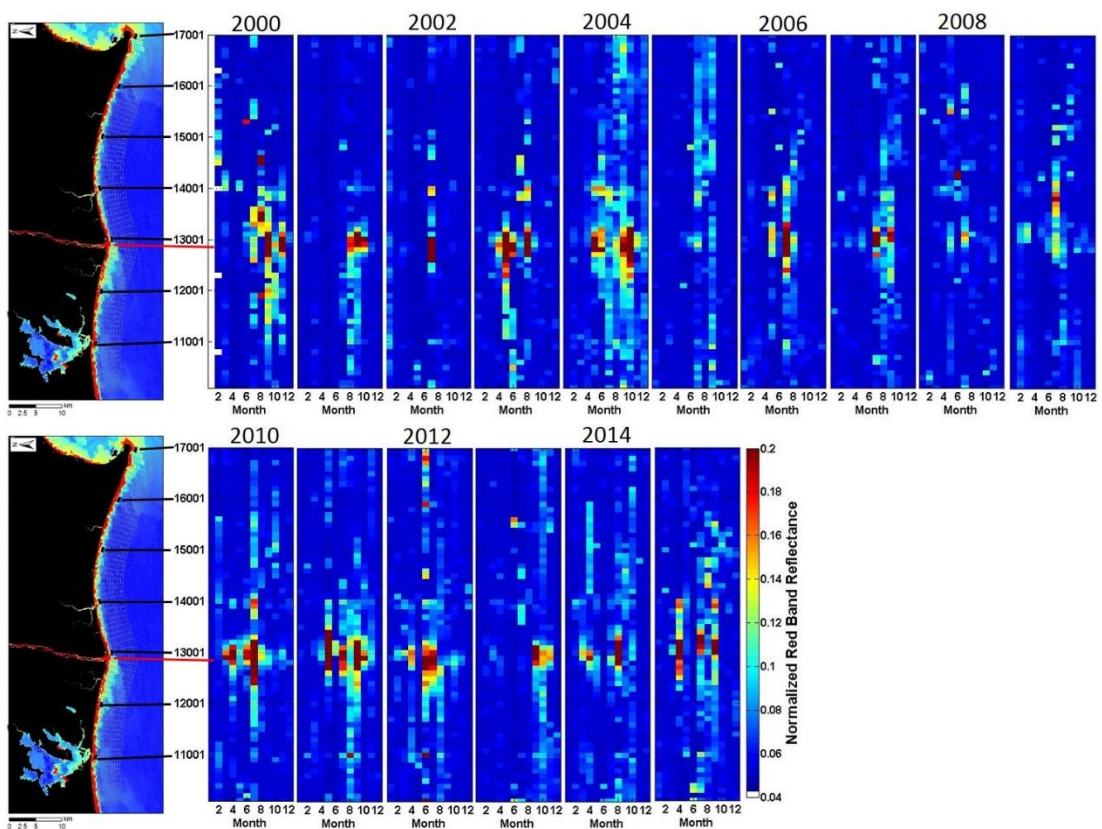
Figure 6.10 Cell-based alongshore monthly variation of turbidity

6.5 Detail Investigation around the Tenryu River

In this section, the area for a turbid plume is investigated for the Tenryu River water level over the period of time. The turbid plume is further divided into the east and west sides of the mouth of the Tenryu River for detailed investigation. At the end, several dates were selected to compare the turbid plume area with tidal variations.

94
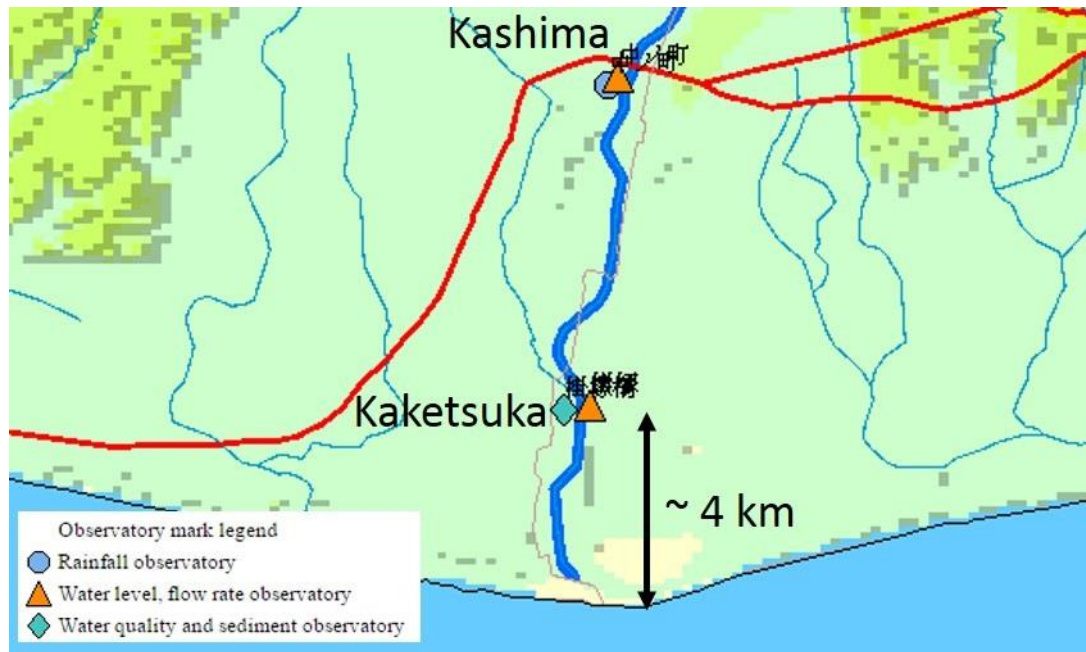
Figure 6.11 Location of Kakestsuka river gauge station

Hourly water level data were collected from the river gauge station at Kaketsuka from the following website; http://www1.river.go.jp/. Figure 6.7 shows the location of the Kaketsuka river gauge station, which is located 4 km inland from the river mouth. The map in Figure 6.11 is taken from the Water Information System of the Ministry of Land, Infrastructure, Transport and Tourism. The data is available from 2002 to the present, and the results of this analysis may enable us to find the dates of any higher turbid discharge for the missing data in 2000 and 2001.

6.5.1 Extraction of area of turbid plume

The extraction of an area of turbid plume is executed based on the pixel-based (not the cell-based) system. Figure 6.12 shows the diagram of the area calculation. This has been executed in Matlab software.

The same cloud masking algorithm is used to identify the qualified pixels for the analysis. The number of cloud-free pixels is identified for each day and the ratio of cloud-free pixels to the total number of pixels of each area is calculated. If the qualified pixels are 80%, then the Matlab routine output the area of turbid pixels. This part of the program output has four main features; the turbid area of the eastern part, the turbid area of the western part, the total area and the available data

95
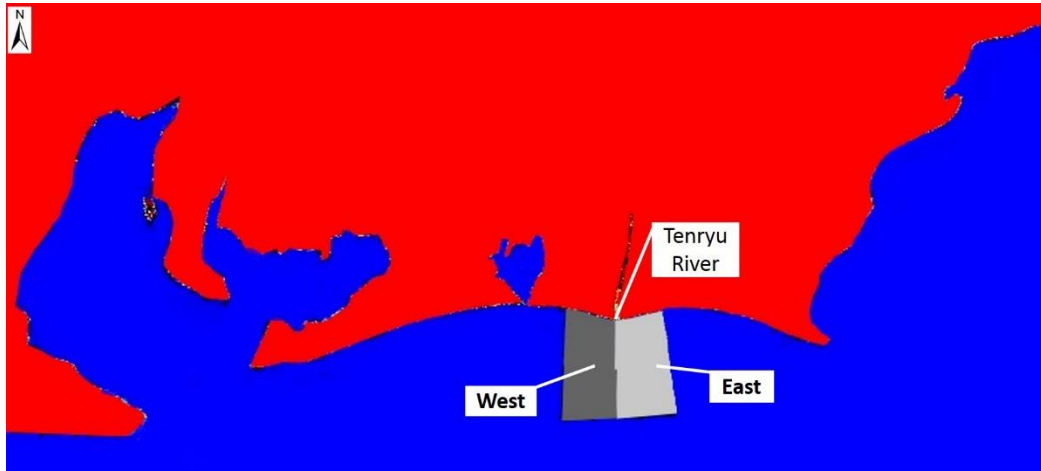
Figure 6.12 Map of area calculation

6.5.2 Time variation of the area

The daily average of the water level fluctuation at Kakestsuka river gauge station is calculated from the collected hourly data. After that, the river water level is plotted for the extracted areas of the eastern and western sides of the mouth of the Tenryu River.

Figure 6.13 (a)-(d) shows 16 years' variation of the turbid areas with the water level fluctuations. The areas' values are further sub-categorized based on the both the Terra (MOD) and Aqua (MYD) satellites. The black colored dots represent the area values of the west side of the mouth of the Tenryu River and the red dots represent the east side. The solid dot values are extracted from the Terra satellite and the dots with a white spot in the middle represent the values from the Aqua satellite. The gray lines represent the no data dates, mainly caused by the cloud cover. Due to graphic limitations, some of the white lines (dates with data) are not visible even though the area values are plotted. As the first MODIS data is available from end of February 2000, data in the first two months of 2000 are missing.

The dates with areas of higher turbid plumes closely correspond with the higher water levels at the river gauge station. Years 2002, 2005, 2008 and 2009 show areas of relatively low turbid plumes compared with other years. The east side dominant river turbid plumes can be observed in 2013, 2014 and 2015.

The turbid plumes seem to be equally distributed between both sides of the river mouth from 2000 to 2012 with little variation. Afterwards, turbid plumes were observed on both sides but the eastward side shows a clear trend. Interestingly, the end of July 2011 shows a sudden increase in the westward dominant turbid plume patterns.
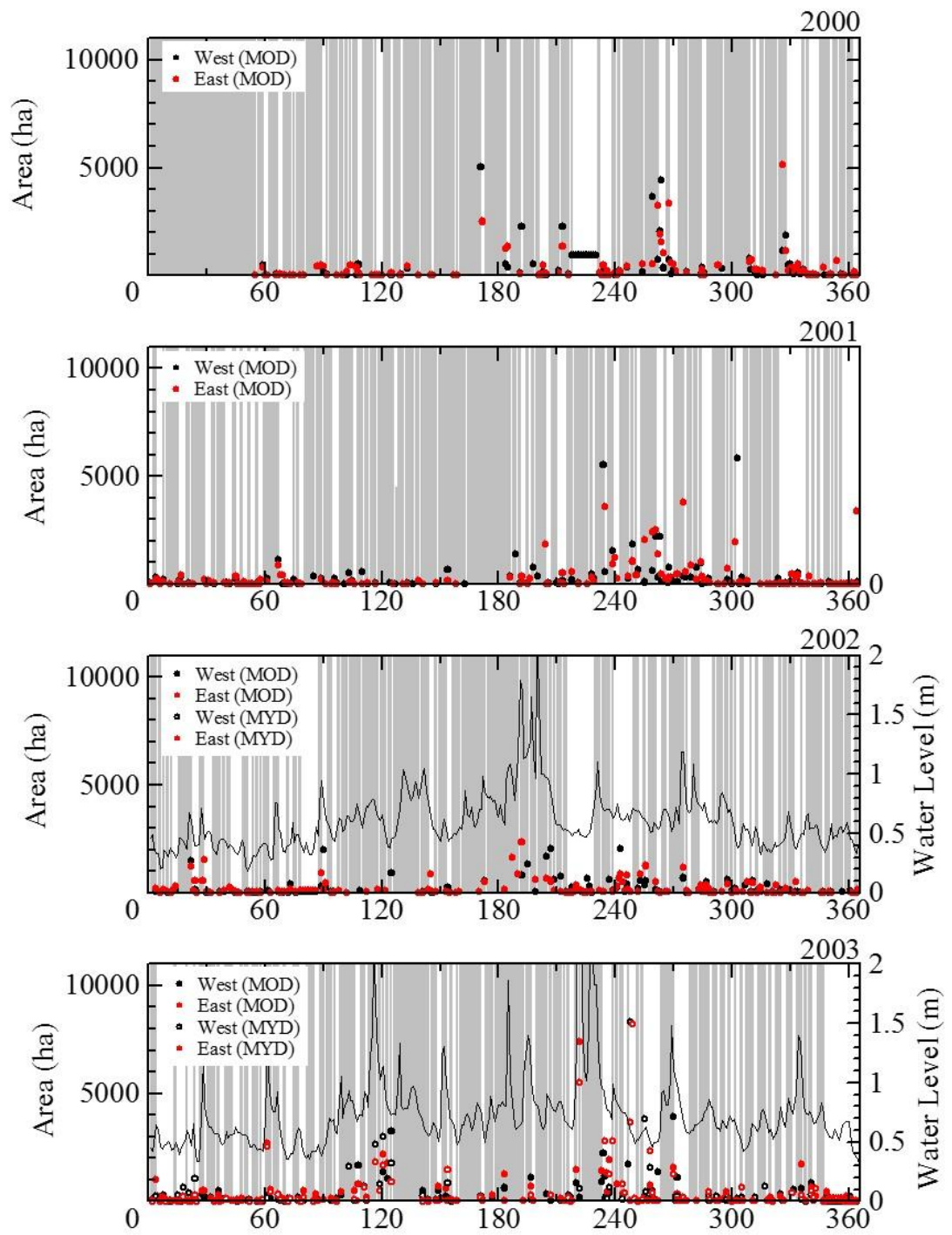
Figure 6.13 (a) Variation daily water level at the Kakestsuka station and area of East and
West turbid plume
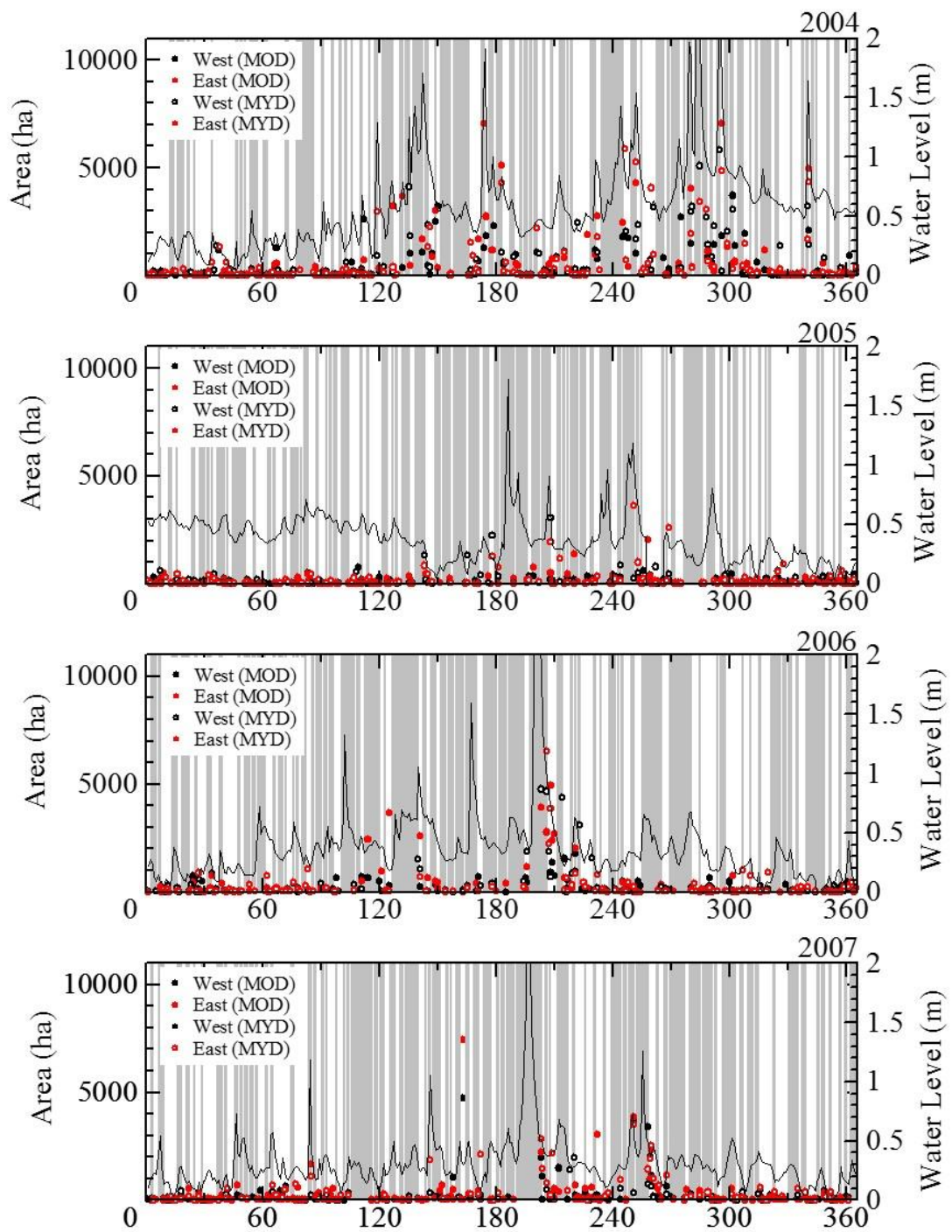
Figure 6.13 (b) Variation daily water level at the Kakestsuka station and area of East and West turbid plume
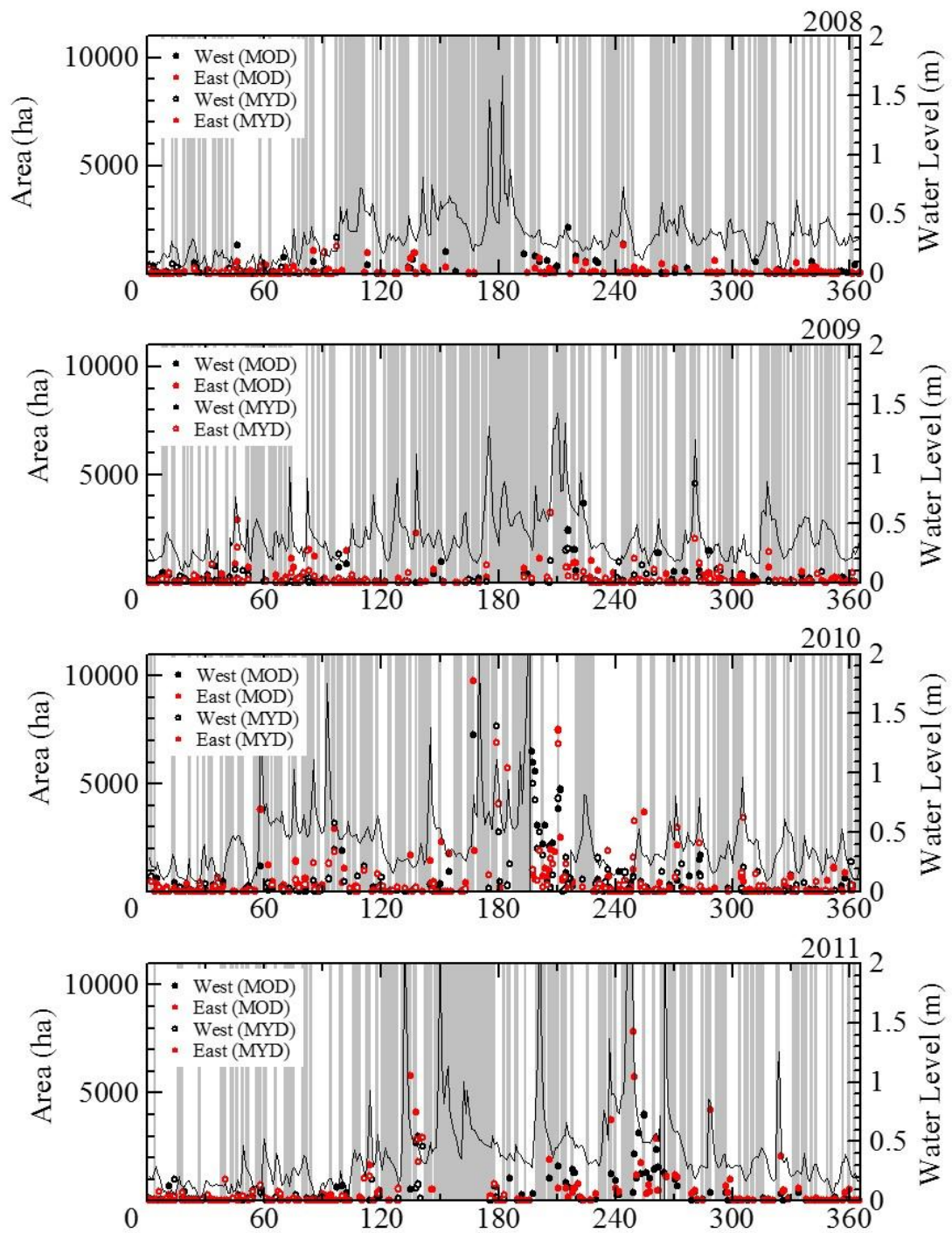
Figure 6.13 (c) Variation daily water level at the Kakestsuka station and area of East and West turbid plume
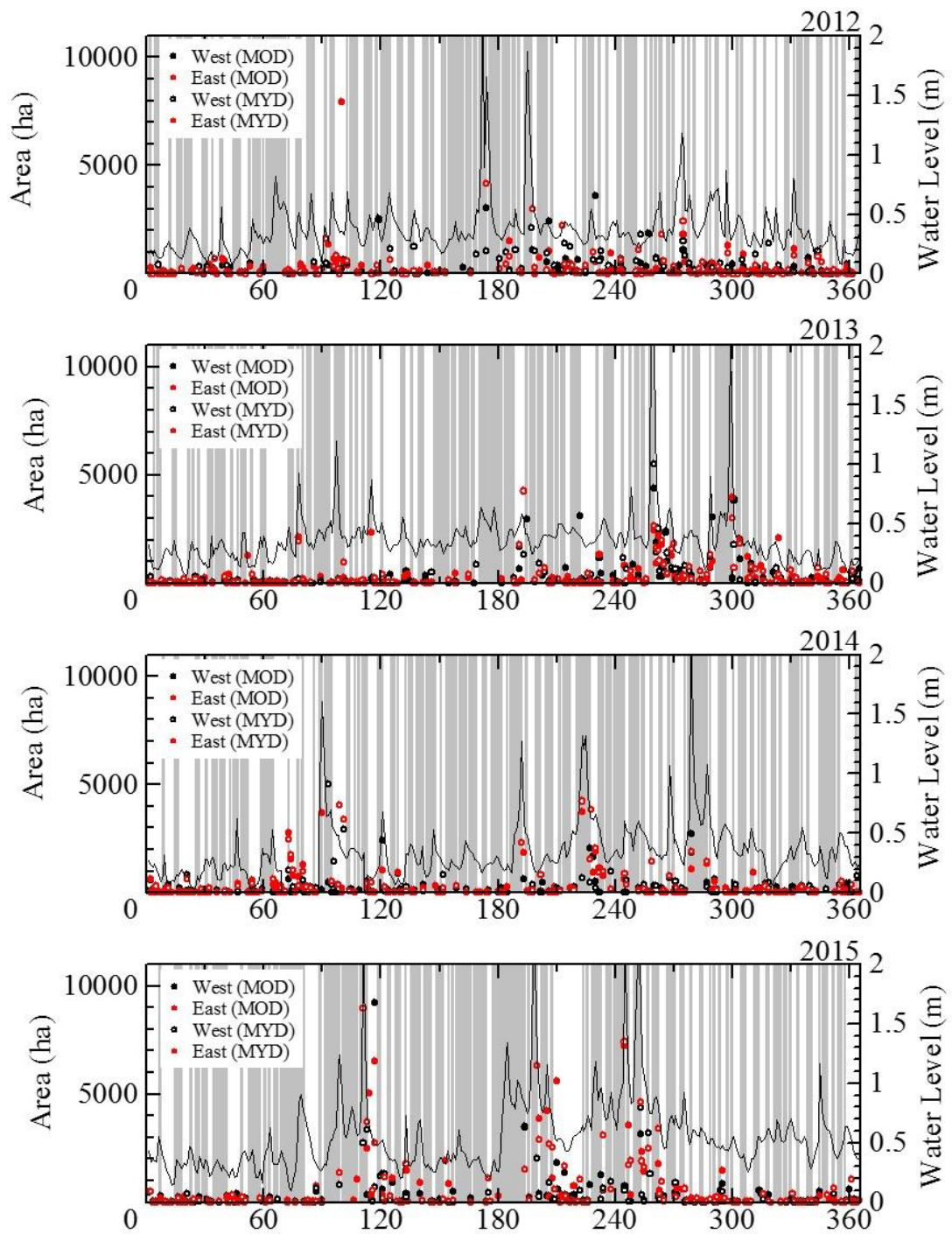
Figure 6.13 (d) Variation daily water level at the Kakestsuka station and area of East and
    West turbid plume

6.5.3 Relationship of the river water level and area of turbid discharge

The corresponding dates of available data were matched with hourly data at the Kaketsuka station. Figure 6.14 shows the relationship of the areas of turbidity plume and the water levels. When the water level is below 1 m, there is no correlation with the areas of turbid plume. However, with the increase of the water level, the river tends to produce larger areas of turbid plume. Years 2004, 2006, 2010, 2011, 2014 and 2015 produced higher turbid plumes than the other years.
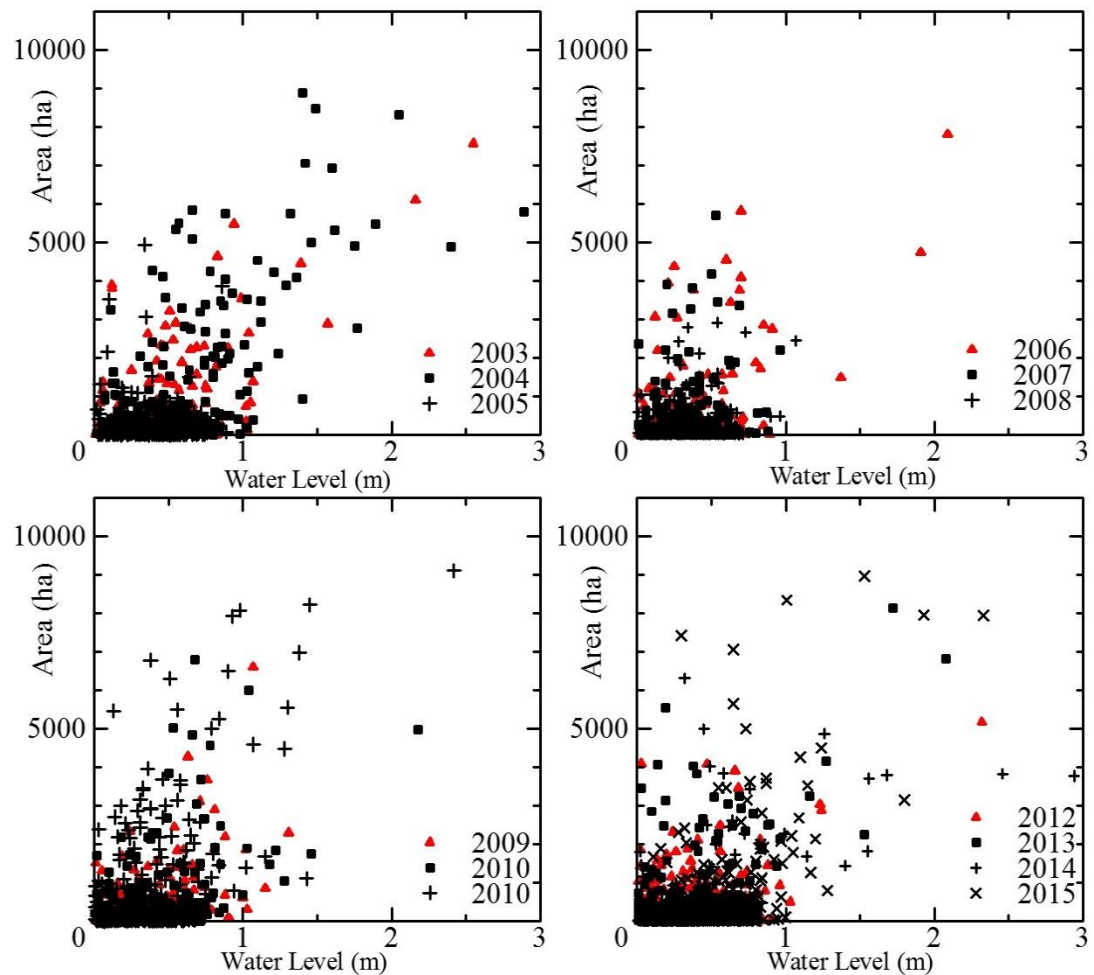
Figure 6.14 Relationship of water level and turbid plume area

6.5.4 Tidal influence on turbidity patterns

Several days in the month of September 2015 have been selected to compare the turbid discharge distribution in nearshore areas with the tides and water levels of the mouth of the Tenryu River. Figure 6.15 shows the Terra (MOD) and Aqua (MYD) images on
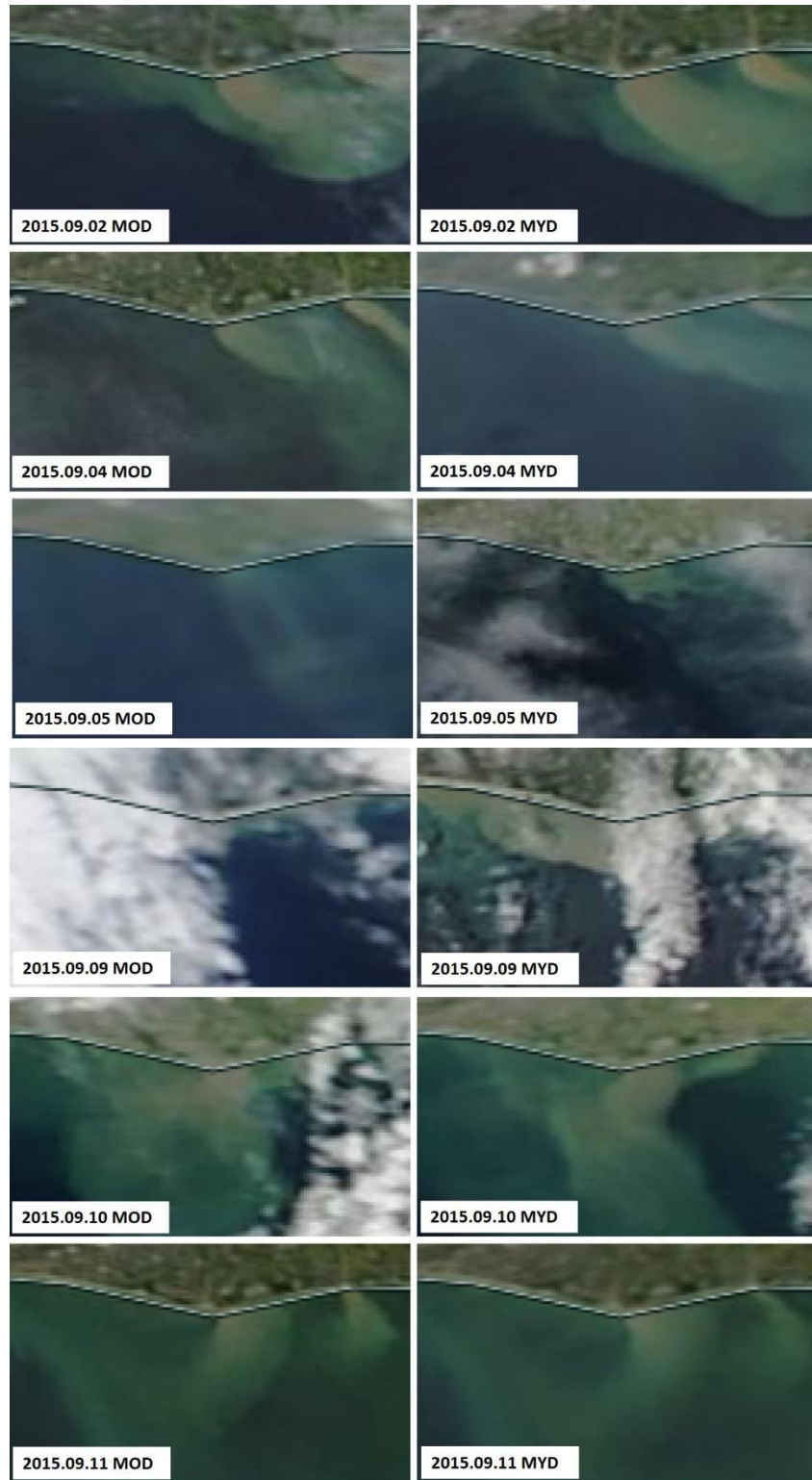
Figure 6.15 Cloud status of utilized MODIS images in September 2015

the 2nd, 4th, 5th, 9th, 10th and 11th September 2015. Table 6.3 illustrates the summary of the visual assessment of turbid plumes and the cloud status of the images in Figure 6.15. The hourly water level at the Kakestsuka water gauge station and hourly tidal

data at the Omaezaki tidal station are used to discuss the relationship with the patterns of the areas of turbid plumes. The Terra (MOD) satellite observes the area around 9:30 am and the Aqua (MYD) satellite observes at around 12:30 pm.

Figure 6.16 illustrates the river water level, tidal variation, area of turbid plume and direction of turbid plume. The eastward dominant turbid plume could be observed during the ebb tide, and it can be clearly seen on September 2nd, 4th 5th and 11th. The turbid plume on September 9th is clearly seen on the west side but it seems to be spread through to both sides of the river mouth, although the east side is covered by a cloud patch. On September 10th, the turbid plume also spread through to both sides of the river mouth. Both September 9th and 10th fall in the flood tide phase.

Table 6.3 Visual assessments of satellite images in Figure 6.15

Date	Satellite	Dominant side of the turbid plume	Magnitude of turbid plume
2015.09.02	Terra (MOD)	East	Relatively high
	Aqua (MYD)	East	Relatively high
2015.09.04	Terra (MOD)	East	Relatively low
	Aqua (MYD)	East	Relatively low
2015.09.05	Terra (MOD)	East	Relatively very low
	Aqua (MYD)	East	Relatively low
2015.09.09	Terra (MOD)	Cloudy	Relatively high
	Aqua (MYD)	Both sides (east side could be visible through a cloud patch but it has been masked out by the process)	Relatively high
2015.09.10	Terra (MOD)	Both sides	Relatively low
	Aqua (MYD)	Both sides	Relatively low
2015.09.11	Terra (MOD)	Both sides but dominant on the east	Relatively low
	Aqua (MYD)	Both sides but dominant on the east	Relatively low
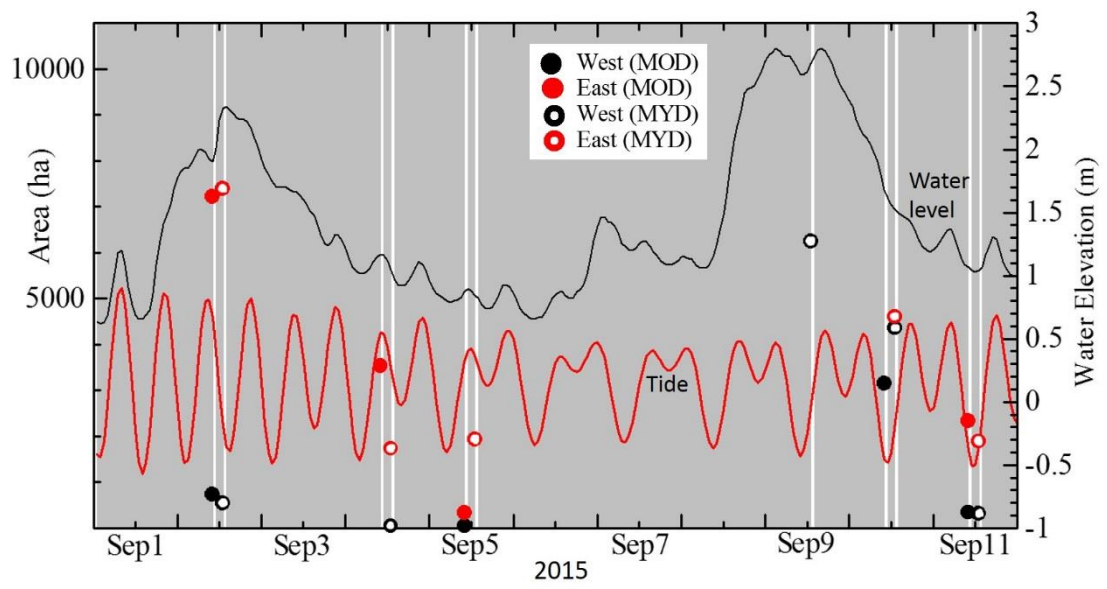
Figure 6.16 Comparison of the tide and water level with turbid plume area

CHAPTER SEVEN

SATELLITE-BASED ANALYSIS OF AN EXTREME WEATHER EVENT IN A COASTAL AREA -TYPHOON HAIYAN

7.1 Introduction

The Philippines is highly prone to tropical cyclones due to its geographical setting in the West Pacific Ocean (Webser et al., 2005) Surrounded by sea water with a relatively high surface temperature, the Philippines receives a considerable number of typhoons every year (Wikipedia., 2014).

Typhoon Haiyan was the second deadliest typhoon recorded in the Philippines and became the strongest typhoon at the time of landfall. The typhoon reached Eastern Samar on November 8, 2013, at around 4:40 a.m. local time. While the severest damage was observed in Tacloban, this study focused on the east coast of the island of Samar, which faces directly to the Pacific Ocean. The observed inundation heights along the coast were much higher than the numerically predicted wind-driven storm surge level while the phase-averaged wind-driven wave generation model predicted significantly high stormy waves (Tajima et al., 2014). The coast is mostly covered by a fringing coral reef, which should have the potential for significant wave attenuation through the combined effects of bed friction and breaking. On the other hand, the reef may have a certain influence on the amplification of the water level on the reef due to the setup and wave trapping effects.

The focus of this study is, thus, to capture the overall inundation characteristics along the coast of Eastern Samar and investigate how these characteristics are related to various physical features such as the width of the fringing coral reef, estimated wave heights, and local beach topography conditions. The damage of alongshore vegetation, including mangroves, was also examined through the analysis of satellite images and numerical wave simulations.

7.2 Study Area and Satellite Images

This study especially focuses on the southern part of Eastern Samar. Along nearly 80 km of coastline strip of the east coast, several sites were selected for this study.

Figure 7.1 illustrates the map of the study area and the small map in the upper right corner shows the typhoon's track overlaid on the boundary of the Philippines

Very high resolution (VHR) satellite images were used to capture the impact of Typhoon Haiyan on the target coast. WorldView-2 pan-sharpened multispectral 50cm resolution satellite data were used to capture the area before the typhoon. The image mosaic consists of images from the year 2011 to those of November 2013.

Satellite images after the typhoon were obtained from the USGS Hazard Data Distribution System under the public access policy (U.S. Department of the Interior, U.S. Geological Sur-vey/ Hazard Data Distribution System). The system is dedicated to the provision of quick and easy access to imagery and geospatial data during emergency response and recovery operations. Several images, including QuickBird and WorldView-2 data with 3m resolution, were used. Since the data were highly distorted due to the instant provision of the data for emergency response activations, all the post-typhoon images were rectified to pre-disaster images. The Google Earth images after the typhoon were used to fill the gaps of the post-typhoon image data set.

LANDSAT 8 with 30m resolution satellite images was used to evaluate the change in the vegetation cover, especially the mangrove coverage, along the coast of Matarinao Bay. The data were freely obtained from the U.S Geological Survey (http://eros.usgs.gov/) before and after the landfall of Typhoon Haiyan.

Right after the typhoon, the post-disaster survey was jointly conducted by the Japan Society of Civil Engineering, JSCE, and the Philippine Institute of Civil Engineers, PICE Tajima et al., 2014), and this study applied their survey results such as the beach slopes, inundation boundary and inundation height at some locations (Figure 7.1). The research team later conducted a follow-up survey. All the data were provided for this analysis.
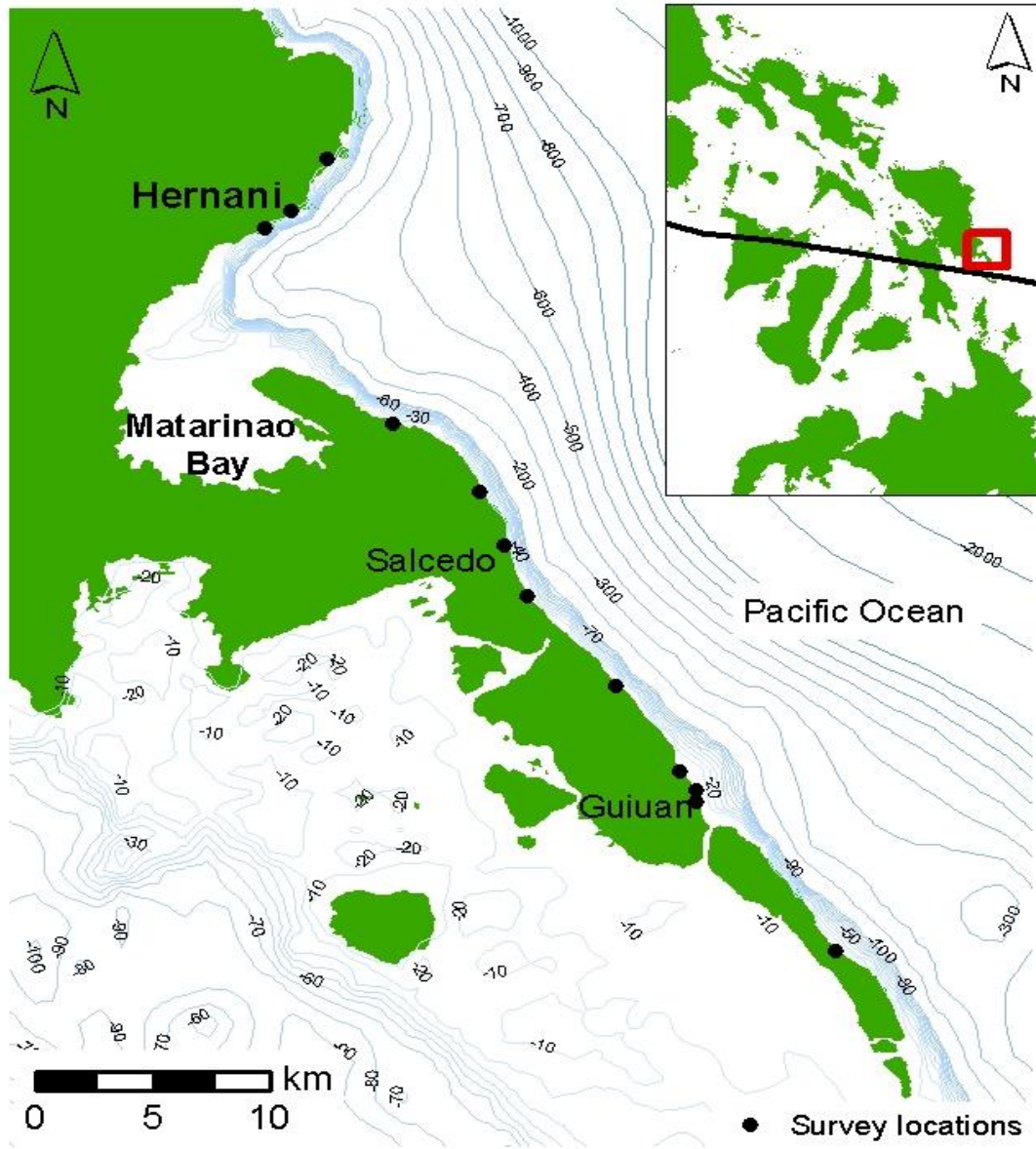
Figure 7.1 Study area

7.3 Methodology

7.3.1 Overview

Figure 7.2 shows the flow chart of the analysis.
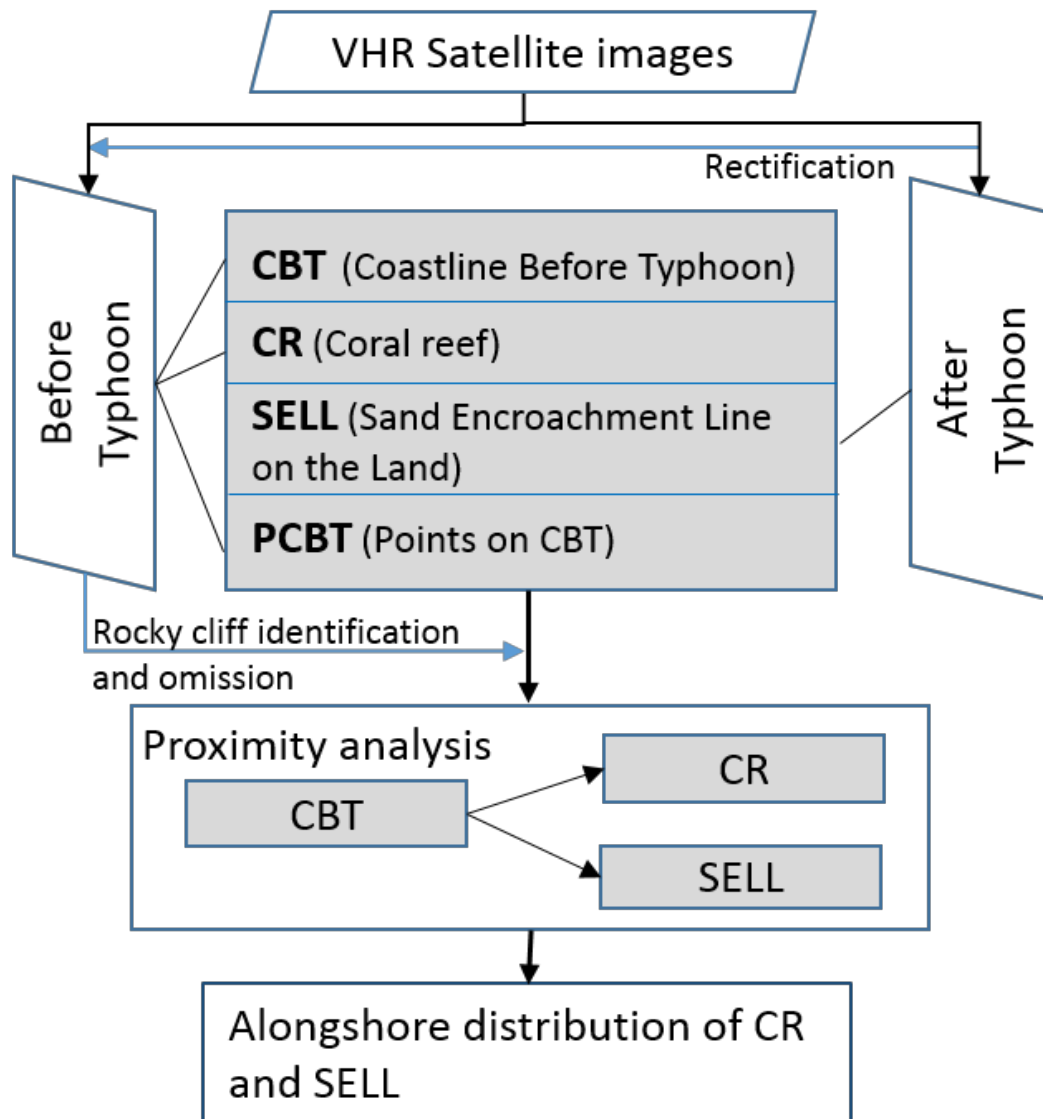
Figure 7.2 Methodology of the VHR satellite image analysis

7.3.2   Feature extraction

Post-disaster VHR satellite images contained uneven illumination and haze which could lead to erroneous results in automated classification. Hence, visual interpretation techniques were adopted for extracting information from the VHR satellite data. Figure 7.3 illustrates the quality of the pre- and post-typhoon VHR satellite data.

Figure 7.3 (a) pre-typhoon image (b) post-typhoon image

Coral reef (CR), coastline before typhoon (CBT) and sand encroachment line on the land (SELL) were extracted from the satellite data. The SELL is a good indicator of extent of the inundation due to storm waves, and it was clearly recognized by the clearance of soft vegetation cover near the beach.

Then, proximity analysis was performed by taking the CBT as the baseline. The distance to the SELL and the edge of the CR were calculated at 100m intervals along the CBT. Figure 7.2 shows the flow chart of the analysis. The distance analysis was performed with the help of the Digital Shoreline Analysis System (Thieler et al., 2009) which is a freely available software application that works within the Environmental Systems Research Institute's (ESRI) ArcGIS software (v. 10).

7.3.3   Image classification

Vegetation analysis was performed to detect the changes inside Matarinao Bay using medium resolution LANDSAT-8 multispectral imageries. In the first step, bands 2 to 7 were used for the iso-clustering which clustered the natural grouping of pixels into multivariate data. The clustered results were used for the final unsupervised 40 classes of classification with the maximum likelihood algorithm. In the final step of the classification, the 40 classes were further narrowed down to several classes by cross-interpretation with the aid of VHR satellite images and field observations. The selected classes were mangrove, forest, mixed forest, disturbed

109

forest (after the typhoon), bare land, sea, clouds and shadow. All the image processing was conducted within the ArcGIS software and its tools.

To do the change analysis, the same classifications were applied to both pre- and post-typhoon images. The obtained vegetation change results were then compared with the wave heights inside the bay estimated through the following numerical analysis.

7.3.4 Numerical analysis of wave-sheltering effect

As seen in Figure 7.1, Matarinao Bay is highly sheltered by the peninsula located to the north of Salcedo; thus, the mangrove forest is well developed, especially inside the bay, while the bay directly faces the Pacific Ocean. To investigate the overall characteristics of the "sheltering effect" of the bay under the stormy wave conditions, we carried out numerical experiments. This study applied a linear mild slope equation (Ohnaka e al., 1989) for computations of wave shoaling, refraction and diffraction around the bay. Focusing on diffraction and refraction, the breaking dissipation was not accounted for in this computation. The incident wave angle was set to be 4 degrees northward from the east based on the numerical estimation of the wind-driven waves3). We assume that the wave spectra are highly concentrated during the storm and the single incident wave period, either T=15s or 20s, and the incident angles, of 40, 90 and 140 northward from the east and 10 and 40 southward from the east, were applied for computation of the wave field of the highly concentrated frequency spectrum. Then, spatial distributions of the computed wave heights were integrated with weight which was determined based on the Mitsuyasu-type wave directional spectra (Mitsuyasu H., 1968) with Smax=75. Bathymetry data were obtained from the National Mapping and Resource Information Authority and used for the study.

7.4 Results and Discussion

7.4.1 Alongshore distribution of sand encroachment line

Figure 7.4 illustrates the local variation of the SELL in Section 2 (in Figure 7.5). As seen in the figure, there are several rocky cliffs exposed to the shoreline and these cliffs form pocket beaches along the coast. The VHR satellite images clearly show

the changes before and after the typhoon. Furthermore, the sand movement towards the sea is clearly visible in the post-disaster images.
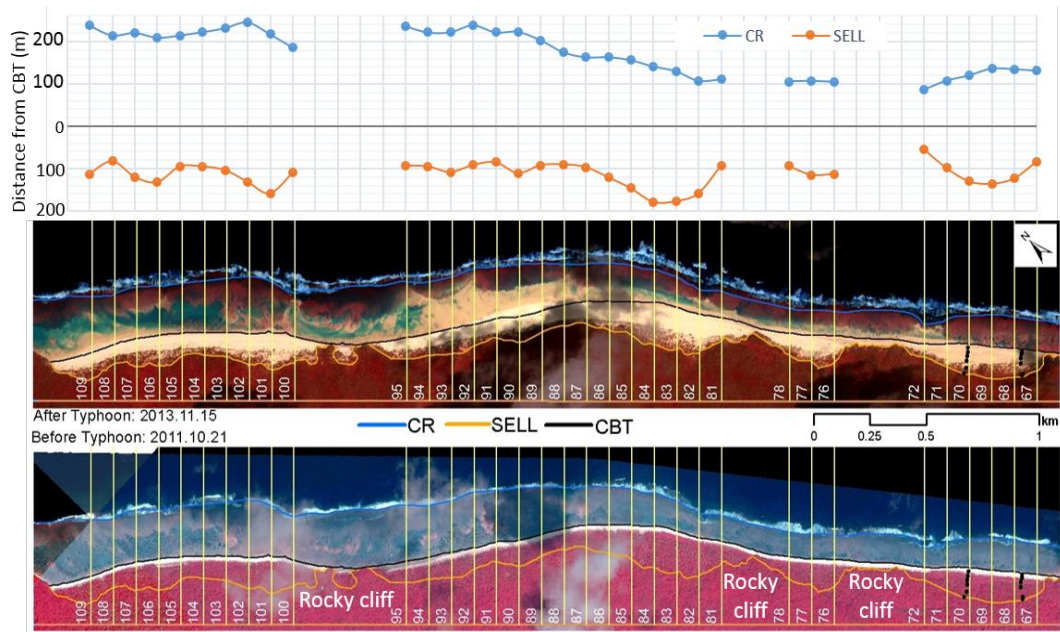
Figure 7.4 Local variation of SELL and CR (above), extracted CR, SELL and CBT overlaid on pre- and post-typhoon VHR satellite images

Figure 7.5 shows the alongshore distribution of the distance from the CBT to either the CR or SELL estimated through the satellite images. Figure 7.6 shows the relationship of each distance. The figure distinguishes the data obtained from the different four sections, specified in Figure. 7.5, by using different symbols. In the figure, data were not plotted at several locations where rocky cliffs were exposed to the coral reef.

Figure 7.6 appears to have different relationships in different sections. Section 1 is around Hernani and the angle of the shoreline towards the incident waves differs from the other sections. Sections 2 and 3 show a peak of the SELL along the CR, and this result somehow implies that a reef with a certain width may cause amplification of stormy waves. The absence of good terrain data limits further explanation. In section 4, around Guiuan, the low-elevated wide plain is extended behind the shoreline, so that the observed distance between the CBT and the SELL was much longer than those of the other sections.
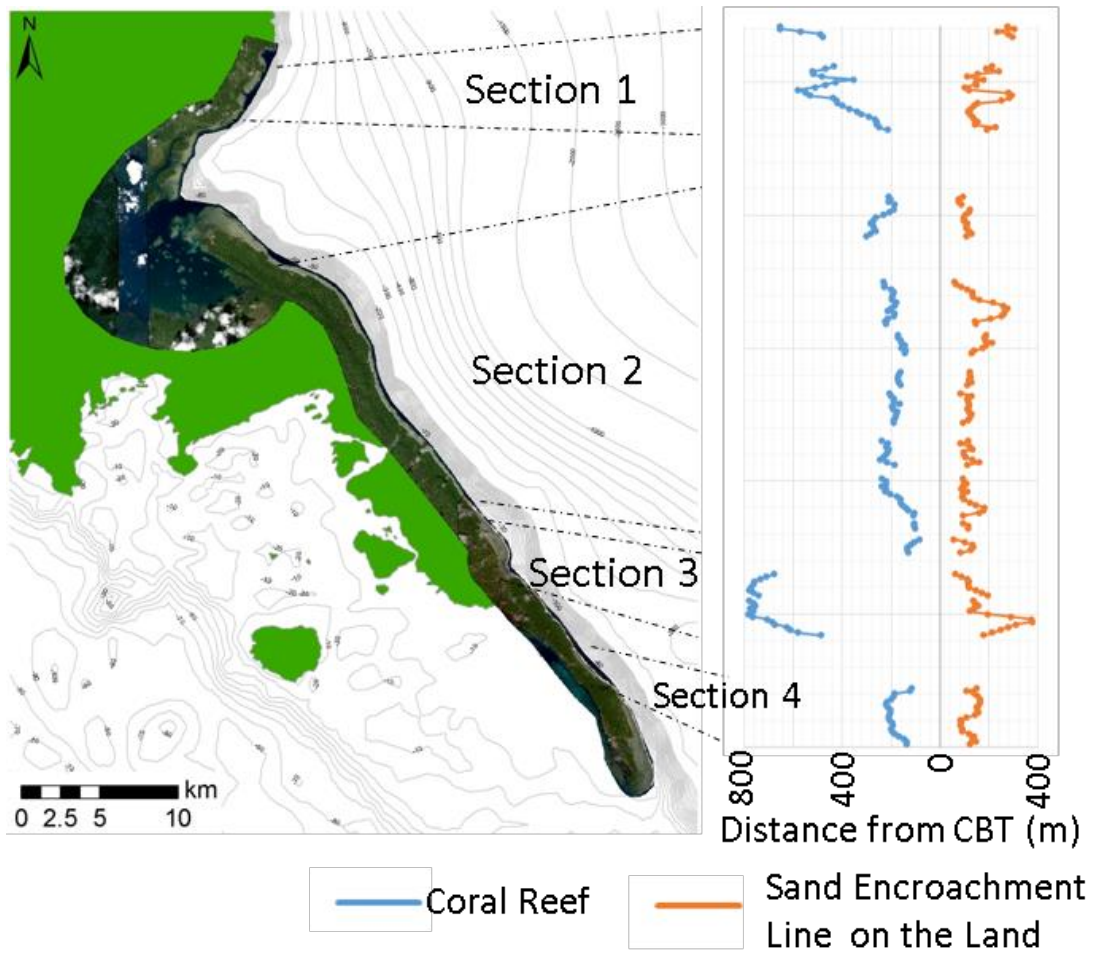
Figure 7.5 Alongshore distribution of the CR and SELL
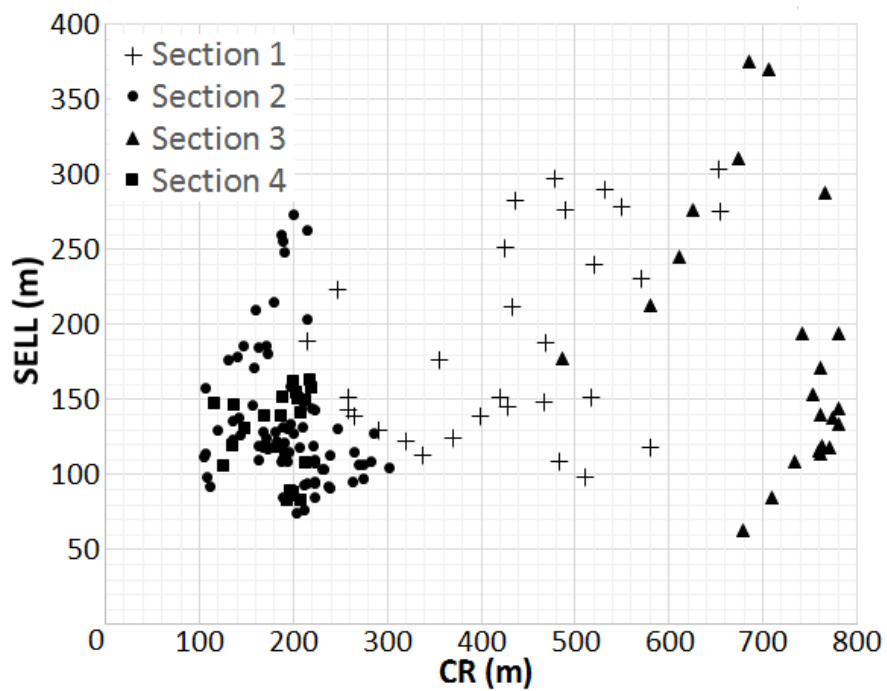
Figure 7.6 Relationship between the CR and SELL

7.4.2 Vegetation analysis

Figure 7.7 (a) and (b) show the LANDSAT-8 images used for the analysis and (c) shows the results' classification analysis. It is clearly visible that the strip of mangrove inside the bay remains unchanged even after the typhoon (the yellow color). On the other hand, the red color represents the damaged mangrove on the small islands outside the bay.
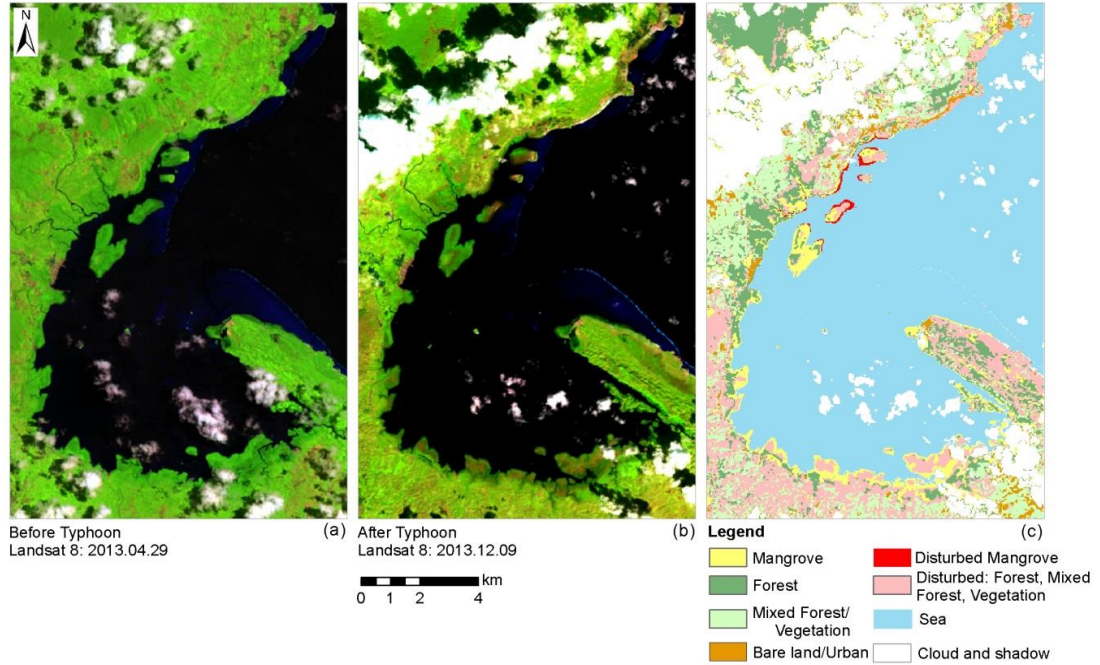
Figure 7.7 (a) Before typhoon LANDSAT-8 image, (b) After typhoon LANDSAT-8 image, (c) Results of change analysis

In contrast, the pink color represents the disturbed forest, mixed forest, and other vegetation. Since the surrounding coastal edge of the bay was not damaged, most of the damage in the pink color could be due to the wind force, a non-wave interaction mechanism. Other categories represent the remaining land cover classes. The vegetation analysis needs to be further investigated with ground truth data and supervised image classification.

7.4.3　Wave-sheltering effect of Matarinao Bay

Figure 7.8 shows the bathymetry data and the results of computed wave heights when the incident wave period was T=15s and 20s, respectively. It is clearly visible that the wave heights inside the bay are much smaller than those along the north coast of the bay where Hernani is located. It is also interesting to note that refracted waves tend to concentrate on the coast behind the peninsula where the area of damaged forest (the pink color in Figure 7.7) was also relatively higher near the coastal strip than in other coastal areas of the bay. Further on-site investigation is needed to identify the influence of this local concentration of wave heights behind the peninsula. The numerical computation results are intimately related to the vegetation change especially around the bay mouth (the red color in Figure 7.7). Small islands near the bay's mouth were highly damaged even though that part was covered with mangrove vegetation. Along the Hernani coast, the mixed forest was the dominant land cover category before the typhoon, and these areas were significantly changed after the typhoon.
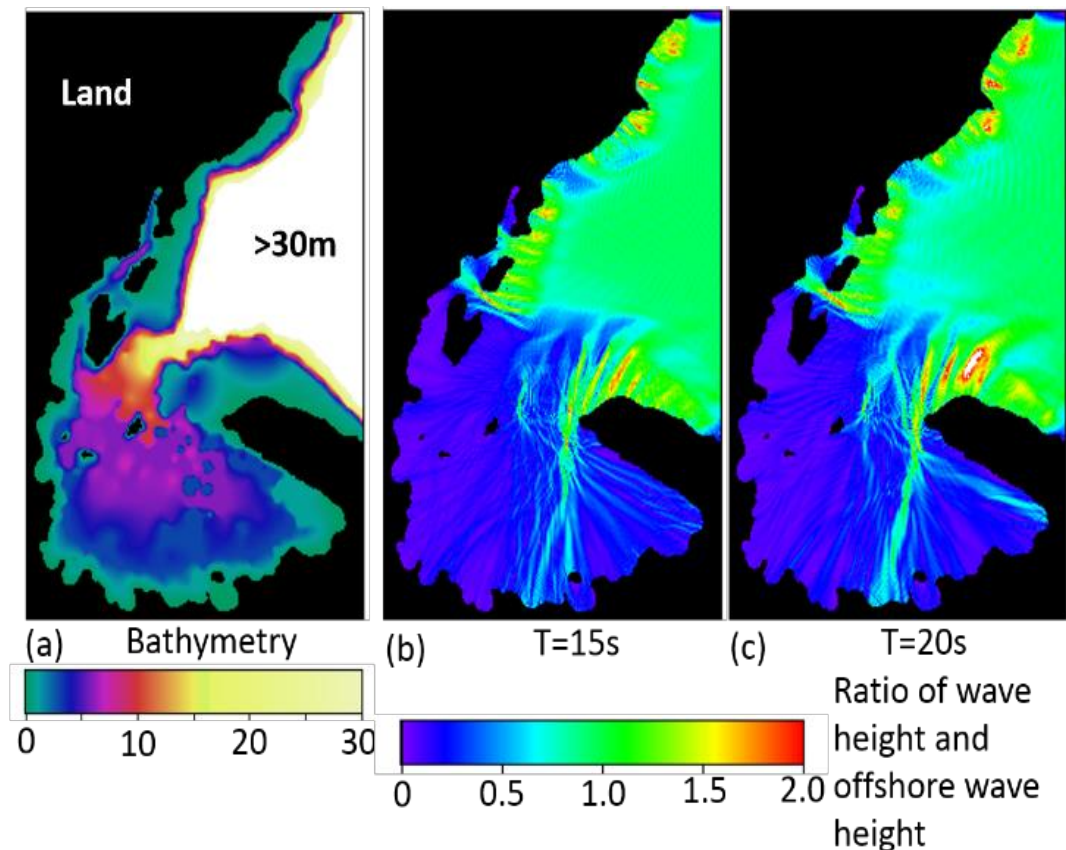
Figure 7.8 (a) Bathymetry data, (b and c) results of numerical computation of ratio of wave height and offshore wave height

It should also be pointed out that similar wave concentrations around Hernani and the coast behind the peninsula were also observed with different incident wave angles. As seen in Figure 7.8 (b) and (c), the wave angle was abruptly altered at the edge of the reef and the influence of the reef's bathymetry on the concentration of waves needs to be further investigated.

7.5 Conclusions and Future Study

The mapping of the typhoon's impact using remote sensing and numerical modeling provided clear evidence of the variation in the damage along the coast which could be further extended for detailed assessment.

The vegetation analysis was performed using the different seasonal LANDSAT-8 images (April and December) due to the presence of a higher percentage of cloud coverage. The seasonal effect on the change analysis could be minimized by using the same seasonal images. It was found that the overall vegetation coverage had been reduced after the typhoon.

Another interesting observation was that the comparisons of pre- and post-typhoon images clearly showed evidence of the movement of eroded sand both landward and seaward of the shoreline.

7.6 Summary

The east coast of Eastern Samar in the Philippines faces the Pacific Ocean and suffered significant damage due to storm waves caused by Typhoon Haiyan. The coast has various characteristic features such as a fringing coral reef, varying beach slopes, pocket beaches, and well-developed mangrove forest, especially inside Matarinao Bay. This paper aims to investigate how this characteristic coast was affected by the catastrophic typhoon mainly through observations of satellite images. Various types of optical satellite images were utilized to capture the changes before and after the typhoon. Comparisons of satellite observations and numerically computed wave height distributions along the coast clearly showed that the coast inside the bay was strongly protected by the sand spit with the fringing reef and, thus, the mangrove strip inside the bay was less damaged. It was also found that the

estimated penetration distance of the wave run-up on the beach showed a certain correlation with the local width of the fringing coral reef.

CHAPTER EIGHT

CONCLUSIONS AND RECOMMENDATIONS

8.1   Summary

The developed satellite-based monitoring system to monitor spatial and temporal variations of turbidity has been deployed successfully in Vietnam and been tested on the Enshu-nada coast, Japan. Even without the site-specific relationship of turbidity and surface reflectance we were able to discuss the relative variations of turbidity around the mouth of the Tenryu River. This study has demonstrated the use of the entire MODIS archive for the monitoring of coastal areas.

A higher area of turbidity plumes closely corresponds with a higher water level (high discharge) in a river. This relationship can be used to identify the high discharge events of a river where the measured water level or discharge data are not available.

The presence of highly turbid events on the alongshore direction can also be closely monitored over a period of time. The cell-based approach has the added advantage of gathering more data over a year, and it generates higher temporal results closer to the actual situation around nearshore areas.

The new cloud masking algorithm that was introduced has performed well to extract cloud free pixels in nearshore areas. This cloud masking algorithm is only applicable to nearshore areas, i.e. land areas are excluded.

8.2   Conclusions

The following conclusions can be drawn from this study:

1. A satellite-based monitoring scheme has been developed to investigate coastal areas.
2. The developed monitoring scheme can be easily applied to other areas for continuous monitoring of suspended sediment discharge.
3. The developed scheme has been demonstrated to understand fine sediment discharge patterns from rivers in two study sites.

4. Within the monitoring scheme, a new cloud masking algorithm is introduced and tested for other areas.

5. The output of the monitoring scheme can be used for coastal studies in wider aspects:

    a. As the feasibility for the use of MODIS data for other applications (the number of usable data is documented as a product);

    b. As validation of suspended sediment numerical models;

    c. As a Contribution to different levels of turbidity along the coast.

6. In the Vietnam study site:

    a. The relationship between the MODIS red band surface reflectance (MOD09) and turbidity has been developed;

    b. The relationship between turbidity and the suspended sediment concentration has also been developed;

    c. The Red River system shows a decreasing trend of suspended fine sediment discharge while the Ma River tends to have an increasing trend;

    d. The observed river discharge data were only gathered in the Ma River system and show a very clear correlation with the results of the monitoring system.

7. On the Enshu-nada coast:

    a. The cell-based daily turbidity product is able to capture the direction and alongshore extent of the suspended load of the Tenryu River, and shows a relationship with the shape of the sandpit near the river mouth;
        The flood events of the Tenryu River closely correspond with the derived area of the turbid plume.

8.3   Recommendations

The observed suspended sediment patterns need to be compared with waves and tidal currents to understand the mechanism of the observed results. This will enable us to understand the contribution of each factor for the spatial distribution of suspended sediment discharge.

The area extraction algorithm can be further improved by introducing a technique to extract only the turbid plume starting from a river mouth. This will improve the

results in two ways: 1). It will be possible to separate very closely oriented river mouth discharges; 2). It will be possible to remove the remaining boundary pixels of cloud patches in some of the cases.

REFERENCES

Ackerman, S. a., Strabala, K. I., Menzel, W. P., Frey, R. a., Moeller, C. C., & Gumley, L. E. (1998). Discriminating clear sky from clouds with MODIS. Journal of Geophysical Research, 103(D24), 32141. doi:10.1029/1998JD200032

Ackerman, S. A., Holz, R. E., Frey, R., Eloranta, E. W., Maddux, B. C., & McGill, M. (2008). Cloud detection with MODIS. Part II: Validation. Journal of Atmospheric and Oceanic Technology, 25(7), 1073–1086. doi:10.1175/2007JTECHA1053.1

Chen, Z., Hu, C., & Muller-Karger, F. (2007). Monitoring turbidity in Tampa Bay using MODIS/Aqua 250-m imagery. Remote Sensing of Environment, 109(2), 207–220. doi:10.1016/j.rse.2006.12.019

Daac, N. L. P., & Falls, S. (2014). MODIS Land Products Quality Assurance Tutorial :Part-1 How to find , understand , and use the quality assurance information for MODIS land products, 1–17.
Delucchi, L. (2013). pyModis Documentation.

Dogliotti, a. I., Ruddick, K. G., Nechad, B., Doxaran, D., & Knaeps, E. (2015). A single algorithm to retrieve turbidity from remotely-sensed data in all coastal and estuarine waters. Remote Sensing of Environment, 156, 157–168. doi:10.1016/j.rse.2014.09.020

Doxaran, D. et al., 2002. Spectral signature of highly turbid waters Application with SPOT data to quantify suspended particulate matter concentrations. , 81, pp.149–161.
Lewis, J. & Eads, R., 2001. Turbidity threshold sampling for suspended sediment load estimation. Proceedings of the Seventh Federal Interagency Sedimentation Conference, pp.110–117.

Doxaran, D., Froidefond, J.M., & Castaing, P. (2002). Areflectance band ratio used to esti- mate suspended matter concentrations in sediment-dominated coastal waters. International Journal of Remote Sensing, 23,5079–5085.

Doxaran, D., Froidefond, J.-M., & Castaing, P. (2003). Remote-sensing reflectance of turbid sediment-dominated waters. Reduction of sediment type variations and changing illumination conditions effects by use of reflectance ratios. Applied Optics, 42(15), 2623–34. Retrieved from http://www.ncbi.nlm.nih.gov/pubmed/12776997

Doxaran, D. et al., 2009. Dynamics of the turbidity maximum zone in a macrotidal estuary (the Gironde, France): Observations from field and MODIS satellite data.

Estuarine, Coastal and Shelf Science, 81(3), pp.321–332. Available at: http://linkinghub.elsevier.com/retrieve/pii/S0272771408004435

Farooq S. 2011. Spectral Reflectance of Land Covers, Department of Geology, Aligahr Muslim university., http://www.geol-amu.org/notes/m1r-1-8.htm

Gunasekara, K., Tajima, Y., Chi, L.H., Cuong, H.V., Hung, N.T and Hung, L.M (2016), Satellite based monitoring of turbidity around Hai Phong Ba, Vietnam. Journal of JSCE, B3(Ocean Engineering),

Hori, K., Tanabe, S., Saito, Y., Haruyama, S., Nguyen, V., and Kita- mura, A.: Delta initiation and Holocene sea-level change: exam- ple from the Song Hong (Red River) delta, Vietnam, Sediment. Geol., 164, 237–249, 2004.

Hubert Loisel, Vincent Vantrepotte, Cédric Jamet and Dinh Ngoc Dat (2013). Challenges and New Advances in Ocean Color Remote Sensing of Coastal Waters, Topics in Oceanography, Prof. Enrico Zambianchi (Ed.), InTech, DOI: 10.5772/56414

IOCCG (2000). Remote Sensing of Ocean Colour in Coastal, and Other Optically-Complex, Waters. Sathyendranath, S. (ed.), Reports of the International Ocean-Colour Coordinating Group, No. 3, IOCCG, Dartmouth, Canada.

Lewis, J., & Eads, R. (2001). Turbidity threshold sampling for suspended sediment load estimation. Proceedings of the Seventh Federal Interagency Sedimentation Conference, 110–117.

Lefebvre, J. P., Ouillon, S., Vu, D. V., Arfi, R., Panche, J. Y., Mari, X., Chu, V. T., and Torréton, J. P.: Seasonal variability of co- hesive sediment aggregation in the Bach Dang-Cam Estuary, Haiphong (Vietnam), Geo-Mar. Lett., 32, 103–121, 2012.

Liu, R., & Liu, Y. (2013). Generation of new cloud masks from MODIS land surface reflectance products. Remote Sensing of Environment, 133, 21–37. doi:10.1016/j.rse.2013.01.019

M. Wang and W. Shi, "Cloud masking for ocean color data processing in the coastal regions," IEEE Trans. Geosci. Remote Sens. 44, 3196-3205 (2006)

Milliman, J. D. and Meade, R. H.:World-wide delivery of river sed- iment to the oceans, J. Geol., 91, 1–21, 1983

Mitsuyasu, H.: On the growth of the spectrum of wind-generated waves (I), Rept. Res. Inst. for Applied Mech., Kyushu Univ., vol. XVI, No. 55, pp.459-482, 1968 MODIS Surface Reflectance User's Guide, 2011

.

National research project (code KC08.34/11-15). (2015). Science-based research and proposed solutions to improve the phenomenon of sedimatation in Do Son estuary, Hai Phong City, Vietnam. Center for river hydraulics engineering, Vietnam Academy for Water Resources.

Nordkvist, K., Loisel, H., & Gaurier, L. D. (2009). Cloud masking of SeaWiFS images over coastal waters using spectral variability. Optics Express, 17(15), 12246–12258. http://doi.org/10.1364/OE.17.012246

Ohnaka, S., A. Watanabe and M. Isobe: Numerical compu-tation of wave field by the unsteady mild slope equation ex-tended to wave-current coexisting field, Proc. of Coast. Eng., JSCE, 91-95 (in Japanese), 1989.

Park, E. & Latrubesse, E.M., 2014. Modeling suspended sediment distribution patterns of the Amazon River using MODIS data. Remote Sensing of Environment, 147, pp.232–242.

Park, E. & Latrubesse, E.M., 2015. Surface water types and sediment distribution patterns at the confluence of mega rivers: The Solim??es-Amazon and Negro Rivers junction. Water Resources Research, 51(8), pp.6197–6213.

Petus, C. et al., 2010. Estimating turbidity and total suspended matter in the Adour River plume (South Bay of Biscay) using MODIS 250-m imagery. Continental Shelf Research, 30(5), pp.379–392.

Petus, C. et al., 2014. Monitoring spatio-temporal variability of the Adour River turbid plume (Bay of Biscay, France) with MODIS 250-m imagery. Continental Shelf Research, 74, pp.35–49.

Ryota, H., Yoshimitsu T., Gunasekara, K. Nguyen, T. H. and Chi, L. H. (2015). Investigation of sediment transport characteristics along the coast of Ma river mouth adjacent to the Red river mouth. Journal of JSCE, B2 (Coastal Engineering), Vol. 71, No.2, I_715_720, 2015.

Tajima, J., Kawasaki, K., Asano, Y. and Ortigas, N. M.: Characteristics of Storm Surges and Stormy Waves Induced by Typhoon Haiyan around Leyte and Samar, Journal of JSCE, B2(Coast. Eng.), (printing), 2014.

Tajima, Y., Yasuda, T., Pacheco, B.M., Cruz, E. C., Kawa-saki, K., Nobuoka, H., Miyamoto, M., Asano, Y., Arikawa, T., Ortigas, N.M., Aquino, R., Mata, W., Valdez, J. and F. Briones: Initial report of JSCE-PICE Joint Survey on the storm surge disaster caused by Typhoon Haiyan, Coastal Eng. Journal, World Scientific, DOI: 10.1142/S0578563414500065, 2014.

Thieler, E.R., Himmelstoss, E.A., Zichichi, J.L., and Ergul, Ayhan.: Digital Shoreline Analysis System, version. 4.0- An ArcGIS extension for calculating shoreline change: U.S. Geological Survey Open-File Report 2008-1278, 2009.

U.S. Department of the Interior, U.S. Geological Sur-vey/Hazard Data Distribution System (URL: http://hddsexplorer.usgs.gov).

Vermote, E. F., El Saleous,N. Z., & Justice, C.O. (2002). Atmospheric correction ofMODIS data in the visible to middle infrared: First results. Remote Sensing of Environment, 83,97–111

Vermote, E. F., & Vermeulen, A. (1999). MODIS algorithm technical background document, atmospheric correction algorithm: Spectral reflectance (MOD09). NASA, contract NAS5-96062.

W. D. Robinson, B. A. Franz, F. S. Patt, S. W. Bailey, and P. J. Werdell, "Masks and flags updates," in NASA Technical Memorandum, S. B. Hooker and E. R. Firestone, eds., Vol. 22, pp. 34-40 (2003).

Wang, J., Lu, X., Zhou, Y., & Liew, S. (n.d.). Remote Sensing of Suspended Sediment Concentrations in Turbid Rivers: A Field Survey. Gsdi.Org. Retrieved from http://www.gsdi.org/gsdiconf/gsdi13/papers/200.pdf

Webster, P.J., Holland, G. J., Curry, J. A. and Chang, H.R.: Changes in tropical cyclone number, duration and intensity in a warm environment, Science, Vol. 309, pp1844-1846, 2005.

Wikipedia contributors: Typhoons in the Philippines, Wik-ipedia, The Free Encyclopedia, (accessed on May 10, 2014).

```
 1    echo
 2
 3    # Start Data of Back processing and period in days. This goes backward.
 4    #As example startday=2011-01-10 and period=10 means --> data from 2011-01-01 to
      2011-01-10 will be processed
 5    startday=`date -d "2016-08-24" +"%Y-%m-%d"`
 6    period=1825
 7
 8    cd /home/kubuntu/MY/MOD09GQ
 9
10    for c in  `seq 0 -1 -"$period"`
11    do
12
13        rm -f ./*.hdf
14        rm -f ./*.xml
15        rm -f ./*.txt
16        rm -f ./*.log
17        rm -f ./MOD09GQ*
18        rm -f ./MYD09GQ*
19
20        ############### MOD ###############
21
22        # Download Data - Change Tile Numbers and Product Name
23        ./modis_download.py -t h27v07 -p MOD09GQ.006 -f `date -d "$startday $c day"
          +'%Y-%m-%d'` -O ./
24
25        for file in ./listfile*.txt
26        do
27            ./modis_mosaic.py -s "0 1 1 0 0" -m "/home/kubuntu/MRT/" -o "MOD09GQ" "$file"
28        done
29
30        ./modis_convert.py -s "(1 1)" -g "250" -m "/home/kubuntu/MRT/" -t "UTM" -u "53" -o
          "MOD09GQ.tif" "MOD09GQ.hdf"
31
32        # Extract by Mask - Change study_area.shp file
33        for file in ./MOD09GQ*.tif
34        do
35            temp_d=`date -d "$startday $c day" +'%Y-%m-%d'`
36            temp_f=`basename ${file%.*}`
37            gdalwarp -of GTiff -dstnodata -32768 -cutline ./Study_area_MY.shp -
              crop_to_cutline -tr 250 250 "$file"
              "/home/kubuntu/Dropbox/01_ubuntu/Processed_data/MY/MOD09GQ/$temp_d.$temp_f.tif"
38        done
39
40        rm -f ./*.hdf
41        rm -f ./*.xml
42        rm -f ./*.txt
43        rm -f ./*.log
44        rm -f ./MOD09GQ*
45
46        ############### MYD ###############
47
48        # Download Data - Change Tile Numbers and Product Name
49        ./modis_download.py -t h27v07 -s MOLA -p MYD09GQ.006 -f `date -d "$startday $c day"
          +'%Y-%m-%d'` -O ./
50
51        for file in ./listfile*.txt
52        do
53            ./modis_mosaic.py -s "0 1 1 0 0" -m "/home/kubuntu/MRT/" -o "MYD09GQ" "$file"
54        done
55
56        ./modis_convert.py -s "(1 1)" -g "250" -m "/home/kubuntu/MRT/" -t "UTM" -u "53" -o
          "MYD09GQ.tif" "MYD09GQ.hdf"
57
58        # Extract by Mask - Change study_area.shp file
59        for file in ./MYD09GQ*.tif
60        do
61            temp_d=`date -d "$startday $c day" +'%Y-%m-%d'`
62            temp_f=`basename ${file%.*}`
```

```
63
64              gdalwarp -of GTiff -dstnodata -32768 -cutline ./Study_area_MY.shp -
                crop_to_cutline -tr 250 250 "$file"
                "/home/kubuntu/Dropbox/01_ubuntu/Processed_data/MY/MOD09GQ/$temp_d.$temp_f.tif"
65          done
66
67      rm -f ./*.hdf
68      rm -f ./*.xml
69      rm -f ./*.txt
70      rm -f ./*.log
71      rm -f ./MYD09GQ*
72
73  done
74
```

APPENDIX II

GPS number	Sample Number	Latitude	Longitude	Weight (mg): Suspended Sediment (SS) + filter paper						Weight of the filter paper (mg)	SS weight (mg)	Volume of water sample (ml)	SSC (mg/L)	Measured Turbidity (FTU)
				W1	W2	W3	W4	W5	Average weight					
2015 July 26														
234	N1	20.83167681	106.8116381	134	134	134	134	135	134.2	128	6.2	500	12.4	13.17
235	N2	20.83110684	106.8253963	131	133	132	133	133	132.4	126	6.4	500	12.8	15.35
236	N3	20.83853044	106.8294494	138	139	138	139	139	138.6	127	11.6	500	23.2	1.66
237	N4	20.82965509	106.8276708	136	132	134	135	134	134.2	128	6.2	500	12.4	118.56
238	N5	20.81828713	106.8421574	133	135	133	136	136	134.6	127	7.6	500	15.2	18.625
240	N6	20.82565701	106.8574769	142	143	142	143	143	142.6	126	16.6	500	33.2	87.37
241	N7	20.83372652	106.8730925	146	144	145	146	145	145.2	129	16.2	500	32.4	78.72
242	N8	20.82800654	106.88365	134	133	134	133	136	134	126	8	500	16	94.82
243	N9	20.81800374	106.893663	133	131	132	134	133	132.6	126	6.6	500	13.2	92.29
244	N10	20.80934289	106.9071703	165	166	163	166	167	165.4	127	38.4	500	76.8	280
245	N11	20.79353521	106.9144892	176	176	175	176	179	176.4	126	50.4	500	100.8	468
246	N12	20.78016892	106.9230767	141	143	142	141	143	142	126	16	500	32	514
2015 September 12														
250	K01	20.67841806	106.8089655	130	129	130	130		129.75	127	2.75	500	5.5	7.35
251	K02	20.66558856	106.80498	130	130	130	130		130	127	3	500	6	4.94
252	K03	20.67127559	106.7832723	134	134	134	134		134	127	7	500	14	11.8
253	K04	20.66686965	106.763048	131	134	131	133		132.25	128	4.25	500	8.5	8.6
254	K05	20.66796734	106.7400394	137	137	138	138		137.5	125	12.5	500	25	24.58
255	K06	20.66949469	106.7259349	159	160	160	162		160.25	125	35.25	500	70.5	60.84
256	K07	20.67756336	106.7085883	137	139	139	139		138.5	128	10.5	500	21	24.99
257	K08	20.65355382	106.7234413	139	138	140	139		139	129	10	500	20	25.5
2015 November 17 and 18														
137	C1	20.73098182	106.8018488	140	139	139			139	128	11.3	500	22.7	27.01
139	C2	20.74096106	106.8016384	147	147	147			147	126	21.0	500	42.0	42.17

140	C3	20.74933609	106.7965202	146	147	146			146	126	20.3	500	40.7	31.26
141	C4	20.74918228	106.8046508	141	141	142			141	129	12.3	500	24.7	30.07
142	C5	20.73648722	106.8088412	140	141	141			141	129	11.7	500	23.3	21.21
290	C11	20.66810489	106.7954858	135	134	135			135	127	7.7	500	15.3	14.47
291	C12	20.66917894	106.7831442	131	131	132			131	127	4.3	500	8.7	12.15
292	C13	20.67060253	106.7694081	135	136	136			136	129	6.7	500	13.3	14.6
294	C14	20.67082222	106.7533701	132	134	134			133	127	6.3	500	12.7	15.36
296	C15	20.67662216	106.7434078	135	134	134			134	127	7.3	500	14.7	15.87

APPENDIX III

No.	Date of Image	Image coordinate: X	Image coordinate: Y	Longitude	Latitude	POI Name	Class	Band 1 (Red)	Band 2 (NIR)
1	2000.03.09	464.5	272.5	137.7700158	34.58504166	Pin 1	DC	0.9507	0.9697
2	2000.03.09	439.5	256.5	137.7031116	34.62260072	Pin 4	DC	0.8557	0.8717
3	2000.03.09	478.5	249.5	137.8098798	34.635961	Pin 5	DC	0.2986	0.3114
4	2000.09.15	237.5	304.5	137.1498876	34.52542319	Pin 7	DC	0.5113	0.5236
5	2002.09.12	354.5	236.5	137.4728669	34.67256379	Pin 1	DC	0.8714	0.8756
6	2002.09.12	507.5	254.5	137.8884922	34.62285569	Pin 2	DC	0.6237	0.6389
7	2002.09.18	504.5	251.5	137.8805545	34.62980399	Pin 1	DC	0.345	0.3606
8	2002.10.11	349.5	286.5	137.4559139	34.56021858	Pin 1	DC	0.7683	0.7797
9	2002.10.11	438.5	254.5	137.7005335	34.62716508	Pin 2	DC	0.4008	0.4218
10	2002.10.11	495.5	246.5	137.8564245	34.64163942	Pin 7	DC	0.2442	0.2581
11	2002.10.11	426.5	256.5	137.6676967	34.62338092	Pin 9	DC	0.5154	0.5458
12	2005.09.08	250.5	315.5	137.1846274	34.50001304	Pin 2	DC	0.4733	0.4679
13	2005.09.14	435.5	251.5	137.6925789	34.63410189	Pin 1	DC	0.5648	0.5813
14	2005.09.14	382.5	264.5	137.5472702	34.60792726	Pin 2	DC	0.2399	0.2476
15	2005.09.08	530.5	271.5	137.9497812	34.58307931	Pin 4	DC	0.301	0.3297
16	2010.09.29	379.5	274.5	137.5384123	34.58557481	Pin 4	DC	0.3625	0.3797
17	2010.09.29	285.5	303.5	137.2806031	34.52530522	Pin 5	DC	0.2128	0.2236
18	2013.09.21	549.5	249.5	138.0032877	34.63134802	Pin 10	DC	0.1337	0.1454
19	2013.09.21	540.5	254.5	137.9783711	34.62069248	Pin 11	DC	0.1414	0.1557
20	2013.09.23	470.5	252.5	137.7878585	34.62970612	Pin 1	DC	0.3041	0.3033
21	2013.09.23	515.5	272.5	137.9088672	34.58180868	Pin 2	DC	0.5427	0.5527
22	2013.09.23	464.5	266.5	137.7704646	34.59855288	Pin 5	DC	0.4011	0.4182
23	2010.09.29	523.5	241.5	137.9331021	34.65108506	Pin 5	DC	0.5079	0.5465
24	2010.09.29	382.5	246.5	137.5485103	34.64846799	Pin 9	DC	0.3711	0.3859
25	2000.09.15	476.5	247.5	137.8045828	34.64059008	Pin 1	HT	0.1683	0.0818

26	2000.09.15	468.5	249.5	137.7826358	34.63658612	Pin 2	HT	0.1482	0.0484
27	2002.10.02	517.5	242.5	137.9166757	34.64922596	Pin 1	HT	0.1003	0.0344
28	2002.10.02	659.5	188.5	138.3083075	34.76089029	Pin 2	HT	0.1072	0.0412
29	2002.10.02	471.5	248.5	137.7908846	34.63865103	Pin 3	HT	0.0886	0.0332
30	2005.09.08	75.5	88.5	136.7188931	35.01913447	Pin 3	HT	0.1512	0.0713
31	2005.09.08	83.5	297.5	136.7309365	34.5478608	Pin 6	HT	0.1504	0.0636
32	2005.09.08	474.5	247.5	137.7991337	34.64071537	Pin 1	HT	0.1284	0.0583
33	2010.09.29	472.5	249.5	137.7935335	34.6363368	Pin 1	HT	0.1371	0.0624
34	2010.09.29	477.5	257.5	137.8065483	34.6180095	Pin 2	HT	0.1077	0.0297
35	2013.09.21	475.5	247.5	137.8018583	34.64065276	Pin 1	HT	0.1609	0.0967
36	2013.09.21	479.5	248.5	137.8126802	34.63814993	Pin 2	HT	0.1567	0.0897
37	2013.09.21	480.5	252.5	137.8151001	34.62907995	Pin 5	HT	0.1328	0.0514
38	2010.09.29	471.5	247.5	137.7909601	34.64090285	Pin 1	HT	0.1502	0.0649
39	2010.09.29	465.5	249.5	137.7744624	34.63677247	Pin 2	HT	0.1408	0.0527
40	2000.09.15	236.5	297.5	137.1475705	34.54124172	Pin 9	LC	0.0609	0.0467
41	2002.09.12	476.5	254.5	137.8040519	34.62482756	Pin 5	LC	0.0593	0.0469
42	2002.09.12	430.5	275.5	137.6772193	34.58035322	Pin 6	LC	0.058	0.0599
43	2002.09.18	398.5	256.5	137.5914139	34.62502647	Pin 5	LC	0.0374	0.0418
44	2002.10.11	453.5	266.5	137.7405086	34.59922985	Pin 4	LC	0.0797	0.0734
45	2005.09.14	366.5	255.5	137.5042939	34.62910111	Pin 6	LC	0.0867	0.0904
46	2005.09.14	361.5	255.5	137.4906697	34.62938024	Pin 7	LC	0.0364	0.0388
47	2005.09.08	522.5	273.5	137.9278445	34.57910106	Pin 7	LC	0.0674	0.0557
48	2005.09.08	245.5	275.5	137.1733636	34.59037184	Pin 9	LC	0.063	0.0404
49	2010.09.29	410.5	270.5	137.6231148	34.59279718	Pin 6	LC	0.0239	0.017
50	2013.09.21	565.5	254.5	138.0464547	34.61900969	Pin 12	LC	0.0638	0.0745
51	2013.09.21	560.5	244.5	138.0336586	34.64186257	Pin 13	LC	0.0779	0.084
52	2013.09.23	456.5	257.5	137.749347	34.61931308	Pin 11	LQ	-0.01	-0.01

53	2002.10.02	480.5	266.5	137.8140353	34.59755509	Pin 4	LT	0.0318	0.002
54	2002.10.02	526.5	254.5	137.9402418	34.62161828	Pin 9	LT	0.0472	0.0105
55	2005.09.08	387.5	204.5	137.5650558	34.74277509	Pin 5	LT	0.0362	0.0344
56	2010.09.29	468.5	261.5	137.7817332	34.6095641	Pin 12	LT	0.0316	0.0005
57	2013.09.21	477.5	266.5	137.8058659	34.59774335	Pin 7	LT	0.018	0.0011
58	2013.09.23	443.5	240.5	137.7151832	34.6583899	Pin 9	LT	0.0862	0.0304
59	2013.09.23	441.5	252.5	137.7088529	34.63148767	Pin 13	LT	0.012	0.0005
60	2013.09.23	430.5	243.5	137.6795359	34.65241826	Pin 14	LT	0.0044	0.0006
61	2000.03.09	477.5	267.5	137.8057902	34.59549156	Pin 3	MC	0.3427	0.3475
62	2000.03.09	425.5	238.5	137.6662706	34.66397733	Pin 6	MC	0.1578	0.1477
63	2000.03.09	483.5	262.5	137.8225095	34.60637333	Pin 7	MC	0.162	0.1472
64	2000.09.15	236.5	307.5	137.1469919	34.51871225	Pin 8	MC	0.1186	0.1125
65	2000.09.15	152.5	325.5	136.9174007	34.48195991	Pin 10	MC	0.1266	0.101
66	2002.09.12	461.5	263.5	137.7625188	34.60549388	Pin 3	MC	0.1227	0.1207
67	2002.09.12	498.5	272.5	137.8625859	34.58290386	Pin 7	MC	0.1221	0.1136
68	2002.09.18	491.5	257.5	137.8446804	34.61712557	Pin 2	MC	0.079	0.0809
69	2002.10.11	491.5	244.5	137.8456807	34.6463978	Pin 3	MC	0.144	0.1529
70	2005.09.08	478.5	250.5	137.8098038	34.63370923	Pin 1	MC	0.1485	0.1071
71	2005.09.08	473.5	276.5	137.7942189	34.57547529	Pin 4	MC	0.1482	0.1569
72	2005.09.14	373.5	250.5	137.5237087	34.63996928	Pin 4	MC	0.1161	0.115
73	2005.09.08	517.5	272.5	137.9143119	34.58167868	Pin 5	MC	0.0898	0.0865
74	2005.09.08	508.5	276.5	137.8894985	34.57325519	Pin 6	MC	0.075	0.0595
75	2005.09.08	243.5	284.5	137.1673886	34.57019271	Pin 8	MC	0.075	0.059
76	2010.09.29	375.5	242.5	137.5297065	34.6578746	Pin 7	MC	0.0598	0.0588
77	2013.09.23	462.5	246.5	137.7665135	34.64371385	Pin 3	MC	0.1816	0.1692
78	2013.09.23	465.5	263.5	137.7734126	34.60524655	Pin 4	MC	0.1252	0.1235
79	2013.09.23	369.5	236.5	137.5137605	34.67172688	Pin 6	MC	0.1976	0.2214

80	2013.09.23	370.5	240.5	137.5162141	34.66266139	Pin 7	MC	0.2138	0.2311
81	2010.09.29	525.5	287.5	137.9349026	34.54738295	Pin 6	MC	0.0796	0.0616
82	2010.09.29	388.5	255.5	137.5642379	34.62785486	Pin 8	MC	0.0695	0.0555
83	2000.09.15	417.5	248.5	137.6437499	34.64193177	Pin 3	MT	0.0652	0.0216
84	2000.09.15	447.5	249.5	137.7254206	34.63787908	Pin 4	MT	0.093	0.0256
85	2002.10.02	463.5	252.5	137.7687888	34.63014083	Pin 5	MT	0.0543	0.0063
86	2002.10.02	518.5	249.5	137.9188474	34.63339979	Pin 8	MT	0.073	0.026
87	2005.09.08	482.5	252.5	137.8205484	34.62895398	Pin 2	MT	0.1059	0.0258
88	2005.09.08	491.5	246.5	137.8455267	34.64189439	Pin 3	MT	0.0766	0.0396
89	2010.09.29	489.5	265.5	137.8386195	34.59923874	Pin 3	MT	0.0578	0.0144
90	2010.09.29	465.5	255.5	137.7740123	34.62326138	Pin 11	MT	0.0669	0.0214
91	2013.09.21	485.5	254.5	137.8285677	34.6242611	Pin 3	MT	0.0758	0.0213
92	2013.09.21	474.5	254.5	137.7986039	34.62495278	Pin 4	MT	0.1285	0.0422
93	2013.09.21	485.5	259.5	137.8281854	34.61300236	Pin 6	MT	0.0686	0.0166
94	2013.09.23	457.5	244.5	137.7530388	34.64852614	Pin 8	MT	0.1111	0.0372
95	2013.09.23	471.5	246.5	137.7910356	34.64315466	Pin 10	MT	0.1181	0.0423
96	2013.09.23	477.5	246.5	137.8073833	34.64277913	Pin 12	MT	0.1796	0.1431
97	2013.09.23	474.5	249.5	137.7989823	34.63621178	Pin 15	MT	0.1232	0.0491
98	2010.09.29	480.5	260.5	137.8144914	34.61106576	Pin 3	MT	0.0948	0.0263
99	2000.03.09	494.5	246.5	137.8537001	34.64170325	Pin 2	NT	0.0171	0.008
100	2000.03.09	445.5	248.5	137.7200449	34.64025277	Pin 8	NT	0.0388	0.0325
101	2000.09.15	499.5	249.5	137.8670895	34.63462848	Pin 5	NT	0.0105	-0.0017
102	2000.09.15	382.5	251.5	137.5481656	34.63720671	Pin 6	NT	0.0111	-0.0016
103	2002.09.12	452.5	249.5	137.7390436	34.63757366	Pin 4	NT	0.0017	0.0007
104	2002.09.18	468.5	257.5	137.7820339	34.61857146	Pin 4	NT	0.0031	-0.0003
105	2002.10.02	455.5	277.5	137.7451399	34.57433622	Pin 6	NT	0.0019	0.0001
106	2002.10.02	421.5	272.5	137.6529282	34.58764495	Pin 10	NT	0.0033	0.0002

107	2002.10.11	461.5	249.5	137.7635645	34.63702008	Pin 5	NT	0.004	0.002
108	2002.10.11	502.5	260.5	137.8744072	34.60966774	Pin 6	NT	-0.0022	-0.0024
109	2002.10.11	559.5	243.5	138.0310166	34.6441817	Pin 8	NT	-0.0024	0.0005
110	2005.09.14	315.5	253.5	137.3654467	34.63638209	Pin 3	NT	-0.0018	-0.0009
111	2005.09.14	480.5	274.5	137.8134275	34.57954079	Pin 5	NT	0.005	-0.0009
112	2005.09.14	341.5	245.5	137.4368304	34.65300607	Pin 8	NT	0.0015	0.001
113	2005.09.08	421.5	250.5	137.6545059	34.63719069	Pin 10	NT	0.0058	-0.001
114	2005.09.08	388.5	238.5	137.5654178	34.6661427	Pin 11	NT	0.0236	-0.0011
115	2010.09.29	429.5	252.5	137.676159	34.63220992	Pin 9	NT	0.0038	-0.0012
116	2010.09.29	527.5	252.5	137.9431245	34.62605558	Pin 10	NT	0.0024	-0.0005
117	2013.09.21	496.5	247.5	137.8590716	34.63932385	Pin 8	NT	-0.01	-0.0015
118	2013.09.21	437.5	244.5	137.698539	34.64974528	Pin 9	NT	-0.01	-0.0021
119	2013.09.21	517.5	245.5	137.9164389	34.64247127	Pin 14	NT	-0.01	-0.0031
120	2010.09.29	498.5	250.5	137.8642879	34.63244087	Pin 4	NT	0.005	-0.0007
121	2010.09.29	444.5	241.5	137.717835	34.65607719	Pin 7	NT	0.0183	0.0119